UNIVERSITÀ DEGLI STUDI DI PADOVA

Dipartimento di Fisica e Astronomia "Galileo Galilei"

Master Degree in Physics

Final Dissertation

Calorimetry for MUonE

Thesis supervisor

Prof. Franco Simonetto

Thesis co-supervisor

Dr. Enrico Conti

Candidate

Sara Cesare

Academic Year 2021/2022

Introduction

The muon anomalous magnetic moment $a_\mu = (g_\mu - 2)/2$ is one of the most precisely measured quantity, as one of the most precisely calculable in the Standard Model. For the last twenty years, the experimental measurements have been pointing to a significant difference from the theoretical prediction. The latest measurements from FNAL g-2 experiment, that confirmed the previous ones from BNL, shows a discrepancy with the SM prediction of $4.2\,\sigma$. In order to solve this situation and understand if it could lead to new physics, both the theoretical and experimental uncertainties on the values have to be reduced. On the experimental side, FNAL g-2 and a new experiment at J-Park are trying to achieve higher precision, whereas the main contribute to the theoretical error is due to the calculation of the hadronic contribute of a_μ. With its experimental proposal, the MUonE experiments is trying to calculate a_μ^{had} with an innovative and independent method, based on the calculation of a dispersive integral with a space-like approach. To perform this calculation, the MUonE experiment will exploit experimental data on the shape of the cross section of the elastic process $\mu e \to \mu e$. High energy muons from the CERN M2 beam line will interact with the electrons of Beryllum targets inserted in a modular tracking system. A final electromagnetic calorimetr of PbWO4 scintillating crystals is placed downstream the detector. As for today, the main analysis for the extrapolation of the hadronic contribution is performed thanks to information from the tracking system, but an alternative could be represented by the calorimeter.

In this thesis the role of the calorimeter is investigated and its performances are evaluated through software simulations and with the analysis of data from the first test beam at CERN. After a detailed introduction of the theoretical framework in the first chapter, and the description of MUonE proposal and experimental apparatus in chapter 2, the Fast Simulation software tool is introduced in the third chapter, including the new features implemented in the latest Fast Simulation version used for this analysis. The main goal of the simulation exercise is to study the performances of the calorimeter in

terms of energy resolution and energy reconstruction, Particle identification and event selection. At the end of chapter 4, a a preliminary evaluation of the contribution of the calorimeter to the determination of the Mandelstam variable t is performed.

The final chapter is dedicated to the description and analysis of the calorimeter Test Beam of July 2022, I was lucky enough to participate. A first prototype of the calorimeter was tested in a one-week of data taking Test Beam at the T9 beam line of SPS at CERN. The description of the apparatus and DAQ is presented and also the results from a preliminary analysis on the electronic noise are reported.

Contents

Chapter 1

Introduction to the Muon Anomalous Magnetic Moment

1.1 The magnetic moment and its anomaly

The subject of this thesis is in the study of the muon magnetic moment and it's anomaly. To deeply understand the importance of this observable and its role on testing the Standard Model of particle physics, it is necessary to retrace the mains steps that led to its definition. In classical mechanic, an electric charge e with a mass m carries a magnetic dipole moment defined as

$$\vec{\mu}_L = (\frac{e}{2m})\vec{L} \tag{1.1}$$

where $\vec{L} = m\vec{r} \times \vec{v}$ is the orbital angular momentum. When the particle is in presence of a magnetic field $\vec{B}$, the magnetic moment tends to align to the field, therefore the particle experience a mechanical torque

$$\vec{M} = \vec{\mu} \times \vec{B} \tag{1.2}$$

With the discovery of the spin, another magnetic moment was defined: the instrinsic magnetic moment. In this definition, the orbital angular momentum $\vec{L}$ is replaced by the spin $\vec{S}$ and the intrinsic magnetic moment is usually defined in terms of Bohr magneton μ_B

$$\vec{\mu}_s = -g(\frac{e}{2m})\vec{S} = -g\frac{\mu_B}{\hbar}\vec{S} \tag{1.3}$$

$$\mu_B = \frac{e\hbar}{2m} \tag{1.4}$$

Also in this case, a particle's spin tends to twist to align with a magnetic field. This effect becomes dramatically macroscopic when electron spins twist together in a ferromagnet. The Dirac equation predicts fermion magnetic moments to be precisely two in units of Bohr magnetons [1]. That means that the *dimensionless giromagnetic ratio g* needs to assume the value 2. This theoretical prediction was supported by many experimental measurement until, after twenty years, it was showed that the electron's magnetic moment exceeded the value of 2 by a small quantity. The experiment was performed by Kusch and Foley and the values for the electron anomalous magnetic moment was found to be [2]:

$$g_e^{th} = 2 \cdot 1.001161 \tag{1.5}$$

$$g_e^{exp} = 2 \cdot (1.001119 \pm 0.00005) \tag{1.6}$$

This discrepancy together with the existence of another anomaly, the Lambda Shift, motivated a huge theoretical effort that gave birth to the QED thanks to which Schwinger predicted the so called anomaly. In fact in QED the anomaly is explained with lowest-order radiative correction to the Dirac moment and it quantifies the discrepancy between the actual value of g and the value of 2. The electron anomalous magnetic moment has been theoretically calculated to tenth order in quantum electrodynamics (QED) and experimentally confirmed to about two parts in 10^{10}. The muon anomalous magnetic moment is also very precisely measured and the expected value is

$$a_\mu^{SM} = 116591810(43) \times 10^{-11} [3] \tag{1.7}$$

thath differs from the electronic one due to the different masses. However, the experimental value, that will be described in detail in the next sections, is in tension with the one predicted by the Standard Model. This discrepancy has provided a enduring hint for new physics. The only way to solve this inconsistency is to try and the reduce the experimental error and at the same time increase the theoretical accuracy.

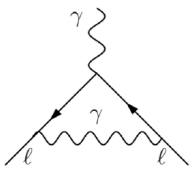

Figure 1.1: Schwinger's lowest order QED contribution to the anomalous magnetic moment

1.2 Theoretical description of the muon anomaly

The muon is considered a heavier and unstable version of the electron. In the Standard Model it is classified as a lepton, a particle with half integer spin. There are three generations of leptons divided into doublets.

$$L_e = \begin{pmatrix} \nu_e \\ e^- \end{pmatrix}_L \quad L_\mu = \begin{pmatrix} \nu_\mu \\ \mu^- \end{pmatrix}_L \quad L_\tau = \begin{pmatrix} \nu_\tau \\ \tau^- \end{pmatrix}_L , \tag{1.8}$$

The muon has a mass of $0.105\,GeV/c^2$ and a lifetime of $2.2\,\mu s$. Its anomaly is a more sensitive probe for new physics than its lighter version, the electron, but it is also more affected by weak and strong interactions. In fact, as pointed out by Berestetskii et al in 1956 [4], the anomalous magnetic moment is modified by quantum fluctuations of heavier particles, as described by the formula

$$\frac{\delta a_l}{a_l} \propto \left(\frac{m_l}{M}\right)^2 \tag{1.9}$$

Accordingly to this relation, while the electron represents a stringent test for QED, in the case of the muon, the sensitivity of deviation from pure QED is enhanced of a factor $m_\mu^2/m_e^2 \sim 43000$. For the same reason the τ lepton should represent an even better candidate for the research of new physics. Unfortunately, its short lifetime of about 290 fs makes it very difficult to measure a_τ with the required precision with the current technologies. Instead, the muon longer lifetime allows accurate measurements of its different characteristics, including the magnetic moment.

1.2.1 Muon g-2 in the Standard Model

In the Standard Model, the muon anomaly can be expressed as a sum of the pure QED term and the contributes of electroweak and strong interactions, as described by the formula:

$$a_\mu^{SM} = a_\mu^{QED} + a_\mu^{EW} + a_\mu^{had} \tag{1.10}$$

While the electromagnetic and weak contributions can be calculated precisely with perturbative expansion, the evaluation of the hadronic contribution must rely on experimental data or on lattice QCD calculations, as explained in the next sections. The most

recent calculation for the Standard Model value is:

$$a_\mu^{SM} = 116591810(43) \times 10^{-11} \quad [3] \tag{1.11}$$

where the greatest source of uncertainty comes from the the hadronic contribution. The most important hadronic contributions are the Leading Order Hadronic Vacuum Polarization term, that relies on experimental data, and the Light-by-Light contribute.

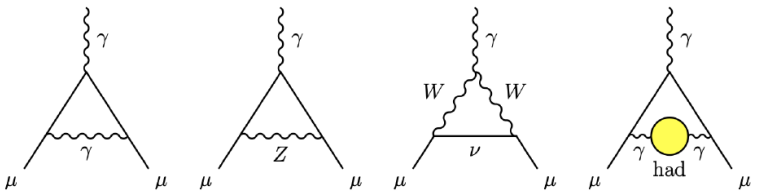

Figure 1.2: Feynmann diagrams of the main contributes to a_{mu}

QED contribution

For the electron a_e, that is the most precisely measured quantity in the SM, the pure QED contribution is the dominant one. Dealing with the muon, the higher mass must be taken into account. In fact, there are mass dependent terms that are therefore enhanced. In particular we can write the QED contribution to a_{mu} as the sum of three terms:

$$a_\mu^{QED} = A_1 + A_2(m_\mu/m_e) + A_2(m_\mu/m_\tau) + A_3(m_\mu/m_e, m_\mu/m_\tau) \tag{1.12}$$

Here the mass dependence is in evidence. While the first term is common for the three leptons, the other two are suppressed in the case of the electron and they account for internal loop diagrams as shown in fig.1.3 [5].

It is also possible to write a_μ^{QED} expanding the coefficients A_j in perturbation series of the fine structure α, thus obtaining with the latest calculations at five loops [3]:

$$a_\mu^{QED}(\alpha(Cs)) = 116584718.931(7)(17)(6)(100)(23) \times 10^{-11} \tag{1.13}$$

$$a_\mu^{QED}(\alpha(a_e)) = 116584718.842(7)(17)(6)(100)(28) \times 10^{-11} \tag{1.14}$$

In the two calculations, the fine structure constant has been extracted from the measurement of the Cesium atom or by the electron anomalous magnetic moment a_e. In

both cases, the main uncertainties arise from the τ-lepton mass, the eight/tenth/twelfth order QED estimates and the fine structure constant α.

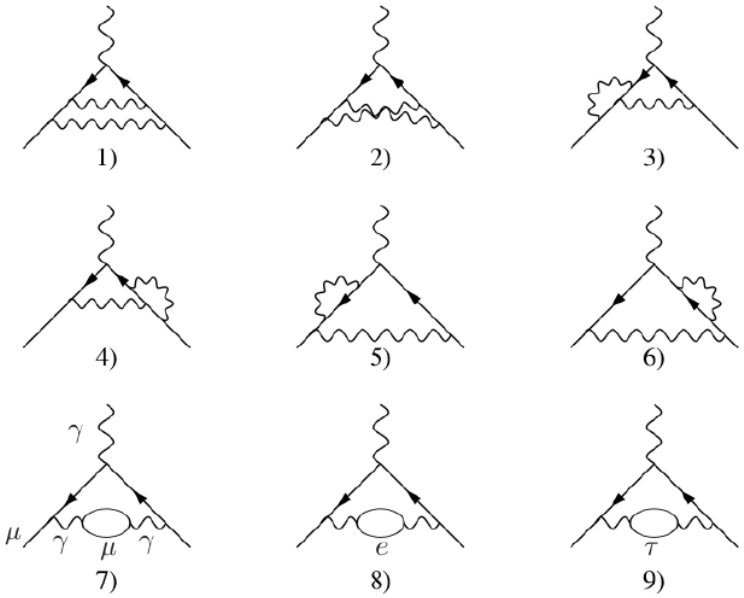

Figure 1.3: Second order QED diagrams that contributes to the muon anomaly.

Electroweak contribution

The electroweak contribution collects all the loop involving $W^{\pm}$, Z or Higgs bosons (the leading order diagrams are shown in the fig1.4).Therefore it is suppressed by a factor $\sim \left(\frac{m_\mu}{m_W}\right)^2$ and it is the least significant of all the contributions. The current calculations, including two loops and leading order three loops, gives the value [6]

$$a_\mu^{EW} = 153.6(1.0) \times 10^{-11} \tag{1.15}$$

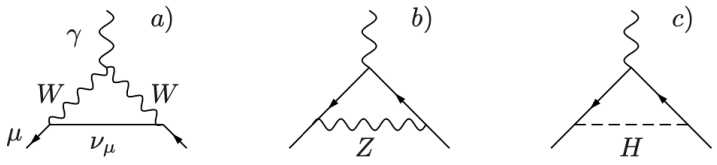

Figure 1.4: The leading weak contributions to a_μ.

The hadronic contribution

The hadronic contributions are divided into the hadronic vacuum polarization (HVP), at leading order (LO) and next to leading order (NLO), and the light-by-light contributios, which are summmed to give

$$a_\mu^{had} = a_\mu^{LO,HVP} + a_\mu^{NLO,HVP} + a_\mu^{HLbL}. \tag{1.16}$$

Hadronic contributions cannot be determined by perturbation theory due to the non-perturbative nature of QCD at low energies. Therefore other methods must be used. As of today, all the three terms are determined by means of dispersion relation from cross section of experimental data, and will be described more in details in the next section.

1.2.2 Hadronic Vacuum Polarization

This is the dominant hadronic contribution. The hadronic vacuum polarization is inserted in the internal photon line of the leading one loop muon vertex diagram in fig.1.5.

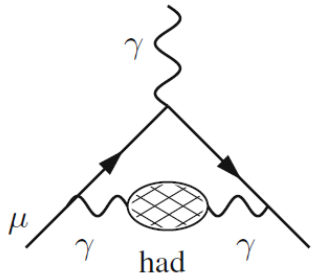

Figure 1.5: Leading order hadronic vacuum polarization diagram

Today, the main evaluation of a_μ^{HVP} comes from a time-like data based approach, that uses dispersion relation exploiting measurements of cross section of $e^+e^- \to had$. Lately, also lattice QCD (LQCD) has demonstrated important progress in the evaluation of this contribution, but its precision is not competitive yet. In the next paragraphs, these two methods will be analyzed and the latest results reported.

Time-like approach

The diagram representing the leading order hadronic vacuum polarization correspond to a dispersion integral [5]

$$a_\mu = \frac{\alpha}{\pi}\int_0^\infty \frac{ds}{\pi} Im\Pi_\gamma'^{had}(s)\frac{K(s)}{s} \tag{1.17}$$

$$K(s) = \int_0^1 dx \frac{x^2(1-x)}{x^2+(1-x)s/m_\mu^2} \tag{1.18}$$

where $K(s)$ is the well know kernel function as a function of the time-like squared momentum transfer $s = q^2 > 0$. The imaginary part of the self-energy function $Im\Pi_\gamma'^{had}$ is determined via the optical theorem (displayed in fig.1.6) by the total cross section of hadron production in electron-positron annihilation:

$$Im\,\Pi_\gamma'^{had}(s) = \frac{\sigma(e^+e^- \to \gamma^* \to hadrons)}{4\pi\alpha/s} = \frac{\alpha}{3}R(s) \tag{1.19}$$

R(s) is the hadronic R-ratio, that is the ratio between the hadronic cross section and the cross section $\sigma(e^+e^- \to \mu^+\mu^-)$. Substituting R(s) in eq.1.18, the dispersion relation at leading order becomes

$$a_\mu^{HVP} = \frac{\alpha^2}{3\pi^2}\int_{m_\tau^2}^\infty \frac{ds}{s}R(s)K(s) \tag{1.20}$$

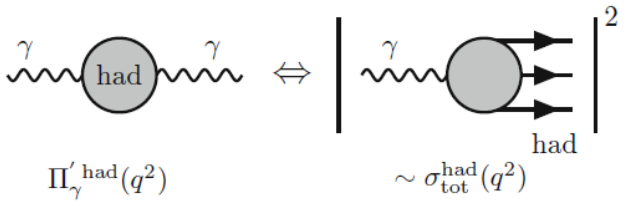

Figure 1.6: Schematic representation of the optical theorem

This methodology is based on the general principles of causality and unitarity, which imply respectively analyticity of quantum field theory and, as already mentioned, the validity of the optical theorem. But since at high energies, thanks to the asymptotic freedom, QCD becomes perturbative, the common strategy is to divide the energy scale and to use experimental data up to a certain energy E_{cut} and then perform perturbative calculations. Therefore the final dispersion relation can be written as:

$$a_\mu^{Had} = (\frac{\alpha m_\mu}{3\pi})\left(\int_{4m_\tau^2}^{E_{cut}^2}\frac{ds}{s^2}R^{data}(s)K(s) + \int_{E_{cut}^2}^\infty \frac{ds}{s^2}R^{pQCD}(s)K(s)\right) \tag{1.21}$$

In the recent review [3] several measurements of a_μ^{HVP} from data collected by different experiments are listed. For example, fig.1.7 compares results from different experiment measuring the cross section in the $\pi^+\pi-$ channel, while fig.1.8 compares the final evaluation from the inclusive cross section $e^+e^- \to hadrons$. The discrepancies between the different results are strongly affecting the precision of the combined cross section used in the dispersive integral. Moreover, in the low energy region $R(s)$ is highly fluctuating due to the presence of hadronic resonances. The presence of ρ and ω resonance is the raeson for the largest contribution to the error on a_μ^{HLO}.

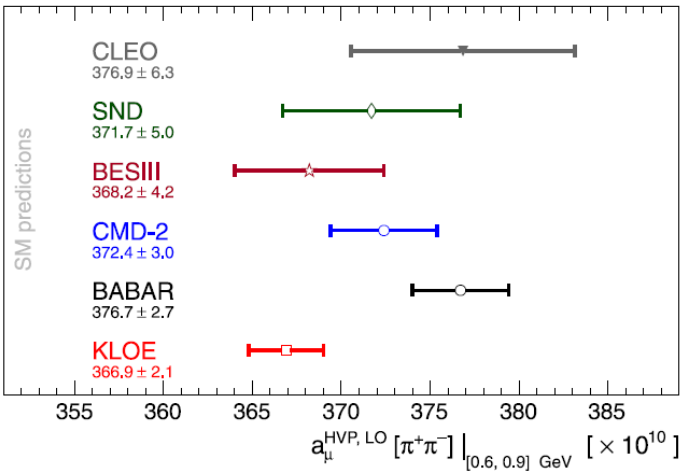

Figure 1.7: Comparison of evaluations of a^{HLO} determined from pion cross section data.

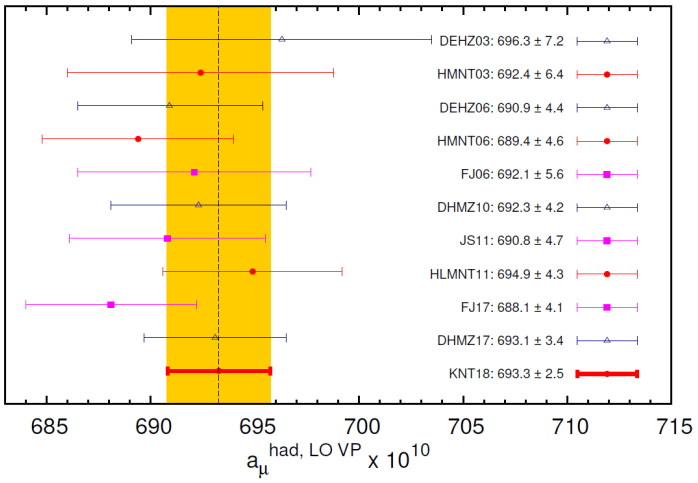

Figure 1.8: Comparison of evaluations of a^HO determined from hadrons cross section data.

The final value for the hadronic LO and NLO vacuum polarization contribution from the combination of all these experiments [3] are:

$$a_\mu^{HVPLO} = 6931(40) \times 10^{-11} \tag{1.22}$$

$$a_\mu^{HVP,NLO} = -98.3(7) \times 10^{-11} \tag{1.23}$$

Lattice QCD calculation

An alternative determination of a_μ^{HVP} can be provided by lattice QCD. Significant progresses have been made in the last few years in lattice QCD calculations of the LO part of the muon anomalous magnetic moment, $a_\mu^{HVP}(LO)$. Recently, the BMW collaboration presented the first lattice QCD calculation of $a_\mu^{HVP}(LO)$ with an impressive sub-percent (0.8%) relative accuracy [7]. This remarkable result weakens the longstanding discrepancy between the muon g-2 SM prediction and the experimentally measured value. However, this result shows a tension with the timelike data-driven determinations of $a_\mu^{HVP}(LO)$. The lattice QCD value is 2.2σ higher than the Muon g-2 Theory Initiative data-driven one.

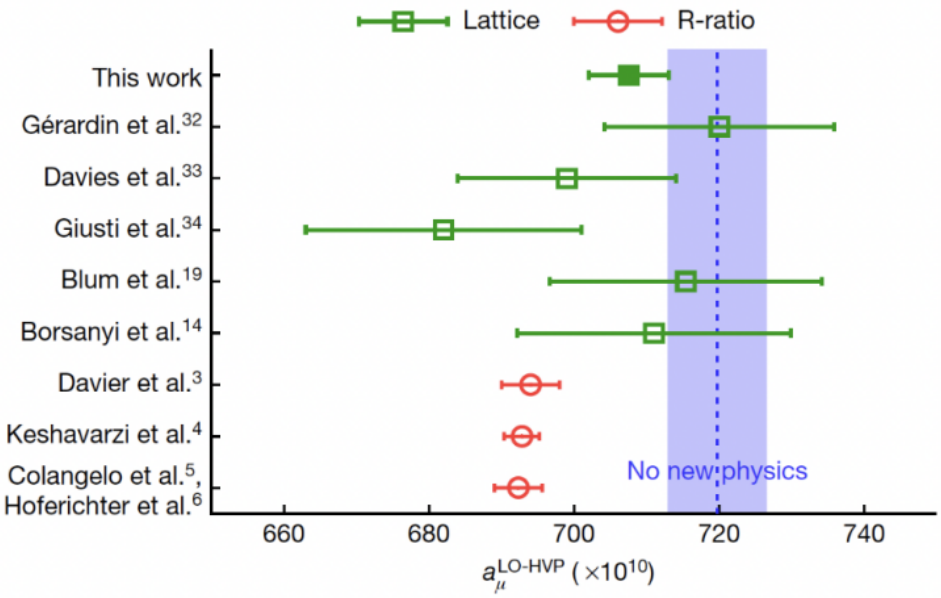

Figure 1.9: Latest lattice results from BMW collaboration in 2021

1.2.3 Hadronic Light-by-Light

The hadronic light-by-light process is the second largest source of uncertainty on the muon anomaly, even though its contribution is smaller. In fact, the HLbL contribution to the muon g-2 is suppressed by an extra power of the fine-structure constant α compared to HVP and indeed is about two orders of magnitude smaller: hence it does not need to be determined to the same level of accuracy. To meet the precision goal of the ongoing Fermilab experiment it suffices to know the HLbL contribution with about 10% relative accuracy. Unlike its QED counterpart, this contribution cannot be calculated in perturbation theory, and thus one should rely on either lattice QCD or data-driven evaluations, similarly to how it is done for the HVP contribution.

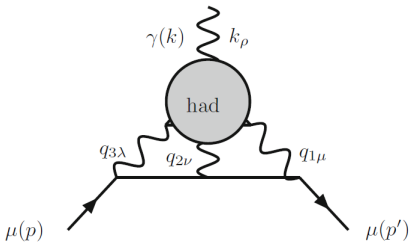

Figure 1.10: Feynman diagram of the hadronic light-by-light contribution.

Model based, past evaluations of HLbL before 2009 were summarized and combined with some new estimates in [8] and in the review by Jegerlehner and Nyffeler [9]:

$$a_\mu^{HLBL}(Glasgowconsensus) = 105(26) \times 10^{-11} \tag{1.24}$$

$$a_\mu^{HLBL}(Jegerlehner - Nyffeler) = 116(39) \times 10^{-11} \tag{1.25}$$

They are consistent with each other and are actually largely based on the same model calculations, but the estimates fall short of the present accuracy goal. Of even greater concern is the question of "model dependence" of these values and their uncertainties. Recently a new data-driven approach has been developed, based on a dispersive relation, providing a model-independent description of HLBL scattering which allowed a sizeable reduction of the uncertainty. The current estimates reported in [10] are:

$$a_\mu^{HLBL} = 92(19) \times 10^{-11} \tag{1.26}$$

$$a_\mu^{HLBL,NLO} = 2(1) \times 10^{-11} \tag{1.27}$$

1.3 Experimental measurements of a_μ

The measurement of a_μ has become more and more precise thanks to three experimental campaigns at CERN and and the more recent experiment of Brookheaven (BNL E821). The latest results for the muon anomaly comes from the experiment Muon g-2 at Fermilab National Accelerator Laboratory (FNAL) [11], that confirmed the previous measurements of BNL. The FNAl measurement, published the 7 April 2021, increased the experimental precision up to (0.46 ppm) and found a value for the muon anomaly of

$$a_\mu(FNAL) = 116592040(54) \times 10^{-11}. \tag{1.28}$$

After combination with previous measurements of both μ^+ and μ^-, the new experimental average

$$a_\mu(Exp) = 116592061(41) \times 10^{-11}(0.35ppm) \tag{1.29}$$

increases the tension between experiment and theory by 4.2 standard deviations.

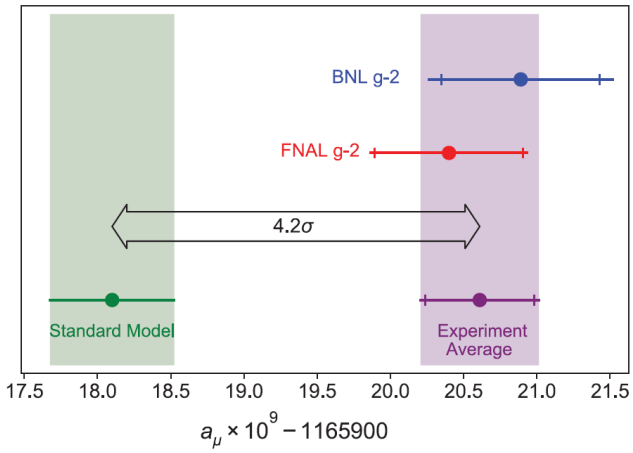

Figure 1.11: Comparison of theory and experiments for the muon anomaly. Figure from [12]

The experimental method for measuring the muon anomalous magnetic moment exploits the muon spin precession in presence of a uniform magnetic field. The frequency of precession is a consequence of the interaction between muons intrinsic magnetic moment and the magnetic field $\vec{B}$. When polarized muons are injected in the storage ring, the spin precession frequency ω_s is different from the cyclotron frequency ω_c. The two frequencies are defined as:

$$\vec{\omega}_s = -\frac{gq\vec{B}}{2m} - (1-\gamma)\frac{q\vec{B}}{\gamma m}, \quad \vec{\omega}_c = -\frac{q\vec{B}}{\gamma m} \tag{1.30}$$

The anomalous precession frequency ω_a is determined from the difference

$$\vec{\omega}_a = \vec{\omega}_s - \vec{\omega}_c = -\left(\frac{g-2}{2}\right)\frac{q\vec{B}}{m} = -a_\mu \frac{q\vec{B}}{m} \tag{1.31}$$

Since the muons are injected in storage rings, also the presence of the Electric field from electric quadrupoles, used to provide vertical focusing, must be taken into account. In the presence of both magnetic and electric fields, the expression for the anomalous precession becomes

$$\vec{\omega}_a = -\frac{q}{m}\left[a_\mu \vec{B} - \left(a_\mu - \frac{1}{\gamma^2-1}\right)\frac{\vec{\beta}\times\vec{B}}{c}\right]. \tag{1.32}$$

The coefficient $\vec{\beta}\times\vec{E}$ disappears at a certain value of the momentum called "magic momentum" that is $p_{magic} \simeq 3.09 \quad GeV/c.$ therefore, tuning the particles energy at exactly this value allows a precise measurement of a_μ from the values of $\vec{\omega}_a$ and $\vec{B}$.

The new FNAL experiment exploits the same concepts of the BNL one, but benefits of some improvements. The polarized muons, produced by parity-violating pion decay, are injected into the 1.45 T superconducting storage ring, same as BNL, but 2.5 times more uniform. Here the muon spin precession is measured exploiting the relation between muon spin and decay positron direction. High energy positrons are emitted preferentially in the same direction as the muon spin, so that the modulation due to the spin precession results in a modulation of the number of positrons above a fixed energy threshold observed in the calorimeters.

$$N(t) = N_0 e^{-t/\tau'}[1 + Acos(\omega_a t + \phi] \tag{1.33}$$

where N_0 is the total population at time t=0 and $\tau' = \gamma\tau = 64.4\mu s$ for FNAL, and τ is the muon lifetime. In fig.1.12, the divergence between the muon momentum and spin in a magnetic field in the case of $g > 2$ is shown. To detect the inward spiraling decay electrons, FNAL uses 24 calorimeters, each containing a 9×6 array of PbF_2 crystals read by SiPMs.

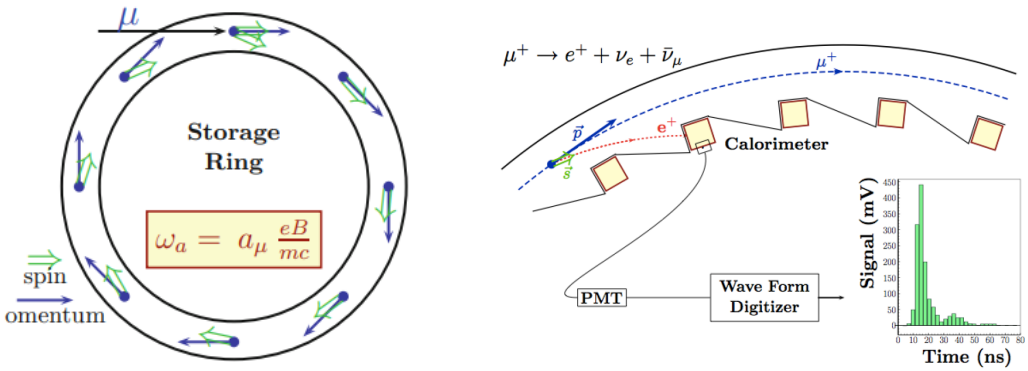

(a) (b)

Figure 1.12: Apparatus

The insert in fig.1.13 shows the number of events recorded in the calorimeters along time, which clearly manifest a sinusoidal behaviour, whose dominant frequency is extracted by a fourier analysis shown in the main figure panel.

To determine a_μ, ω_a is divided by the measure of the average magnetic field seen by the muons ω_p, that is measured very precisely using a pulsed-proton NMR probe. Therefore the muon anomaly is given by:

$$a_\mu = \frac{\omega_a}{\omega_L - \omega_a} = \frac{\omega_a/\omega_p}{\omega_L/\omega_p - \omega_a/\omega_p} = \frac{R}{\lambda - R} \tag{1.34}$$

where $\omega_L$is the Larmor precession frequency of the muon and $\lambda = 3.18334539(10)$ [13] is the muon-to-proton magnetic moment ratio. The value of R is determined by the experiment and so the muon anomaly is then extracted.

In fig.1.11 is visible how the theory and the experiments are still differing by numerous standard deviations. From the experimental side, to better understand the situation, higher precision should be achieved. This is the goal of FNAL g-2 experiment and of a new experiment at J-PARC [14], which will exploit a different experimental method to measure the muon anomalous magnetic moment.

Instead of running at the magic energy, to avoid the complication coming from the focusing electric field, the Japanese experiment will employ an ultra-cold muon beam. In this way the transverse momentum dispersion in significantly smaller and the beam can circulate in the storage ring without the focusing field. Such an ultra-cold beam can be produced from an ultra-cold muon source, where cold muons are produced from

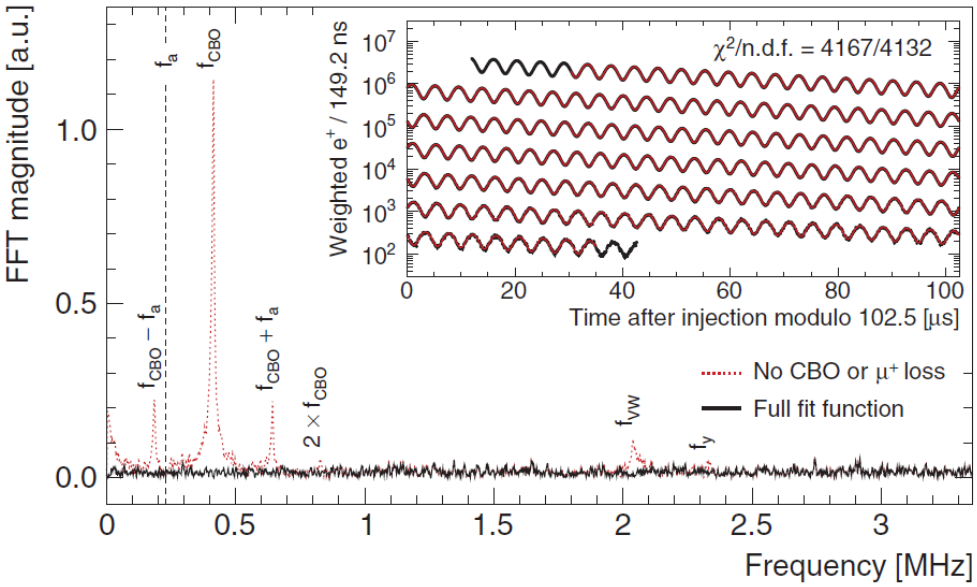

Figure 1.13: Fourier transform of the distribution of positron vs time of FNAL experiment.

the resonant laser-ionization of muonium (Mu). Since there is no electric field, any momentum can be "magic" momentum, and so even lower momentum can be used, thus reducing the size of the experimental apparatus. Having a single piece magnet allows a precise control of the magnetic field uniformity and allows for higher precision.

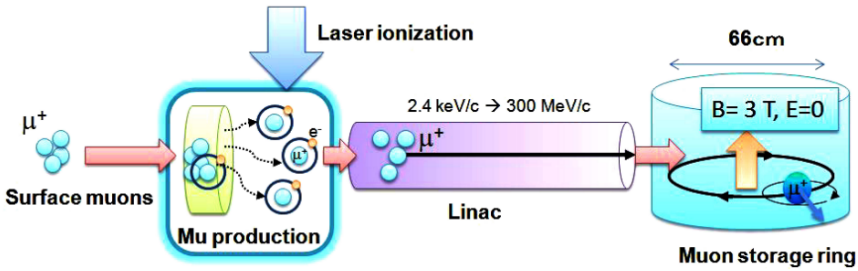

Figure 1.14: Layout of the experimental apparatus for the J-PARC g-2 experiment

Chapter 2

The MUonE experiment

The MUonE experiment aims to make and independent and very precise measurement of the leading order hadronic vacuum polarization contribute to the muon anomalous magnetic moment, in the space-like region [15]. To calculate this contribution, MUonE has to measure the hadronic part of the running of the electromagnetic constant, by the scattering of high energy muons on atomic electrons of a Beryllium target through the elastic process $\mu e \to \mu e$. The differential cross section of this process, measured as a function of the squared momentum transfer in the space-like domain, $t = q^2 < 0$, provide direct sensitivity to a_μ^{HLO}. This space-like approach is meant to reduce the uncertainty on the a_μ^{HVP} since, in this case, the dispersive integral won't be affected by the hadronic resonances in the low energy region.

2.1 Space-like hadronic vacuum polarization

In the time-like approach, the HLO contribution to the muon anomalous magnetic factor is given by the dispersive integral described by the equation (1.17). If we exchange the x and s integration in this equation, we can obtain the space-like dispersive integral [16]

$$a_\mu^{HLO} = \frac{\alpha}{\pi} \int_0^1 dx (x-1) \bar{\Pi}_{had}[t(x)] \tag{2.1}$$

where

$$\bar{\Pi}_{had}(t) = \Pi_{had}(t) - \Pi_{had}(0) = Re\bar{\Pi}(t) + Im\bar{\Pi}(t) \tag{2.2}$$

and

$$t(x) = \frac{x^2 m_\mu^2}{x-1} < 0 \tag{2.3}$$

is a space-like squared four-momentum.

The effective fine-structure constant, at squared momentum transfer q^2, can be defined as

$$\alpha(q^2) = \frac{\alpha}{1 - \Delta\alpha(q^2)} \tag{2.4}$$

where

$$\Delta\alpha(q^2) = -Re\bar{\Pi}(q^2) \tag{2.5}$$

For negative q^2, like in the space-like region, $Im\bar{\Pi}(q^2) = 0$. Therefore, the equation (2.1) can be rewritten as

$$a_\mu^{HLO} = \frac{\alpha}{\pi} \int_0^1 dx(x-1)\Delta\alpha_{had}[t(x)] \tag{2.6}$$

The hadronic shift, $\Delta\alpha_{had}[t(x)]$, can't be calculated from perturbation theory as it involves QCD contributions at low-energy scales. Anyway, it can be defined at LO starting from the effective coupling

$$\alpha(t) = \frac{\alpha(0)}{1 - \Delta\alpha(t)} \tag{2.7}$$

where $\alpha(0)$ is the fine structure constant and $\Delta\alpha(t)$ is the total shift

$$\Delta\alpha(t) = \Delta\alpha_{lep}(t) + \Delta\alpha_{had}(t) \tag{2.8}$$

The hadronic contribution $\Delta\alpha_{had}(t)$ can be extracted by subtracting the purely leptonic part $\Delta\alpha_{lep}(t)$ from $\Delta\alpha(t)$. The purely leptonic part can be calculated very precisely in QED. The final result then is:

$$\Delta\alpha_{had}(t) = 1 - \Delta\alpha_{lep}(t) - \frac{\alpha(0)}{\alpha(t)}. \tag{2.9}$$

This relationship is not true anymore at higher order, thus resulting in the need for a more complex expression that must be implemented in Monte Carlo simulations. While the

calculation's precision of the time-like integral was affected by the hadronic resonances, in the case of the master integral in the space like region of equation (2.6), the integrand is a smooth function as shown in fig. 2.1. Therefore, the computation of the integral is simplified. Furthermore, the running of alpha in the region of interest can be measured by a single scattering experiment, reducing the uncertainties due to handling data from different experiments. Up to date there are very few measurements of the running of α in the space-like region. The most precise one was obtained from OPAL experiment at LEP from small Bhabha scattering [17]. Based on this method [16], also the MUonE experiment wants to measure the hadronic running of $\alpha(t)$from $\mu e \to \mu e$ elastic scattering at low energies, allowing a completely independent estimation of a_μ^{HLO}.

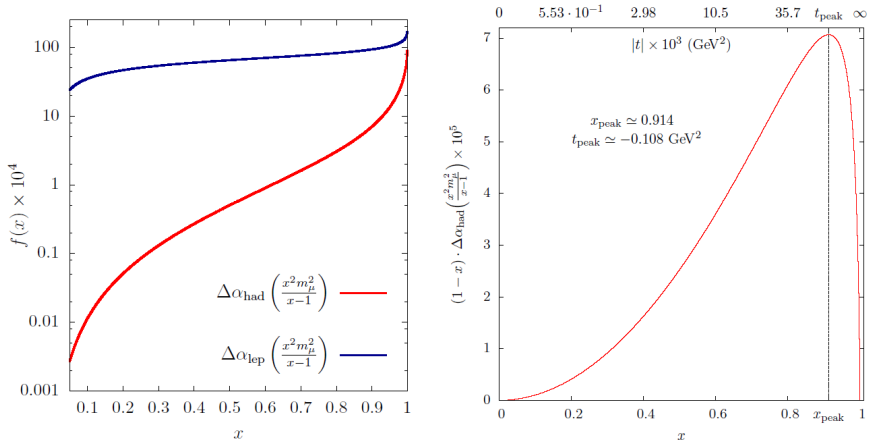

Figure 2.1: On the left, leptonic and hadronic contribution to the running of α^{QED} as a function of x. On the right, the integrand $(1-x)\Delta\alpha_{had}[t(x)]$ as a function of x and t.

2.2 Experimental Proposal

MUonE aims at measuring the hadronic part of the running of the electromagnetic coupling constant, in the spacelike region, by the scattering of high energy muons on atomic electrons on a low-Z target through the elastic process $\mu e \to \mu e$ [18]. MUonE will exploit the 150 GeV muon beam available at the CERN M2 beamline, scattering on atomic electrons of a fixed Beryllium target. The high energy of the muons beam allows the inspection of almost all the region of the integrand function seen in fig.2.1.

The MUonE experimental proposal is appealing for different reasons. First of all, the differential cross section of the involved process is measured as a function of the squared momentum $t = q^2 < 0$, and it provides sensitivity to the leading order hadronic contri-

bution to the muon anomaly. The dependence on the running of the coupling constant is described by the following relationship:

$$\frac{d\sigma}{dt} = \frac{d\sigma_0}{dt}\left|\frac{\alpha(t)}{\alpha(0)}\right|^2 \tag{2.10}$$

where $d\sigma_0/dt$ is the effective Born cross section. Moreover, the kinematic of the elastic scattering is well known and determined by angular observable. In fact, the angles of scattered electrons and muons are correlated, as will be described more in details in the next sections. In the fixed target $\mu e \to \mu e$ scattering is also possible to relate the value of t to the scattered electron energy according to the relation:

$$t = (p_\mu^i - p_\mu^f)^2 = (p_e^i - p_e^f)^2 = 2m_e^2 - 2m_e E_e^f \tag{2.11}$$

Finally, the boosted kinematics of the elastic scattering guarantees the containment of all events in a single homogeneous detector, since the angular deflection stays in a 50 mrad interval.

2.2.1 Precision requested for the measurements

The main challenge of MUonE proposal is to achieve the precision of 10^{-2} on α_{had}, that implies obtaining the precision of 10^{-5} on the shape of the differential cross section, which in order implies knowledge of the systematic uncertainties with about 10 ppm precision. The main contributions to the systematic effects can be divided into two categories: the experimental and the theoretical uncertainties.

- **Experimental systematic uncertainties** The requirements on the experimental side are: i) uniformity of the efficiency over all the q^2 range; ii) the correct alignment of the tracking stations and the inside elements; iii) correct description of the effect of multiple coulomb scattering, which breaks the muon electron angular correlation; iv) knowledge of the detector resolution to properly control the shape of the cross section.

- **Theoretical systematic uncertainties** In order to correctly extract $\Delta\alpha$ the Monte Carlo code for the process should be accurate to the Next to Next to Leading (NNLO) level of radiative corrections. The contributions included in the Monte Carlo event generator will be fully described in section 3.

2.2.2 Extraction of the hadronic contribution

As previously stated, when higher order corrections are duly taken into account, the dependence of the cross section on the running of the coupling costant becomes more complicated. In any case the hadronic contribution is determined from the ratio $R_{had(t)}$ between the observed cross section and the theoretical prediction evaluated for $\alpha(t)$ corresponding only to the leptonic running [19].

In the simplest case, at LO, this ratio is simply proportional to

$$R_{had}^{LO} = \left(1 - \frac{\Delta\alpha_{had}(t)}{1 - \Delta\alpha_{lep}(t)}\right)^{-2} \simeq 1 + 2\frac{\Delta\alpha_{had}(t)}{1 - \Delta\alpha_{lep}(t)} \tag{2.12}$$

At NLO the dependence is more complex and a Monte Carlo simulation is needed. The extraction of the hadronic contribution is then performed by a template fit method, which uses a parametrization for the hadronic contribution. The used parametrization is physically inspired to the one-loop QED calculation of vacuum polarisation induced by a lepton pair in the space-like region [18]:

$$\Delta\alpha_{had}(t) = k\left\{ -\frac{5}{9} - \frac{4M}{3t} + \left(\frac{4M^2}{3t^2} + \frac{M}{3t} - \frac{1}{6}\right)\frac{2}{\sqrt{1-\frac{4M}{t}}} log\left|\frac{1-\sqrt{1-\frac{4M}{t}}}{1+\sqrt{1-\frac{4M}{t}}}\right|\right\} \tag{2.13}$$

From the experimental side, the counting ratio can be define as a function of the experimental cross section, with respect to the MC simulated data

$$R_{had}^{LO} = \frac{d\sigma_{data}(\Delta\alpha_{had}(t) \neq 0)/dt}{d\sigma_{MC}(\Delta\alpha_{had}(t) = 0)/dt} = \frac{dN_{data}(\Delta\alpha_{had}(t) \neq 0)/dt}{dN_{MC}(\Delta\alpha_{had}(t) = 0)/dt} \tag{2.14}$$

The observable used for the analysis are the inclusive distributions of the muon and electron scattering angles, and also the two-dimensional distribution of the two. The analysis workflow can be summarized in the next points:

1. Construction of a detector with a good data quality in terms of event selection and rejection of background.
2. Redundant measurement of observables (scattering angles, electron energy) related to t.

3. Count of the number of signal events as a function of the momentum transfer t.
4. Extraction of the hadronic contribution to the running of α starting from the ration previously described, using the template fit method.
5. Computation of the dispersive integral in eq. (2.6) to get a_μ^{HLO}.

To reach the required precision, MUonE has to collect a final statistic of

$$N_{tot} = L \cdot \sigma_{\mu e} \sim 3.7 \times 10^{12} \tag{2.15}$$

that translates into 2 years of data taking with a energy of the beam of $150GeV$, with a rate of $\sim 1.3 \times 10^7 muons/s$, with a Be target of thickness d= 60 cm, guaranteeing an integrated luminosity of $1.5 \times 10^7 nb^{-1}$.

2.3 The elastic scattering process

Since the experimental proposal exploits the cross section of muon on electron elastic scattering, a deep knowledge of the process is needed. In fact, a proper selection of these events from the radiative background is crucial for the MUonE analysis. The event selection is supposed to be performed primarly by the tracking system [20], that will exploit the elastic relationship between the scattering angles. Anyway, event selection by mean of calorimetric measurements is also possible and is investigated in this thesis.

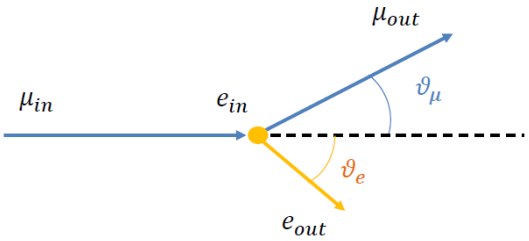

Figure 2.2: Representation of the elastic scattering $\mu \to e$ in the Laboratory frame

Before describing the useful properties of the elastic scattering, on which the experiment is based, it is important to study its kinematics. Schematically, the process is represented by

$$\mu^\pm(p_1)e^-(p_2) \to \mu^\pm(p_3)e^-(p_4) \tag{2.16}$$

where p_1 and p_3 are respectively the four momenta of the ingoing and outgoing muon,

and p_2 and p_4 the four momenta of the electron. At LO the interaction is mediated by photon in t-channel, carrying the transfered momentum t. The representation of the process in the laboratory frame is shown in fig.2.2. In this reference frame the four momenta are the folowing:

$$\begin{aligned} p_1 &= (E_\mu, p_\mu, 0, 0) \\ p_2 &= (m_e, 0, 0, 0) \\ p_3 &= (E_\mu^{'}, p_\mu^{'} cos\theta_\mu, p_\mu^{'} sin\theta_\mu, 0) \\ p_4 &= (E_e, p_e^{'} cos\theta_e, p_e^{'} sin\theta_e, 0) \end{aligned} \tag{2.17}$$

Moreover, since it is a fixed target experiment, the electron is initially at rest, thus the Mandelstam variables in the laboratory frame write as:

$$\begin{aligned} s &= (p_1 + p_2)^2 = (p_3 + p_4)^2 = m_\mu^2 + m_e^2 + 2me_e E_\mu \\ t &= (p_1 - p_3)^2 = (p_2 - p_4)^2 = 2m_e^2 - 2m_e E_e^{'} \\ s + t + u &= 2m_\mu^2 + 2m_e^2 \end{aligned} \tag{2.18}$$

For elastic scattering events, the squared transfer momentum is computable from the measurements of the energy of the scattered electron. The energy of the scattered electron is measured in the calorimeter, but also it is related to the scattering angle, once the energy of the muon beam is known. In fact, from the four momentum conservation, E_e is defined as:

$$E_e = m_e \frac{1 + r^2 cos^2\theta_e}{1 - r^2 cos^2\theta_e}, \qquad r = \frac{\sqrt{E_\mu^2 - m_\mu^2}}{E_\mu + m_e} \tag{2.19}$$

The maximum energy of the electron occurs for $\theta_e = 0$ and it corresponds to $E_{max} \simeq$ 139.8 GeV for the selected beam energy. While the scattered electron energy runs in the interval $[0, E_{max}]$, the momentum transfer ranges in the negative interval $[t_{min}, 0]$. The limit value t_{min} is defined as $t_{min} = -\lambda(s, m_\mu^2, m_e^2)/s$ and it is equal to -0.14289 GeV^2 for a muon beam of 150 GeV. The value of t_{min} corresponds to $x_{max} = 0.93212$, meaning that a muon beam of this energy allows the inspection of more than the 87% of the integrating region of the dispersive integral in eq. (2.6), from witch a_μ^{HLO} is obtained.

The elastic relationship between the scattering angles of muons and electrons can also be obtained by the conservation of four momenta. It relates the angles in the laboratory

frame and can be defined as:

$$tan\theta_\mu = \frac{2tan\theta_e}{(1+\gamma^2 tan^2\theta_e)(1+g_\mu*)-2} \tag{2.20}$$

where

$$g_\mu* = \frac{\beta}{\beta_\mu*} = \frac{E_\mu m_e + m_\mu^2}{E_\mu m_e + m_e^2} \tag{2.21}$$

and $\beta_\mu*$ is the muon velocity in the CMS. The elasticity curve, described by this relation, is shown in fig.2.3, and it represent the main experimental signature for elastic events, together with the requirement of planarity. On the other hand, the event selection based on elastic requirements on the angles is limited by the angular resolution of the tracking system, leading to a ambiguity in the association of the angles to the scattered particles. This ambiguity will be better described in section 4.2, and will be resolved by PID using calorimetric informations.

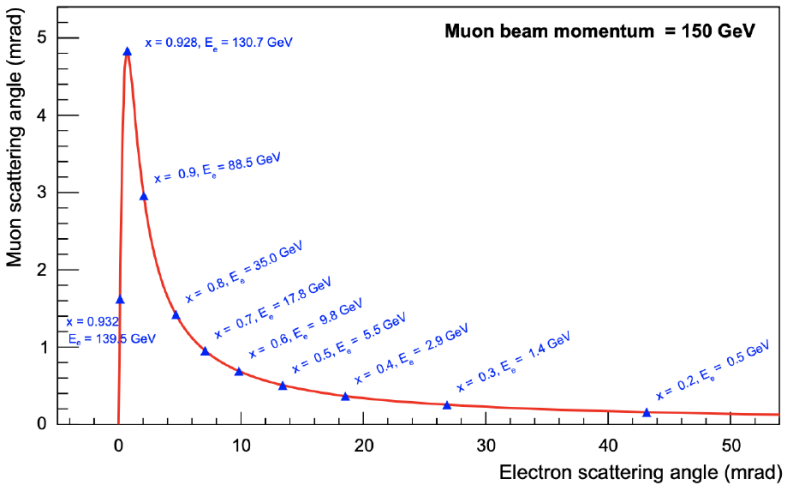

Figure 2.3: Elastic relationship between the muon and electron scattering angle at the muon beam momentum of 150 GeV

2.4 Experimental Set Up

The features of MUonE experimental apparatus are constrained by the request on the final precision needed in the measurement. Since the goal of the experiment is to precisely measure the shape of the differential cross section of the elastic process, a modular setup has been chosen in order to minimize the effect of the Multiple Coulomb Scattering. This way, the muon beam of 150 GeV from the CERN M2 beamline will impinge on a total Be target thickness of 60 cm, required to collected the necessary statistics, but sliced into 40 different layers, to minimize the MCS and recover the necessary resolution of the tracking system. As shown in fig.2.4, the final apparatus will then comprehend:

1. 150 GeV muon beam.
2. 40 identical tracking stations, each of them equipped with a 15 mm Beryllium (Be) target and three couple of Silicon (Si) sensors.
3. an Electromagnetic Calorimeter (ECAL) made by an array of PbWO4 scintillating crystals, read by Avalanche Photo Diodes (APDs).

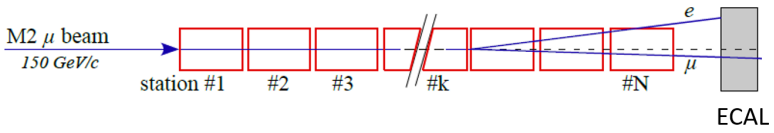

Figure 2.4: MUone experimental apparatus

2.4.1 Tracking system

The tracking system is crucial for the achievement of MUonE proposal, since it has to measure the muon and electron scattering angles. The efficiency of the detector must be uniform in all the q^2 range of interest, corresponding to an electron energy greater than 1 GeV. Giving that the energy of the muon beam is 150 GeV, the total angular acceptance of the detector must cover scattering angles of at maximum 30 mrad. Therefore, an active area of $10 \times 10\ cm^2$ for the tracking module is sufficient to contain all the kinematics of the events.

A Silicon detector based tracking system represents an ideal choice for MUonE since it guarantees: high spatial precision, compactness to allow modularity, high rate sustainability, high uniformity and efficiency and easy integration in the trigger system.

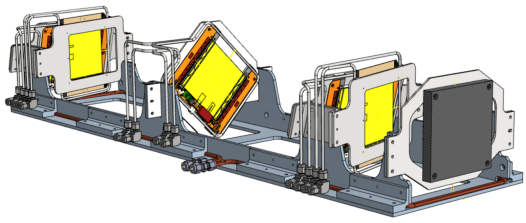

Figure 2.5: A single tracking station with the Si sensors and the Be target.

Tracking stations and alignment

The layout for the single tracking station is reported in fig.2.5. Each station will be one meter long, so the total length of the tracking system will be of 40 m, for the final apparatus. Up to today just two stations are completed and fully equipped and they will be tested, together with the ECAL, in a dedicated test beam in October 2022. Each tracking station is composed by the following elements:

1. a carbon fiber supporting structure
2. a target holder, whit the 15 mm thick Be target.
3. 6 Pt2S Silicon modules, organized in three couples.
4. Read out electronics for the Si sensors.

The first and the last couple of sensors are oriented in the (x,y) plane, while the intermediate couple is rotated of 45° in order to remove the degeneracy of the tracks. To optimize the hit resolution, the tilt of the (x,y) modules is being considered. This would maximize shower sharing in adjacent strips.

To determine the mean energy of the beam, the only way is to relay on the kinematic of the scattering, meaning that the precision on the energy measurement is related to the angular resolution. The angular resolution is then related to the spatial resolution of the alignment of the sensors inside the tracking station. In conclusion, to have the required precision of 2×10^{-5} on the energy of the incoming beam, having a 1m long station, a precision of $1\mu m$ is needed on the alignment of the sensors. Such request is very challenging. The solution that MUonE is adapting is to perform the alignment of the single tracking station by mean of Holographic Interferometry. The scheme for the proposed Holographic Alignment Module (HAM) is represented in fig. 2.6(b). The goal of this system is to monitor the relative distance between two tracking planes. The group

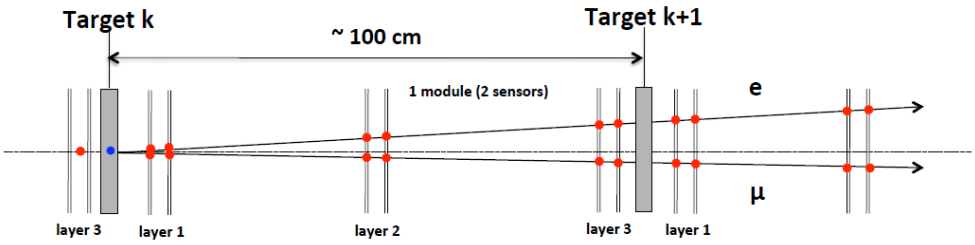

(a)

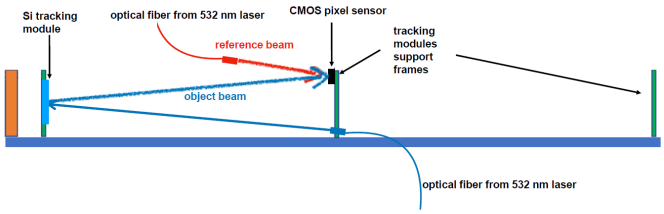

(b)

Figure 2.6: Schematic representation of a tracking station (a), Scheme for the Holographic Alignment Module (b).

of Trieste is already implementing the system to be ready for the test run of October 2022, and they plan to test it in the first tracking station. This system should be able to reach a precision of 0.25 μm that is much beyond the required precision of MUonE.

Silicon sensors

The sensors chosen for the MUonE tracking system are the 2S Silicon strip sensors developed for the CMS Tracker upgrade [21]. The relevant characteristics for the choice of the Si sensors were the sensors active area, the single hit resolution, the material amount and the front-end response time and maximum readout rate. The CMS 2S modules feature 2 micro strip sensors per module (5×10 cm^2), covering a final area of 10×10 cm^2, with a strip pitch of 90 μm. The number of strips for each sensor is 1016 and they are read by 8 ASIC chips (254 channels per chip). The total amount of material for each sensor cover a thickness of 320 μm. They are being assembled by the Perugia assembly group and already six of them are ready for the test run of October.

The read out rate required for MUonE is 40 Mhz. The two sensors are mounted together, with a gap of 1.8 mm, and are read by common front-end CBC ASICs to correlate the hits from the two sensors. This will also allow trigger purposes.

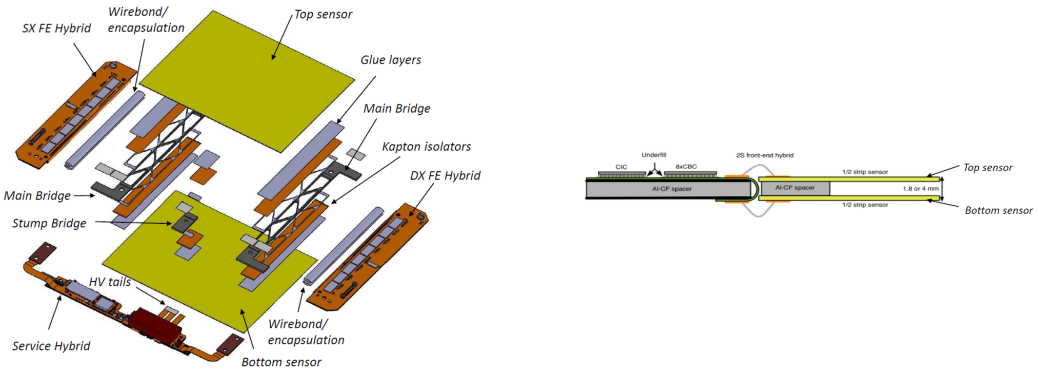

(a) (b)

Figure 2.7: Exploded view of a 2S module of the tracking system(a). Lateral view of the 2S module and the read out board (b).

2.4.2 The Electromagnetic Calorimeter

The forward Electromagnetic calorimeter (ECAL), covering all the detector acceptance, is an essential part of the experiment both for particle identification and event selection. In fact, a calorimetric measurement of the position of the electromagnetic shower could resolve the uncertainty on the discrimination of muons and electrons due to the finite angular resolution. At the same time, the measurement of the energy of the electromagnetic shower could also give information on the elasticity of each event, helping in the discrimination of signal events from backgrounds. Finally, the calorimetric measurement of the electron energy provides an alternative determination of the value of t. All these features of the ECAL will be investigated in detail in the next sections.

The proposed calorimeter for MUonE is homogeneous and will be composed by Lead Tungstate (PbWO4) scintillating crystals, already in use in the CMS Ecal. It will be placed downstream, after the tracking stations. To cover the angular acceptance of the detector, the final calorimeter should have a surface of 1m $\times$ 1m. The first version of this subdetector, that is the one that has been tested in the test beam of July 2022, and will be used in the test run of October 2022, is composed by an array of 5×5 crystals, covering a total surface of 14×14 cm^2.

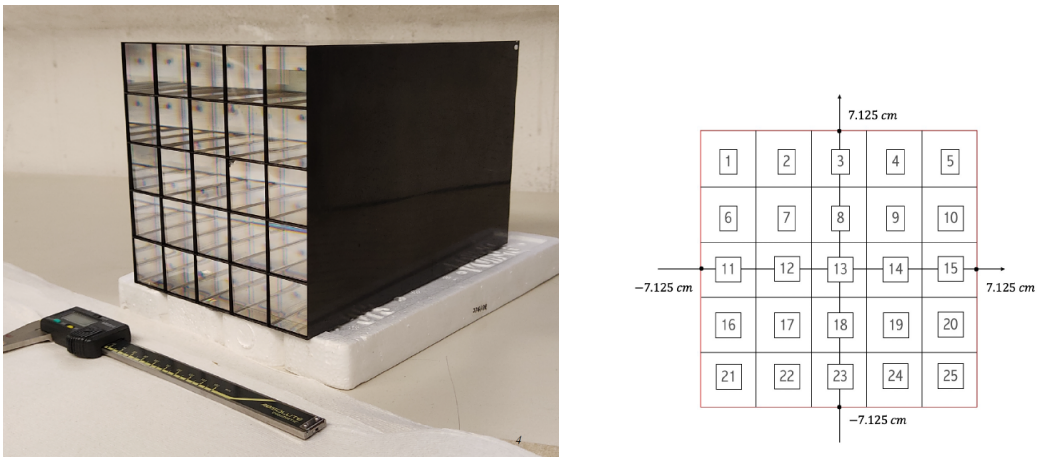

(a) (b)

Figure 2.8: Photo of the 5×5 array of crystals in the supporting structure (a). Schematic view of the surface of the calorimeter (b).

Chapter 3

Fast Simulation and event generation

The Fast Simulation code for the MUonE experiment is a parametric simulation that describes the effects of the detector on the particle characteristics (energy, momentum, position...). The need for a Fast and parametric simulations comes from the high computational challenge represented by the huge statistic needed for the precision required by MUonE. A preliminary simulation is crucial to have rapid feedback in this phase of development of the detector. The final analysis will then be performed with a complete simulation based on GEANT, that will also be used to tune the parameters of the Fast Simulation.

The Fast Simulation has already been used for the analysis of MUonE letter of intent [18] and its updates [20]. But is also has been used for studies of sistematics, and for the study of the setup for the test run of 2022 [22]. The new version of the code, updated to account for NNLO radiative corrections, has been used for the first time in this thesis work. The new code is also updated for the "embedded" use of MESMER MC event generator, meaning that while before the simulation was used only for the analysis of pre-generated sets of events, now the generation is part of the code itself and it is possible to run the (FORTRAN) generator and the (C++) fast simulation and analysis in the same process. The first part of this thesis was than dedicated to the update of the Fast Simulation in order to make the analysis part interact with the new NNLO events. In fact, the presence of more than one radiated photon was not foreseen in the old version, therefore parts of the code needed to be modified. More details on the structure of the

Fast Simulation will be presented in the next paragraphs.

3.1 The MESMER event generator

MESMER (Muon Electron Scattering with Multiple Electromagnetic Radiation) is a Monte Carlo event generator for high-precision simulation of muon-electron scattering at low energies, developed for the MUonE experiment.

On top of the leading order $\mu^{\pm}e^{-} \to \mu^{\pm}e^{-}$ the code includes:

1. NLO QED corrections, meaning events up to one extra virtual or real photon [23];
2. NNLO QED corrections, describing up to two extra virtual or real photons [24];
3. leptonic pair production and extra NNLO virtual leptonic corrections [25];
4. emission of a pion via $\mu^{\pm}e^{-} \to \mu^{\pm}e^{-}\pi^{0}$, with the pion decaying in to gammas [26].

While the last two corrections are included in the code but not public yet, the NLO were already included in all the analysis made with the Fast Sim previous to this thesis. The NNLO corrections instead have been used for the first time in this thesis and are described more in detail in this section.

3.1.1 NNLO corrections

The complete set of NNLO QED corrections along the electron line entering the process $\mu^{\pm}e^{-} \to \mu^{\pm}e^{-}$ consists of three parts with contributions due to virtual and real photons:

- virtual two loop corrections - diagrams of the type 1a and the irriducible 1b-1d.
- one-loop corrections to single photon emission given by diagrams as in 2a-2b.
- double bremsstrahlung process $\mu^{\pm}e^{-} \to \mu^{\pm}e^{-} + \gamma\gamma$ given by contributions as in 2c-2d.

All the above contributions are infrared-divergent quantities. The IR divergences are regularized by means of a small photon mass and a slicing photon energy parameter to separate soft from hard real radiation [24]. The total contribution up to NNLO accuracy implemented in the MESMER MC generator can be summarized by the formula:

$$d\sigma^{NNLO} = d\sigma^{\alpha^0} + d\sigma^{\alpha^1} + d\sigma^{\alpha^2} \tag{3.1}$$

where the $d\sigma^{\alpha^0}$ describes the tree level contributions and $d\sigma^{\alpha^1}$ the NLO contributions.

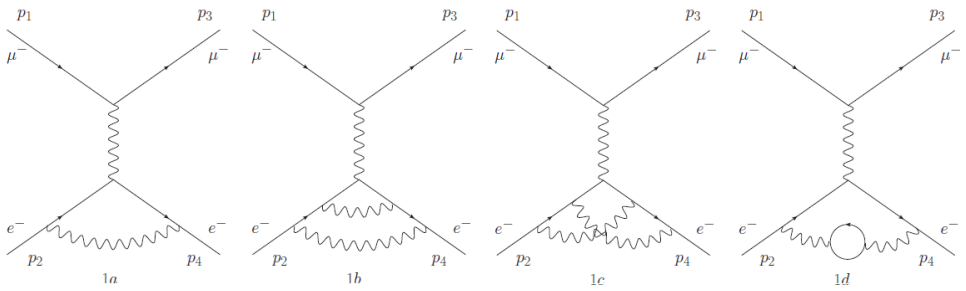

Figure 3.1: Virtual QED corrections to the electron line. One-loop correction (diagram 1a); sample topologies for the two-loop corrections (diagrams 1b-1d).

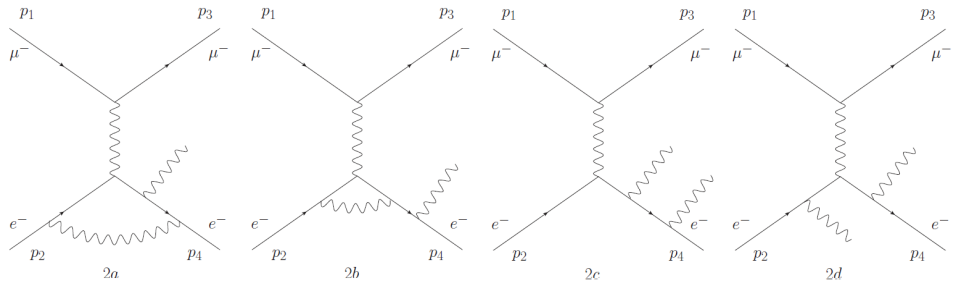

Figure 3.2: Sample diagrams for the one-loop QED corrections to single photon emission (diagrams 2a-2b); sample diagrams for the double bremsstrahlung process (diagrams 2c-2d).

The final MUonE analysis, for the calculation of the hadronic contribution to the muon anomaly, will include all these new contributions. The analysis presented in the MUonE letter of intent that pointed out the feasibility of the experiment proposal have then to be counter-checked including these corrections. Anyway, a phenomenological study of the different observable used in the analysis [24], points out that the size of the NNLO corrections, with respect to the LO differential cross-sections, is at the level of a few 10^{-4} for several regions of phase space in the presence of acceptance cuts only, leaving some corners of phase space where the corrections can grow up to the per cent level. Hence, the results from the LOI analysis are not expected to change. As a first step towards the complete inclusion of NNLO corrections in the MUonE experiment analysis, one of the activity of this thesis work consisted in the reproduction of previous studies, to check whether the presence of NNLO correction in the generated sample of events had some impact on the final results. The complete process is described in details in the next sections.

3.1.2 Photons energy distribution

The main practical difference related to the inclusion of NNLO radiative corrections in the MC generator is the possibility of having up to two real photons in the final state of the simulation. The emission of one or more photons spoils the two body kinematics and the calorimeter can be used to discard these background events, as will be shown in the next sections. However, the emission of the photons is collinear to the electron direction. Therefore, the purely calorimetric measurement of the variable t is not perturbed by the final state radiation. From the MC sample of data is possible to investigate how many photons are expected in the final state of the collected events. The number of events with 0,1 or 2 emitted photons, for events including only NLO corrections and also NNLO corrections, are displayed in the graphs of fig. 3.3. The percentage of the different final states, for different photon energy thresholds, are also shown in table 3.1.

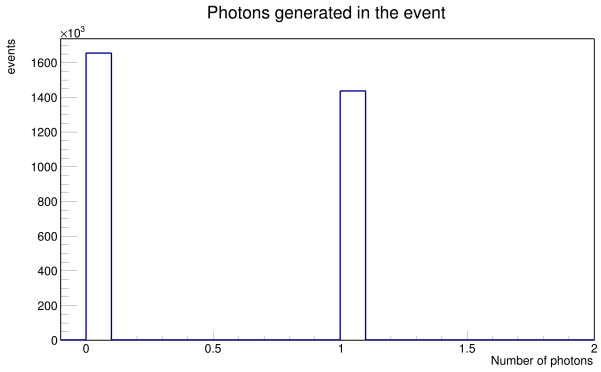

(a)

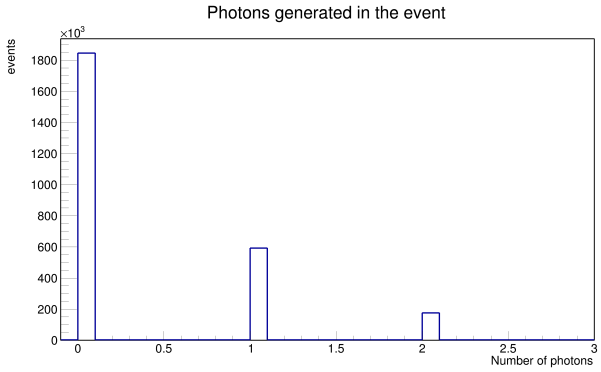

(b)

Figure 3.3: Number of events with 0,1 or 2 real photons in the final state for NLO events (a), and NNLO events (b).

		0 photons	1 photon	2 photons
NLO	all	53.3%	46.5%	-
NNLO	all	59.4%	30.6%	10.0%
	$E_\gamma > 1MeV$	59.4%	28.1%	8.9%
	$E_\gamma > 10MeV$	59.4%	24.9%	7.6%
	$E_\gamma > 100MeV$	59.4%	19.2%	5.6%

Table 3.1: Distribution of the final states, with different photon energy thresholds.

It is interesting to notice that the emitted photons have a low energy, very few of them have an energy higher than 100 MeV. Also, in the events with one or more photons, the electron energy distribution is shifted towards lower energies closer to zero, since part of the energy is transferred to the photons. In fig. 3.4, the total energy distribution of the electron is divided into the three contributions. The bulk of electrons with low energy is represented by the final states with one or two photons, while the electron energy for elastic events has a peak around 1 GeV.

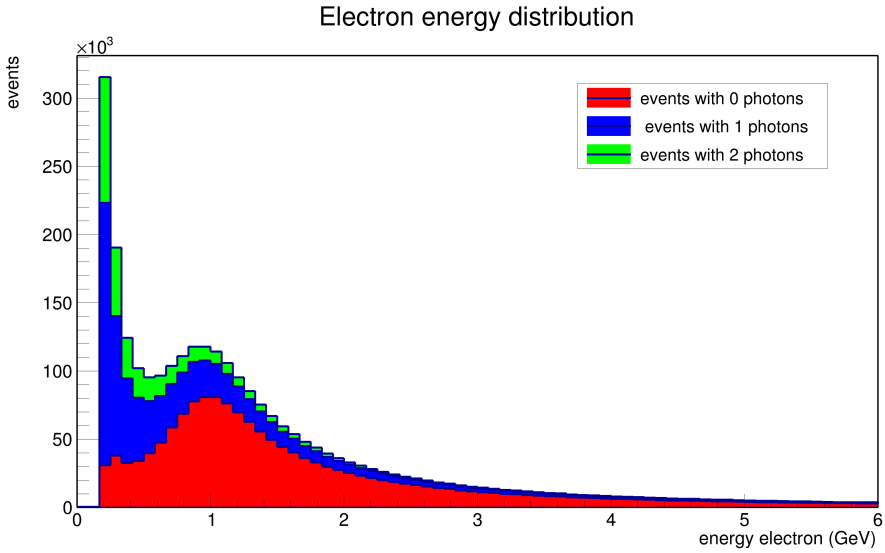

Figure 3.4: Virtual QED corrections to the electron line. One-loop correction (diagram 1a); sample topologies for the two-loop corrections (diagrams 1b-1d).

3.2 The Fast Simulation of the Test Run apparatus

The Fast Simulation developed for MUonE is a parametric simulation needed for preliminary analysis due to the large amount of statistic required. In fact, a parametric simulation reduce the power consumption and the amount of time necessary to analyse a large sample of data. As stated before, the new version of the simulation is configured to run together with the MESMER MC event generator, so it is possible to divide the full package into a first generation phase plus the description of the detector, including the propagation of the particle along the detector, and a final analysis of the data. This final analysis than can be compared with the experimental data. The MC event generator was described in the previous subsection. In the next pages, the layout of the detector description inside the code is provided.

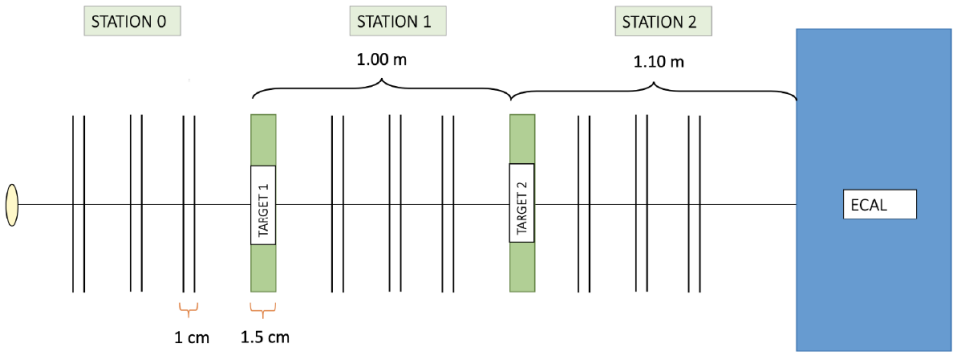

Figure 3.5: Graphical layout of the Test Run experimental apparatus from [22].

The version of the code used in this thesis work, describes the MUonE experimental apparatus foreseen for the Test Run of October 2022 and was developed by E. Spedicato in her master thesis work *"Fast simulation of the MUonE 2021 Test Run setup"* [22]. The Test Run, rescheduled for October 2022, will see for the first time two tracking stations and the electromagnetic calorimeter (5×5 crystals array) working together. In the fast simulation the following characteristics of the setup are included:

- Beam spot and divergence of the muon beam.
- Multiple Coulomb Scattering of electrons and muon with the Beryllium targets and the Silicon layers of the sensors.
- Parameterization of the electromagnetic showers generated by electrons and pho-

tons inside the ECAL.

The code was updated to work with in the "embedded" mode, together with the MESMER generator, and also slightly modified to account for the higher numbers of photons.

3.2.1 Beam Spot and Divergence

The MUonE experiment will employ the upgraded M2 muon beam available at the CERN SPS [27]. The muon beam has an energy of $E_\mu = 150GeV$, with a beam spread of the order of 3%. The cross section of the beam in the plane perpendicular to its motion, beam spot, is characterized by the parameters $\sigma_x = 26$ mm and $\sigma_y = 27$ mm [18]. The dimension of the beam has been taken into account in the simulation and the generated muons have been assigned a random coordinate, according to a Gaussiang distribution:

$$\begin{aligned} x_R &\to \text{Gauss}(0, \sigma_x) \\ y_R &\to \text{Gauss}(0, \sigma_y). \end{aligned} \tag{3.2}$$

The beam also has an angular divergences of $\sigma_{x'} = 0.27\,mrad$ on the XZ plane and $\sigma_{y'} = 0.27\,mrad$. The divergence was also taken into account in the simulation of the incoming beam by mean of Gaussian distribution in the initial angles θ_x and θ_y.

$$\begin{aligned} \theta_x &\to \text{Gauss}(0, \sigma_{x'}) \\ \theta_y &\to \text{Gauss}(0, \sigma_{y'}) \end{aligned} \tag{3.3}$$

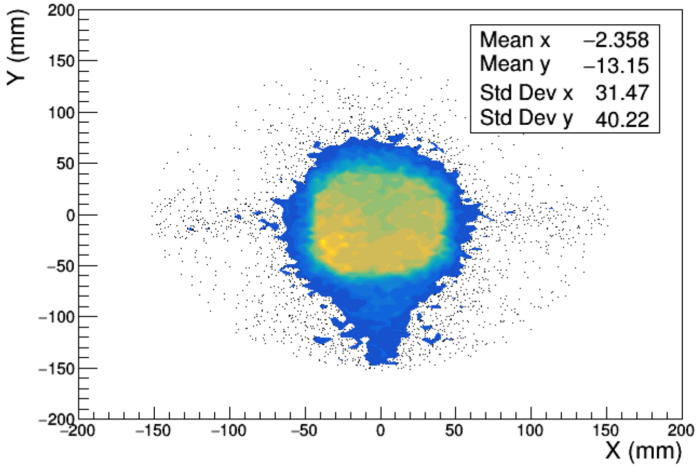

Figure 3.6: Virtual QED

The kinematical properties of the incoming muon beams impact also on the properties of the outgoing particles in the final state. In fact, due to the angular divergence, the direction of the incoming muon beam is no more aligned with the z-axis but it is rotated in agreement with the divergence of the beam. Therefore also the momenta of all the outgoing particles, from the interaction with the target, have to be rotated by consequence. As a first step, the incoming muon momentum is modified the new components are calculated according to:

$$\begin{cases} P'_z = \sqrt{\frac{|\vec{P}_{in}|}{1+tan^2(\theta_x)+tan^2(\theta_y)}} \\ P'_x = P'_z \tan(\theta_x) \\ P'_y = P'_z \tan(\theta_y) \end{cases} \tag{3.4}$$

The new vector still has the same absolute value, it is only rotated. Then the final momenta of the outgoing particles are rotated using a rotation matrix R:

$$R = R_{x'} R_y = \begin{pmatrix} \cos\psi & 0 & \sin\psi \\ -\sin\varphi\sin\psi & \cos\varphi & \sin\varphi\cos\psi \\ -\cos\varphi\sin\psi & -\sin\varphi & \cos\varphi\cos\psi \end{pmatrix}. \tag{3.5}$$

where the two angles are defined by the components of the incoming muon momenta:

$$\psi = arctan\left(\frac{P'_x}{P'_z}\right) \tag{3.6}$$

$$\varphi = arctan\left(\frac{P'_x}{\sqrt{P'^2_x + P'^2_z}}\right) \tag{3.7}$$

After being rotated, the outgoing particles are propagated through all the remaining layers of the tracking stations until they impinge on the surface of the electromagnetic calorimeter. The interaction with the detector layers also have an impact on the trajectories, both on the incoming muon, before the scattering in the target, and on the outgoing particles. This phenomenon is called Multiple Coulomb Scattering (MCS).

3.2.2 MCS and particles propagation

Charged particles traversing a material are deflected by many small-angle scatterings with the atoms of the medium. The net scattering and displacement distributions are

Gaussian according to the central limit theorem and are well-represented by the theory of Moliére [28]. In MUonE experiment, the incoming muons have to pass through several Silicon layers, and sometimes also Be layers, before interacting with the electrons in one of the targets. Therefore, the MCS with all these layers has to be taken into account. The modularity of the detector helps reducing the probability of multiple scattering, but only with simulations it is possible to quantify the effect on the trajectories of the particles. In the simulation from [22], no energy loss effect due to radiative processes, like Bremmsstrahlung have been considered, hence the particles conserve the energy along their path. Also, the photons were considered as propagating in straight lines, as the pair production process in the tracking stations is not yet implemented.

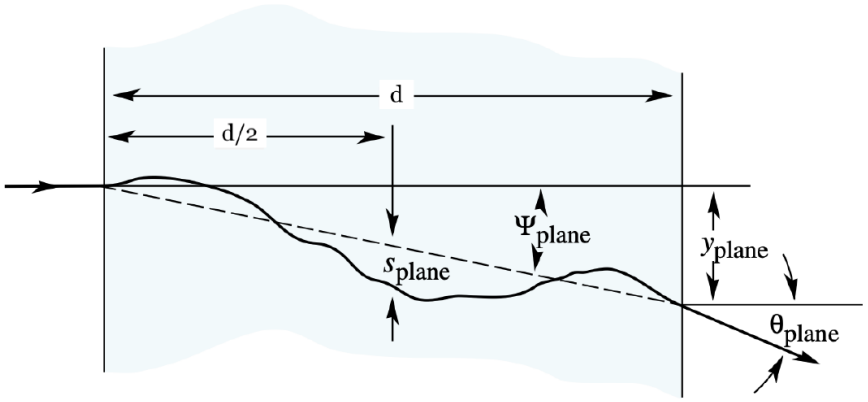

Figure 3.7: Virtual QED

Each time a muon or an electron traverses a target or a silicon layer, in the simulation the i-th exit angles are generated following a Gaussian distribution [29]:

$$\begin{aligned} \theta^i_{XZ} &\rightarrow \text{Gauss}(\,\theta^{i-1}_{XZ},\,\theta_0), \\ \theta^i_{YZ} &\rightarrow \text{Gauss}(\,\theta^{i-1}_{YZ},\,\theta_0). \end{aligned} \tag{3.8}$$

where

$$\theta_0 = \frac{13.6}{E\,(MeV)}\sqrt{\frac{d}{X_0}}\left[1 + 0.038\cdot \ln\frac{d}{X_0}\right] \tag{3.9}$$

The parameter of the Gaussian distribution depends on the thickness d and on the radiation lenght X_o of the material, and on the energy E of the incoming particle. Also the exit coordinates are redefined applying a Gaussian smearing on the entrance

coordinates as described by:

$$\begin{aligned} x^i_{out} &\rightarrow \text{Gauss}(x^i_{in},\ \frac{1}{\sqrt{3}} d\,\theta_0), \\ y^i_{out} &\rightarrow \text{Gauss}(y^i_{in},\ \frac{1}{\sqrt{3}} d\,\theta_0), \end{aligned} \tag{3.10}$$

After the propagation through the tracking stations, keeping into account the effect of MCS and the initial beam spot size and divergence, the transversal profile of the coordinates of the outgoing muons and electrons, at the surface of the electromagnetic calorimeter, are as shown in fig. 3.8.

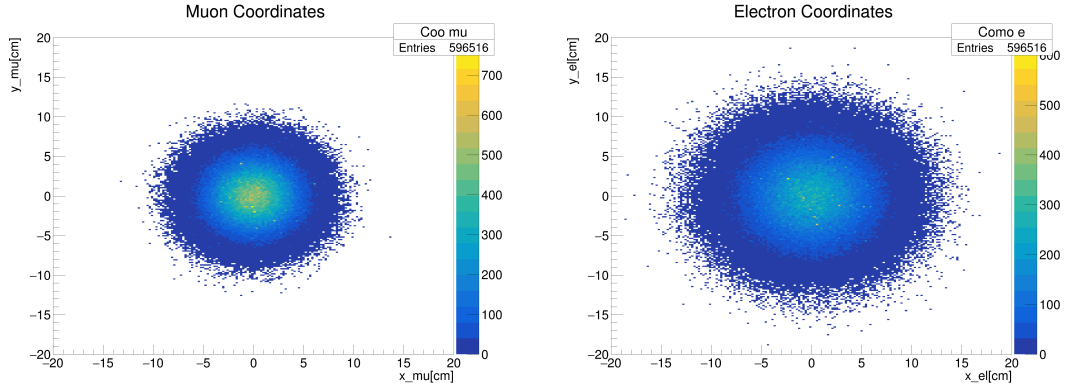

(a) (b)

Figure 3.8: Impact coordinates of the outgoing muons (a) and electrons (b) on the surface of the calorimeter. The coordinates origin (0,0) corresponds to the center of the calorimeter surface.

3.2.3 Electromagnetic shower parametrization

In the last part of the Fast Sim, also the interaction of the outgoing particles with the electromagnetic calorimeter is described. While the outgoing muons cross the ECAL, releasing only a small fraction of their energy inside the crystals, electrons and photons are absorbed by the medium. Electromagnetic calorimeters are specifically designed to measure the energy of particles exploiting the process of electromagnetic showers. When an electron or a photon enters in the calorimeter they start interacting with the medium and lose energy. For energy lower than $\sim 10\,MeV$ electrons lose energy by ionization and thermal excitation of the atoms of the material and photons interact via Compton scattering and photoeletric effect . When the energy increases, the main source of energy loss for electrons is Bremmstrahlung, while photons produce mainly electron-positron pairs. As a consequence of these processes electrons and photons in the calorimeter

produce secondary photons or electron-positron pairs. The secondary particle in turn produce other particles giving rise to a cascade (shower) of particles. A schematic view of the shower development is displayed in the fig. 3.9. The energy of the particles is progressively degraded until it is not sufficient anymore to produce new particles and it is mainly dissipated through ionization and excitation. This low energy threshold is called critical energy E_c.

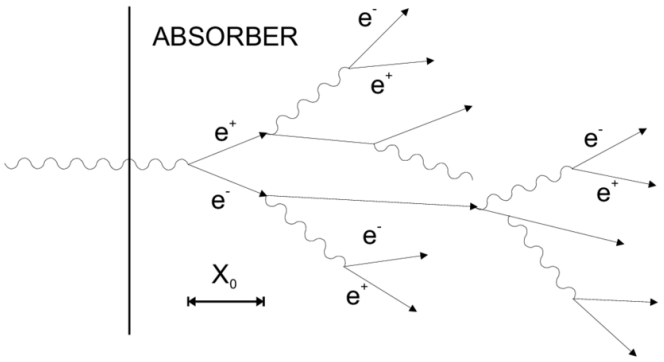

Figure 3.9: Virtual QED

The critical energy depends on the atomic number of the absorbent material and on its radiation length as follows:

$$E_C = 2.66 \left(X_0 \frac{Z}{A} \right)^{1.1} \tag{3.11}$$

The radiation length of a material represents the path after which the energy of the electron is reduced by a factor $1/e$. Photons do not lose energy but convert into electron positron pairs: the probability for a photon to survive $\frac{7}{9}X_0$ path is equal to $1/e$. The radiation length is approximated by:

$$\frac{1}{X_0} = \frac{4\alpha N_A Z(Z+1) r_e^2 \ln(183 Z^{-1/3})}{A} \tag{3.12}$$

where N_A is the number of Avogadro and X_0 is measured in g/cm^2. In the Fast Simulation developed in [22], the shower has been modeled with the GFLASH parameterization by G. Grindhammer and S. Peters in [30][31]. This method was already use for the shower parameterization in the Fast Simulation of the CMS experiment electromagnetic calorimeter as described in [32]. The CMS ECAL is made of the same crystals of MUonE and it has a similar readout electronics.

In the GFLASH parameterization, the spatial energy distribution of the shower is divided

into three probability density functions (PDF):

$$\mathrm{d}E(\vec{r}) = Ef(t)\mathrm{d}tf(r)\mathrm{d}rf(\phi)\mathrm{d}\phi \tag{3.13}$$

where E is the energy of the impacting particle in units of E_c. The three PDFs represent the three contributes to the spatial shower development.

- $f(t)$ represents the longitudinal profile of the shower as a function of t, shower depth in units of X_o.
- $f(r)$ represents the lateral profile as a function of r, the radial distance in units of the Moliére radius R_M.
- $f(\phi)$ is the azimuthal distribution, assumed uniform.

All the material dependent parameters have been summarized in the next table. These values are in common for CMS and MUonE electromagnetic calorimeters since the material is the same, PbWO4, and also the lenght of the crystals is the same, $l = 22\,cm = 24,7\,X_0$.

$\rho = 8.28$ g/cm^3	$X_0 = 7.37$ g/cm$^2 = 0.89$ cm
$A_{eff} = 170.87$	$E_C = 8.74$ MeV
$Z_{eff} = 68.36$	$R_M = 2.19$ cm

Longitudinal parameterization The mean longitudinal profile of a shower is described by a gamma distribution:

$$f(t) = \left\langle \frac{1}{E}\frac{dE(t)}{dt} \right\rangle = \frac{(\beta t)^{\alpha-1}\beta e^{-\beta t}}{\Gamma(\alpha)} \tag{3.14}$$

The longitudinal position of the shower maximum is $T = (\alpha - 1)/\beta$. In calorimeters with thickness $\simeq 25\,X_0$, the shower longitudinal leakage beyond the end of the active detector is much less than 1% up to incident electron energies of $\sim 300GeV$. In case of MUonE ECAL, the length of the active detector is $\sim 24,7\,X_0$, so the expected leakage is about 1% of the total energy of the particle.

Radial parameterization The radial parameterization runs in function of r that is the radial distance in units of the Moliére radius R_M. The Moliére radius is defined as

$$R_M = X_0\frac{21.2\text{ MeV}}{E_C} \tag{3.15}$$

and it expresses the transversal size of the shower. The 90% of the shower is contained within a radius of R_M. The transversal section of MUonE crystals is of $2.85 \times 2.85\, cm^2$, that is comparable to the Moliére radius of PbWO4 material.

The radial distribution is defined by two components, as shown in the formula:

$$\begin{aligned} f(r) &= \frac{1}{E}\frac{dE(t,r)}{dr} = \\ &= p\frac{2rR_C^2}{(r^2+R_C^2)^2} + (1-p)\frac{2rR_T^2}{(r^2+R_T^2)^2}\,, \end{aligned} \tag{3.16}$$

Here R_C (R_T) is the median of the core (tail) component and p is a probability giving the relative weight of the core component.

$$\begin{aligned} R_C(\tau) &= z_1 + z_2\tau \\ R_T(\tau) &= k_1\big(exp\left[k_3(\tau-k_2)\right] + exp\left[k_4(\tau-k_2)\right]\big) \\ p(\tau) &= p_1 \cdot exp\left(\frac{p_2-\tau}{p_3} - exp\left[\frac{p_2-\tau}{p_3}\right]\right) \end{aligned} \tag{3.17}$$

More details on the shower parametrization and the code description can be found at [22]. Whit the addition of NNLO corrections, so with the possibility of having two photons, the shower parameterization does not change. In principle, up to three different showers will develop in the detector and are duly represented in the simulation: it should be noted, however, that the photons are collinear with the electron so that, in the reconstruction phase, the three showers are summed up in a single measurement, which determines then the energy of the electron before radiation in vacuum.

Chapter 4

The Electromagnetic calorimeter

The primary goal of this thesis work is to study the calorimeter performances both with simulation and from the experimental side, studying the data from a dedicated test beam. The aim is to investigate the role of the calorimeter for the MUonE experiment in the achievement of different tasks as Particle Identification and selection of elastics events. In addition, the potential for an alternative determination of t from the energy deposit in the calorimeter will be inspected, allowing a comparison with the results from the tracking system.

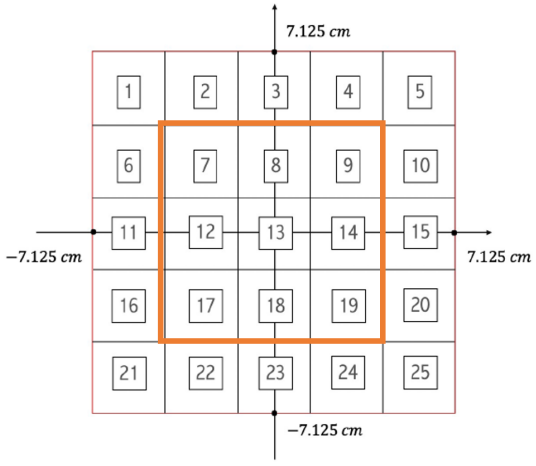

Figure 4.1: Schematic view of the crystals array. Only events in which the electron where impinging in one of the nine central crystals were chosen for the analysis.

4.1 Response of the ECAL

The measurement of energy with an electromagnetic calorimeter is based on the principle that the energy released in the detector material by the charged particles of the shower, mainly through ionization and excitation, is proportional to the energy of the incident particle [33]. To show that a measurement of the signal produced by the charged tracks of the cascade provides a measurement of the original particle energy E_0, it is useful to define the total track length of the shower T_0.

$$T_0(g/cm^2) \propto X_0 \frac{E_0}{\epsilon} \tag{4.1}$$

The term E_0/ϵ indicates the number of particles in the shower and ϵ is a material dependent parameter. In the case of MUonE homogeneous calorimeter, the measurement is performed by collecting the light produced by the scintillating crystals. The intrinsic resolution of an ideal calorimeter, without considering instrumental effects, is mainly due to the fluctuations on the number of particles in the shower. Since the shower development is a stochastic process, the intrinsic resolution is given by[33]:

$$\sigma(E) \propto \sqrt{T_0} \tag{4.2}$$

Therefore the dependence of the fractional energy resolution is the following:

$$\frac{\sigma(E)}{E} \propto \frac{1}{\sqrt{T_0}} \propto \frac{1}{\sqrt{E_0}} \tag{4.3}$$

The actual energy resolution of a realistic calorimeter is deteriorated by other contributions and can be written in a more general way as:

$$\frac{\sigma(E)}{E} = \frac{a}{\sqrt{E}} \oplus \frac{b}{E} \oplus c \tag{4.4}$$

The energy resolution is described by three terms in quadratic sum. The first term is called "stochastic term", and is the one mentioned above depending on the shower fluctuations and on the efficiency of photoelectron collection in the photosensors. The second term is the "noise term" due to the electronic noise of the readout chain. The last term is the "constant term" due to detector non-uniformities, shower leakage, knowledge of calibration constants, etc. More details on the nature of these three term are given in [33].

The study the energy resolution of the calorimeter has bben performed by simulating an electron beam of different energies impinging on the surface of the ECAL. The chosen energies are E_{true} = 0.25, 0.5, 1, 2, 2.5, 5, 10, 25, 50, 75, 100, 120 GeV. Only events in which the electron impinged in one of the nine central crystals of the calorimeter were chosen, as shown in fig. 4.1. The reason for this particular choice derived from a previous study of [22], were it was established that the mean energy reconstructed in an array of 3×3 crystals, around the seed crystal, was $\sim 95\%$. Excluding from the analysis events impacting on the frame of the calorimeter guarantees that the analysis is not spoiled by events not completely reconstructed . In the future also these frame events could be recovered by means of specific algorithms or machine learning techniques.

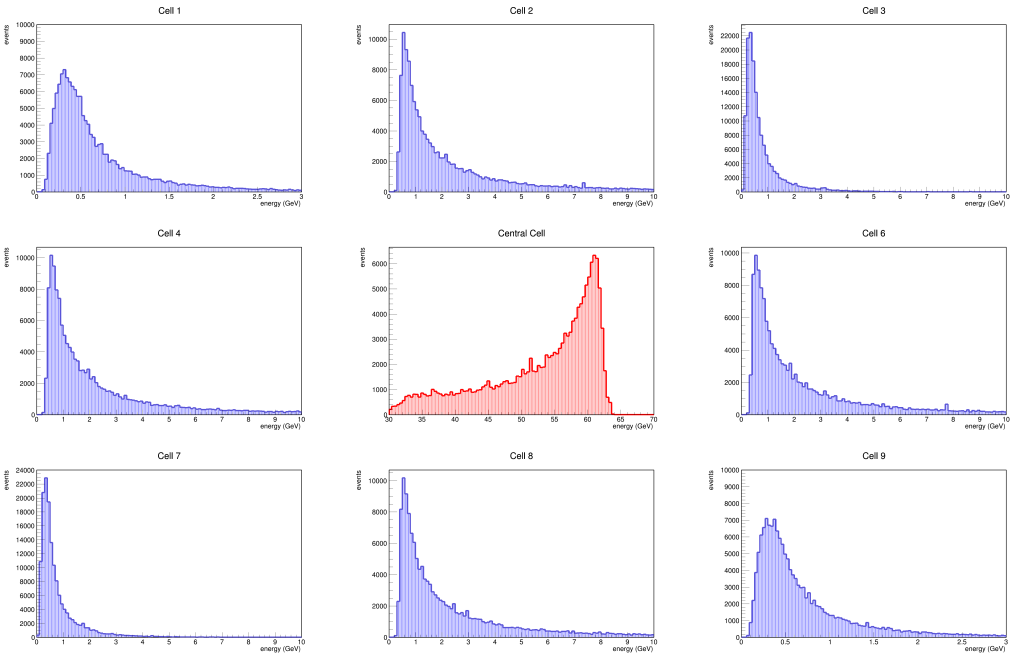

Figure 4.2: Example of energy distribution inside the nine crystal for a electron beam of 75 GeV

Fig. 4.2 shows the energy distribution in all the 3 cells, for the sample with E_{true} = 75 GeV. The electrons were impacting on the ECAL surface with different angular directions, not only along the z-axis. From the graph it is visible how the main fraction of the energy is deposited inside the seed cell (in red), while in the corner cells the energy deposited is less than 1 GeV. For each event of the sample the energy reconstructed by the calorimeter was defined as $E_{reco}(3 \times 3)$ and it is the sum of the energy deposited in the 9 cells array. The distributions of $E_{reco}(3 \times 3)$ for the various energies E_{true} are reported in fig. 4.3.

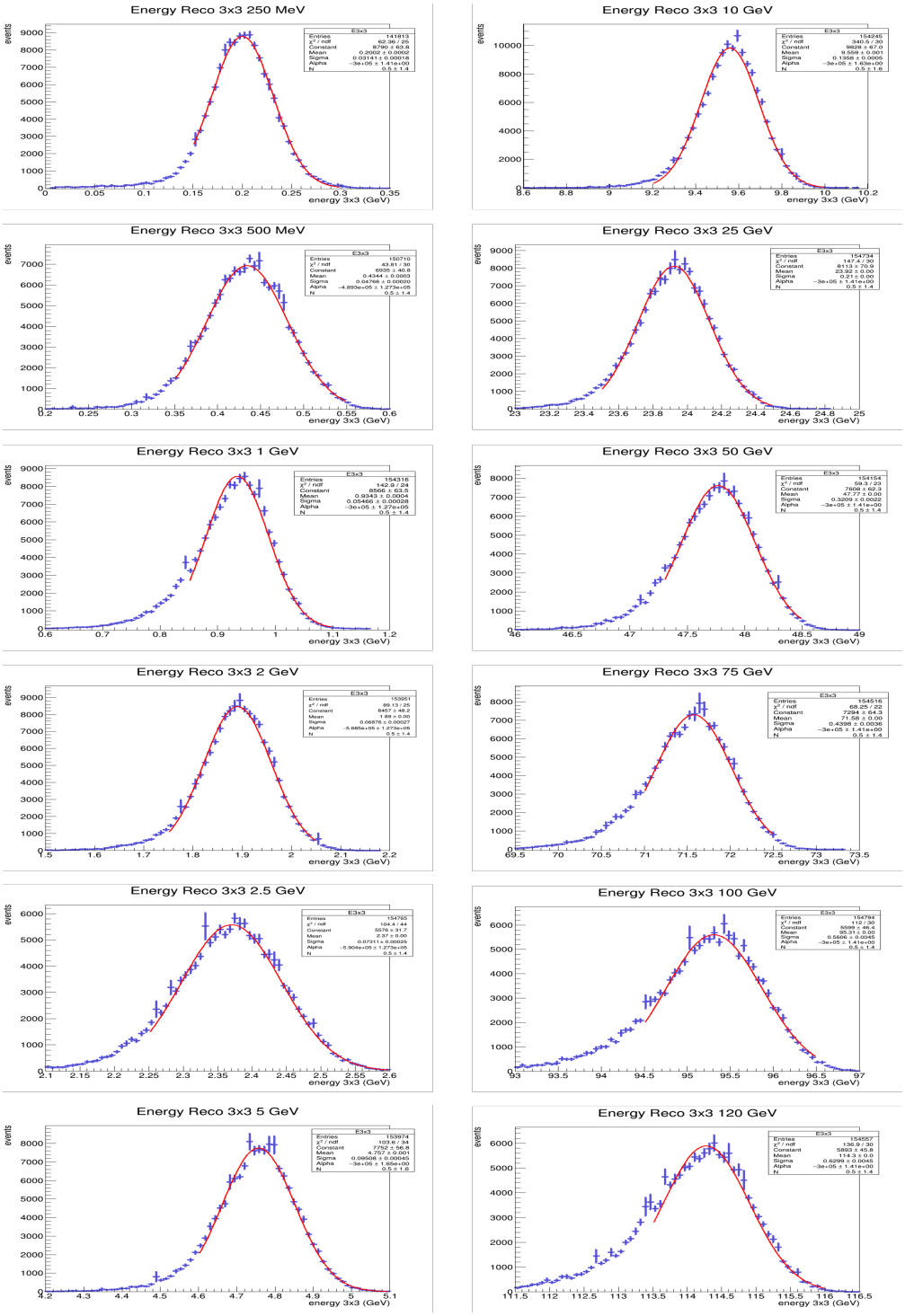

Figure 4.3: Energy reconstructed inside the 3×3 array of crystal for all the studied energies.

It should be noted that the electronic noise is not yet implemented in the Fast Sim. In a reaslistic situation a more complex approach should be implemented in the reconstruction of low-energy showers, which are contained ina smaller array and are much more affected by the effect of noise: at this stage of the analysis, however, a simpler approach, the same at all energies, has been preferred.

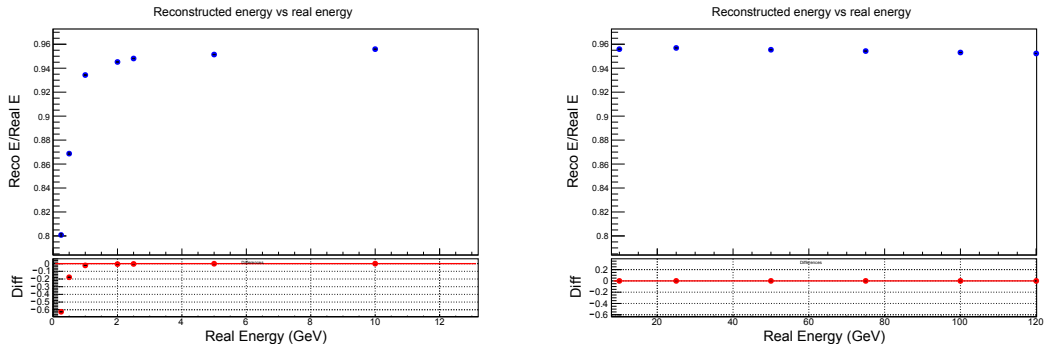

(a) (b)

Figure 4.4: Distribution of the mean fraction $E_{reco}(3 \times 3)/E_{true}$ in the energy range 0-12 GeV (a) and 8-120 GeV (b)

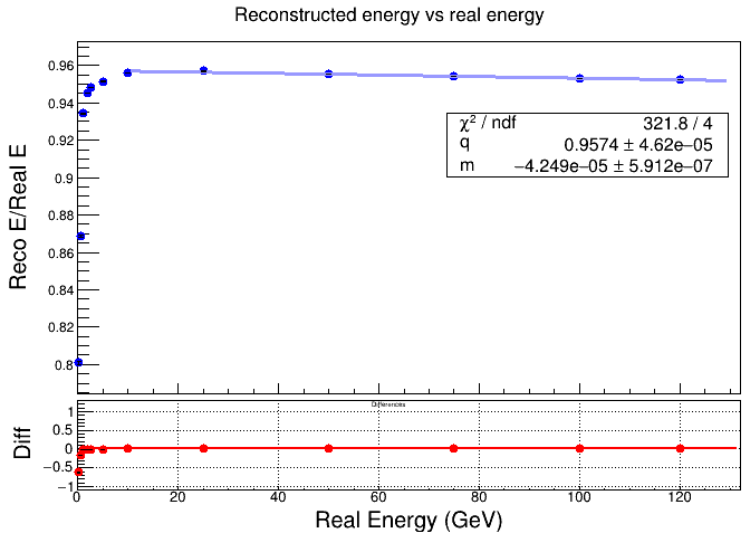

Figure 4.5: Distribution of the mean fraction $E_{reco}(3 \times 3)/E_{true}$ for the different set of studied energies.

From the peak values of $E_{reco}(3 \times 3)$ with respect to the E_{true} it is possible to evaluate the mean energy reconstructed inside the array of cells. The ratio $E_{reco}(3 \times 3)/E_{true}$ is reported in fig. 4.5. The plot shows that the algorithm is not stable for very low energies

meaning that, going towards lower energies, the energy reconstructed is decreasingly less than the true energy. While for $E_{true} > 10$ GeV the mean energy fraction is stabilized around a value

$$\frac{E_{reco}(3 \times 3)}{E_{true}} = 95,7\% \tag{4.5}$$

This value confirmed the precedent value found in [22]. In all the analysis done with the Fast Sim, the energy reconstructed in the calorimeter is always calculated as $E_{reco}(3 \times 3)$. Therefore, while analysing the data, the value of the energy from calorimetric information must be corrected accounting for the remaining 5% that is lost outside the array of crystals. From the RMS of the energy distribution in fig.4.3, that are fitted with a Crystal Ball function, it is possible to extrapolate the energy resolution of the calorimeter. As stated before, the energy resolution is composed by three terms. The second term is the "noise" term and it depends on the electronic noise of the readout chain. In the Fast Simulation the effect of the readout chain is not implemented. Therefore the noise term of the resolution is not simulated. For this reason, when fitting the ratio $\sigma(E)/E$ only the stochastic and the constant terms are inserted in the fitting function. The values for the a and c coefficients are shown in fig.4.6

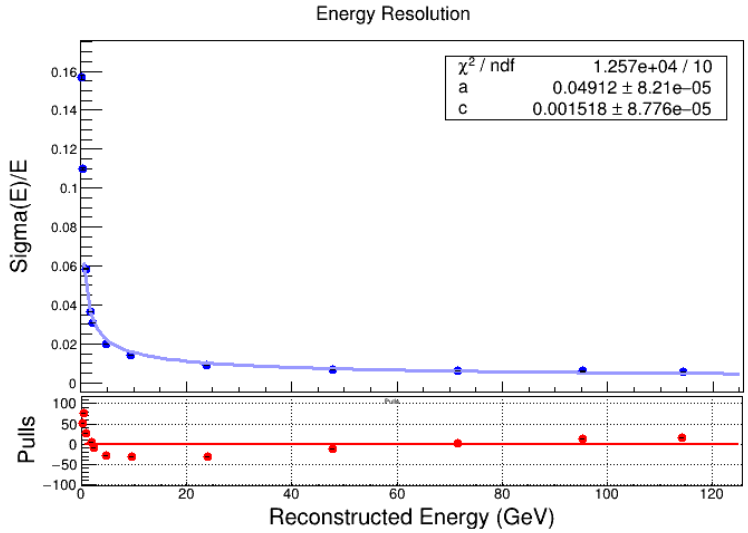

Figure 4.6: Calorimeter resolution as a function of E.

4.2 Particle Identification

The final computation of a_μ^{HLO} is based on the use of muon and electron angular distributions to perform the template fit, hence it is crucial to perform a precise particle

identification (PID) not to add any further systematic effect. Muons can be distinguished from electrons using solely the angular information [18], with the exception of a limited ambiguity region where $\theta_\mu \sim \theta_e$, which is determined by the the angular resolution of the tracking system. As stated before, the muon and electron scattering angles are connected by the elasticity condition defined by equation (2.20). The capacity of discriminate precisely between muons and electrons by means of the elasticity relation, depends on the angular information, and therefore is dominated by the angular resolution. This dependence is clearly visible in the fig.4.7 where different scenarios are depicted, with the angular resolutions varying from 0.02 mrad to 0.1 mrad. As expected, the width of the ambiguity region increases with degraded resolution.

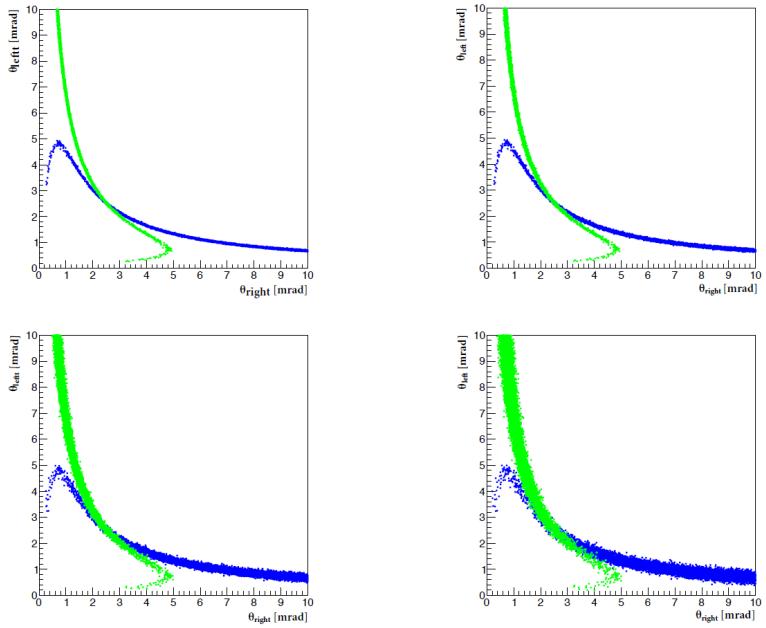

Figure 4.7: Distribution of the two measured scattering angles, qle f t versus qright in mrad, for events simulated with ideal angular resolution (only multiple scattering from the target included, top left panel), angular resolution of 0.02 mrad (top right panel), 0.06 mrad (bottom left panel) and 0.1 mrad (bottom right panel), respectively. In blue are the points corresponding to the correct particle identification, in green the wrong identification [18]

The addition of calorimetric information is useful to remove the ambiguity region. In fact, from the energy deposited in each crystal it is possible to extrapolate the position of impact on the calorimeter surface of the electron,identified by the shower centroid. In the definition from [34] the centroid coordinates are calculated by a weighted sum of the energies E_i released in the single crystals:

$$x = \frac{\sum_i w_i x_i}{\sum_i w_i}, \quad w_i = \max\left\{0, \left[W_0 + \ln\left(\frac{E_i}{E_T}\right)\right]\right\}, \tag{4.6}$$

The index i runs inside the 3×3 crystals of the considered array. E_T is the total energy released in the nine crystals and $W_0 = 4.0$ is an adimensional parameter. When $\theta_\mu \sim \theta_e$, the elasticity condition does not give information whether the particle detected is a muon or an electron because due to the angular resolution the particles are interchangeable. But even though the scattering angles are similar, the actual impact position on the calorimeter surface of the electron may be far from the impact position of the muon. In fact, the scattering angles are defined with respect to the direction of the incoming muon, that is close to the direction of the z-axis. The particles on the other hand, travels at least one meter after the scattering so the distance between the particles in the transverse plane increases. Combining the angular information with the centroid position of the shower, the electron can be distinguished from the muon. This method works only if the effective distance between the impact position of the muon and the position of the electron is large enough not to be ambiguous too.

In this section, a study on the inter-particle distance is presented. The distance d between the two impact points is defined as the distance between the shower centroid coordinates in the transverse plane, as defined before, and the (x,y) position of impact simulated muon extrapolated to the calorimeter surface.

$$d = \sqrt{(x_C - x_\mu)^2 + (y_C - y_\mu)^2} \tag{4.7}$$

The analysis discriminates between muons interacting in the first of the two stations, the furthest from the calorimeter, and muons that scatter in the second target. In fig.4.8, the distribution of the variable d is shown as a function of the following observables:

- mandelstam variable t;
- energy deposited inside the calorimeter $E_{reco}(3 \times 3)$, calibrated to the missing 5%;
- electron scattering angle θ_e;

Also two acceptance cut were applied on the analyzed events, to ensure that all the particles in the generate events reach the fiducial surface of the calorimeter, namely that all the electrons of the selected events impact on one of the nine core crystals of the calorimeter. The fiducial cut on the beam is imposed requiring that the impact point of the incoming muon from the center of the target is distant $r_\mu < 1.7cm$. In addition, in

order to increase the efficiency at large scattering angles, a threshold is applied to the reconstructed cluster energy to be $E_{reco}(3 \times 3) > 1$ GeV [22].

From these general distribution, the difference between the events from target 1 and the ones from target 2 is already visible. The distance of flight for the scattered particles from target one is almost twice the distance from the second target. Therefore, also the distance between the impact point on the calorimeter's surface is greater.

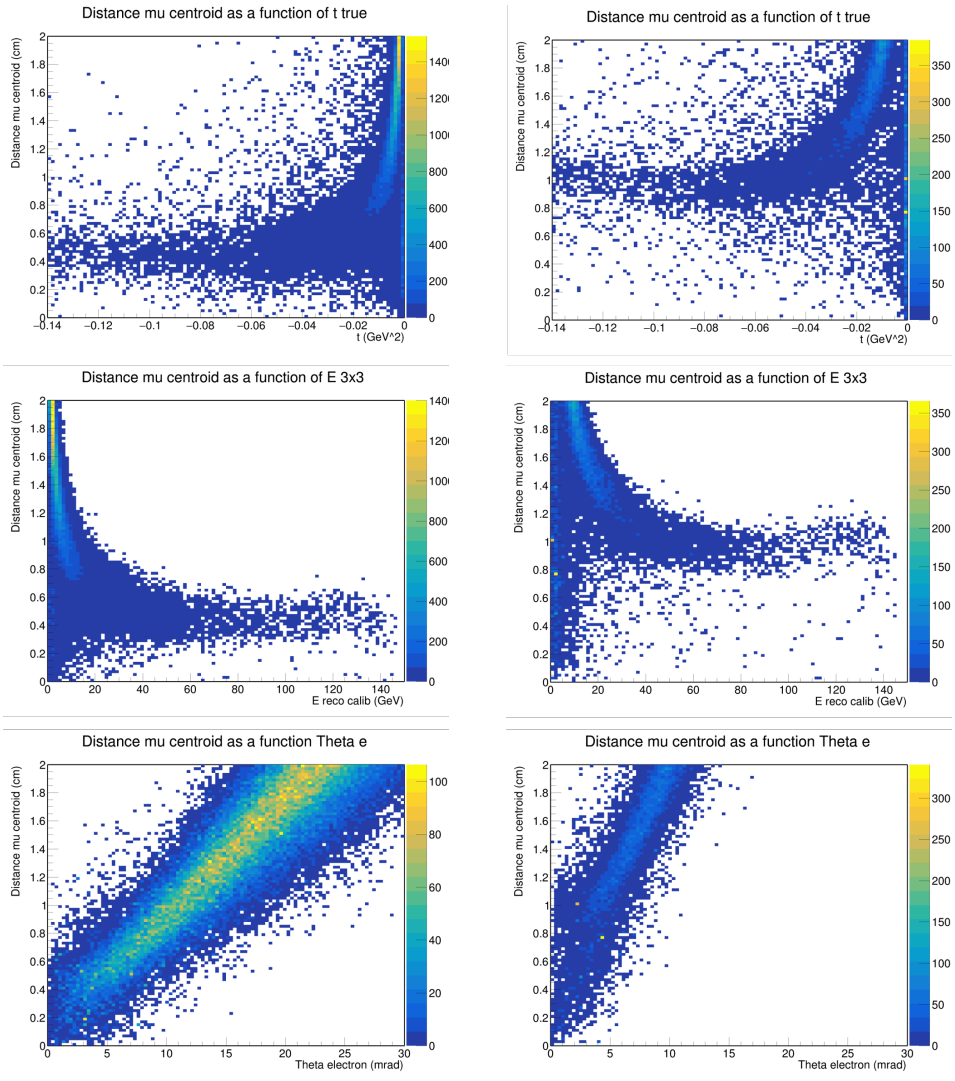

(a) (b)

Figure 4.8: Distribution of the variable d as a function of the mandelstam variable t, the energy of the electron E and the electron scattering angles, for muons interacting in target 2 (a) and muons interacting in target 1 (b).

The addition of the calorimetric information is crucial inside the ambiguity region, where $\theta_\mu \sim \theta_e$. The maximum foreseen angular resolution is about 0.06 mrad. The distribution of the distance d is plotted also as a function of the angular difference itself, in fig.4.9, after selecting only events where the difference $\Delta\theta = \theta_e - \theta_\mu < |3mrad|$. As expected, there are more events in the positive region of $\Delta\theta$ since for the kinematic of the process, the electron is scattered to greater angles than the muon. Moreover, in all the range of $\Delta\theta$ the distance d between the impact positions is stabilized around $d \sim 0.4$ cm for the events from target 2, and $d \sim 1$ cm for the events from the first target.

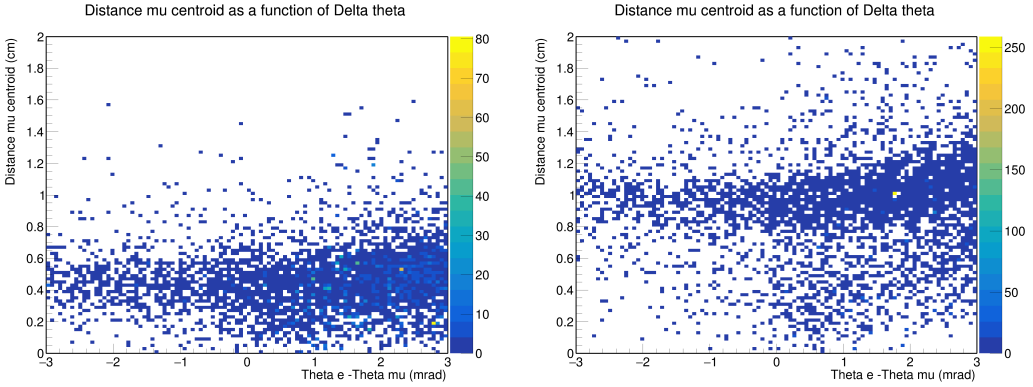

(a) (b)

Figure 4.9: Distribution of the variable d as a function of the difference $\Delta\theta = \theta_e - \theta_\mu$.

This is valid also for event where $\Delta\theta = \theta_e - \theta_\mu < |0.3\,mrad|$, so when the difference is smaller than the angular resolution. This is visible in the projections plotted in fig.4.10 (a-b), where even with low statistic the spatial distribution is clear. The two different peaks are visible also in the projection of events with an electron energy restricted to the range $70 < E_e < 80$ GeV, in fig. 4.11. This is an interesting range since at $E_e = 75$ GeV there is the peak of the integrand of equation (2.6). These plots corroborate the idea of using calorimetric information to distinguish between muons from electrons. In fact, the main distance between the impact points is of the order of half of centimeter, more than enough to guarantee the correct identification.

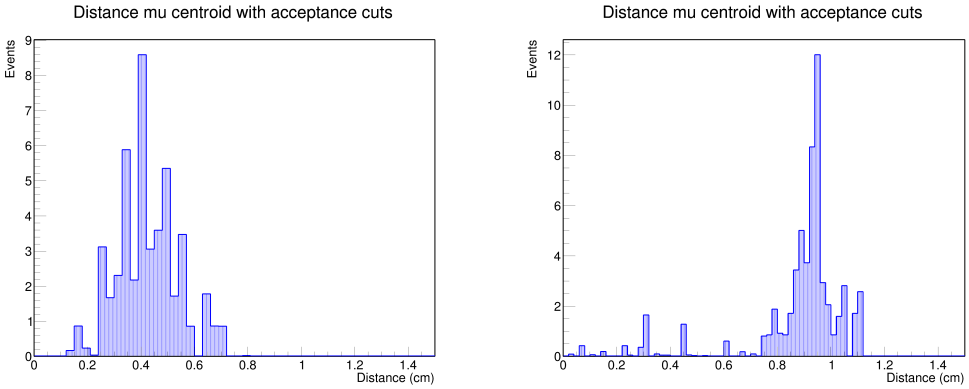

(a) (b)

Figure 4.10: Projection of the distance d for events from target 2 (a) and events from target 1 (b) with a value of $\Delta\theta = \theta_e - \theta_\mu < |0.3\,mrad|$.

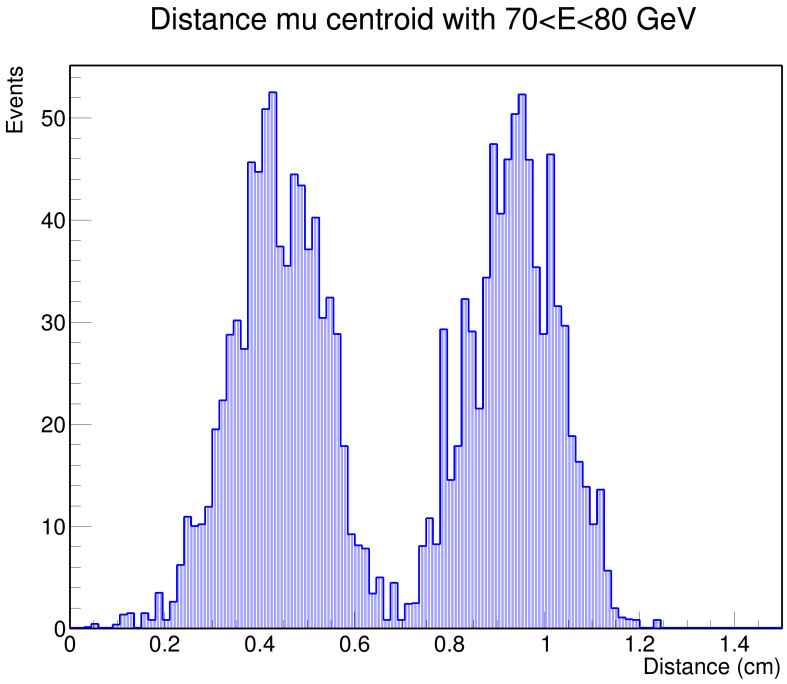

Figure 4.11: Projection of the distance d for events from both targets inside the electron energy range $70 < E_e < 80$ GeV.

4.3 Event Selection

The event reconstruction in the MUonE tracker exploits the two-body kinematics to allow the extraction of t from the emission angles of the two scattered leptons. The

emission of one or more photons in radiative events spoils the kinematic bounds, resulting in a biased determination of t (see also below). As shown below, the calorimeter allows the selection of genuine two-body events. An algorithm for the event selection based on calorimetric cuts is described in[22], and it has been tested up to NLO events generated by the Fast Simulation. In this thesis, the same algorithm has been tested for NNLO events.

This algorithm exploits the relation (2.19) between the electron energy E'e and its angle θ_e which is valid only for two-body diffusion in order to reject radiative events. The three cuts applied to the total generated sample are the following:

1. **Acceptance cuts**: same as the ones applied for the PID. They are needed to maintain the events inside the fiducial surface of the detector and to level the detector acceptance. They be summarized as follows

$$r_\mu < 1.7\,cm\,, \qquad E_{reco}(3\times 3) > 1\,GeV \tag{4.8}$$

2. **Cut on the energy fraction**: electrons from elastic events are expected to have an energy equal to $E_{el}^{th}(\theta_e)$ as described by eq.2.19. When compared with the effective energy reconstructed by the calorimeter, if the ratio between the two values differs from the mean reconstructed energy in the 3×3 crystal array the event is not an elastic event. The cut on the energy is the following:

$$\Delta_E(\theta_e) = \frac{E_{reco}(3\times 3)}{E_{el}^{th}(\theta_e)} - 0.957 < 4\sigma(E_{el}^{th}(\theta_e)) \tag{4.9}$$

   where $\sigma(E_{el}^{th}(\theta_e))$ is RMS of the energy resolution function [22].

3. **Cut on the shower centroid**: the shower centroid is calculated starting from the energy released in each crystal of the calorimeter. However, also photons release energy inside the calorimeter, meaning that the presence of one or more photons will shift the shower centroid away from the actual impact position of the electron. Therefore, applying a cut on the difference between the reconstructed track of the electron and the shower centroid removes radiative events. The applied cut is:

$$|\vec{R}| = |\vec{r}_C - \vec{r}_{track}| < 4RMS(E_{reco}(3\times 3)) \tag{4.10}$$

This selection is effective in rejecting radiative events, as shown in Fig.4.12 and 4.13, which compare the electron and muon scattering angles at NLO and NNLO before (blue

curve) and after (green) applying the cuts to the MC truth of events witouth radiation (black). The green curve well overlaps to the black one for theta¡25 mrad; In the plots in fig.4.12-4.13, the electrons and muons angles and energy are shown. The MC truths at LO have been compared with the full set of events before and after applying the cuts. Even starting from NNLO events, the distribution after the selection (the green curve) follows very well the original LO distribution, both for angles and for energies. This is a further proof that the effects of NNLO corrections on the final state observable are almost undetectable.

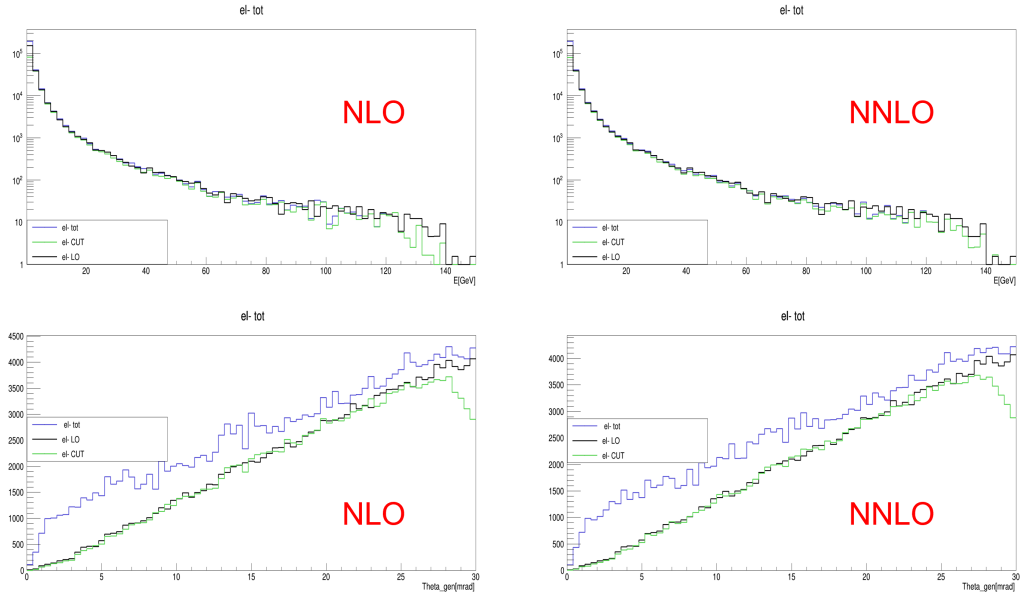

Figure 4.12: MC truth distributions of electrons energy (top) and scattering angle (bottom) before the calorimetric selection (in blue) for NLO and NNLO events. The effect of the selection is shown by the green histograms. The black histograms show the LO prediction.

Apart from recovering the original MC truth, selecting only elastic events allows also to recover the elasticity condition. The elasticity condition describes an characteristic curve in the (θ_μ, θ_e) plane as shown in fig.2.3. A similar curve is also defined by the condition on the energy in the (E_e, θ_e) plane. In the following plots, the correlations of (E_e, θ_e) and (θ_μ, θ_e) are shown, both for NLO event and for NNLO events. In the top lines all the generated events that are impinging on the second target are displayed and a conspicuous background is present. The second line represents the events after the acceptance cuts and the in third line only the events after applying all the final cuts are shown.

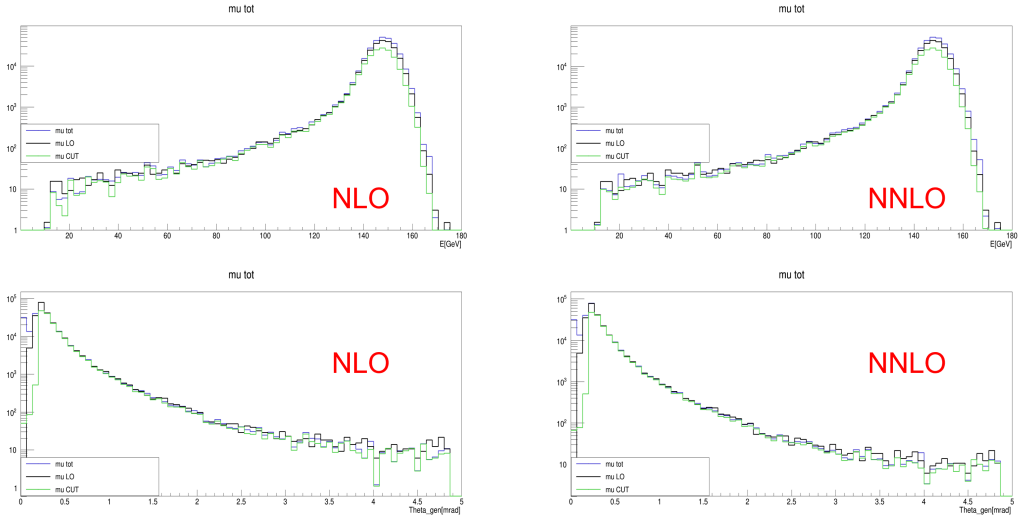

Figure 4.13: MC truth distributions of muons energy (top) and scattering angle (bottom) before the calorimetric selection (in blue) for NLO and NNLO events. The effect of the selection is shown by the green histograms. The black histograms show the LO prediction.

The low muon angle region is populated by low energy electrons, discarded by the cut on the energy $E_{reco}(3 \times 3) > 1\,GeV$. This events are strongly affected by experimental perturbations and are not interesting for the final analysis of MUonE. Some of these electrons are radiating soft photons, hence they have a lower angle than the predicted one. Another fraction of the background is given by electrons deviated by Multiple Coulomb Scattering and impacting with a lower angle than the initial one. Also in this case, the analysis performed with NNLO events confirms the previous results at NLO.

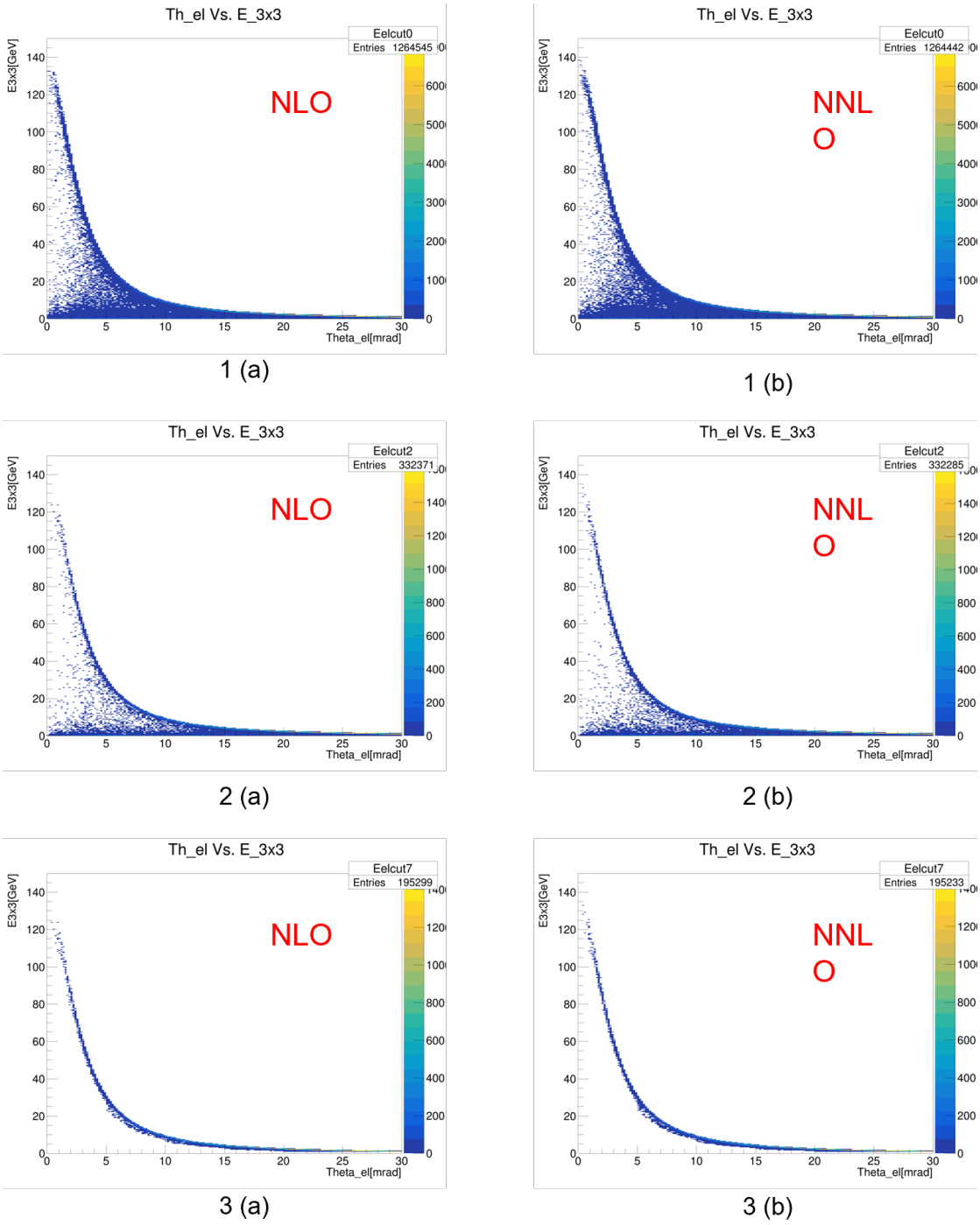

Figure 4.14: Correlation between the reconstructed calorimeter energy $E_{3\times3}$ and the electron scattering angle, before the selection (top line), after the acceptance cuts (second line) and avter the final selection (bottom line).

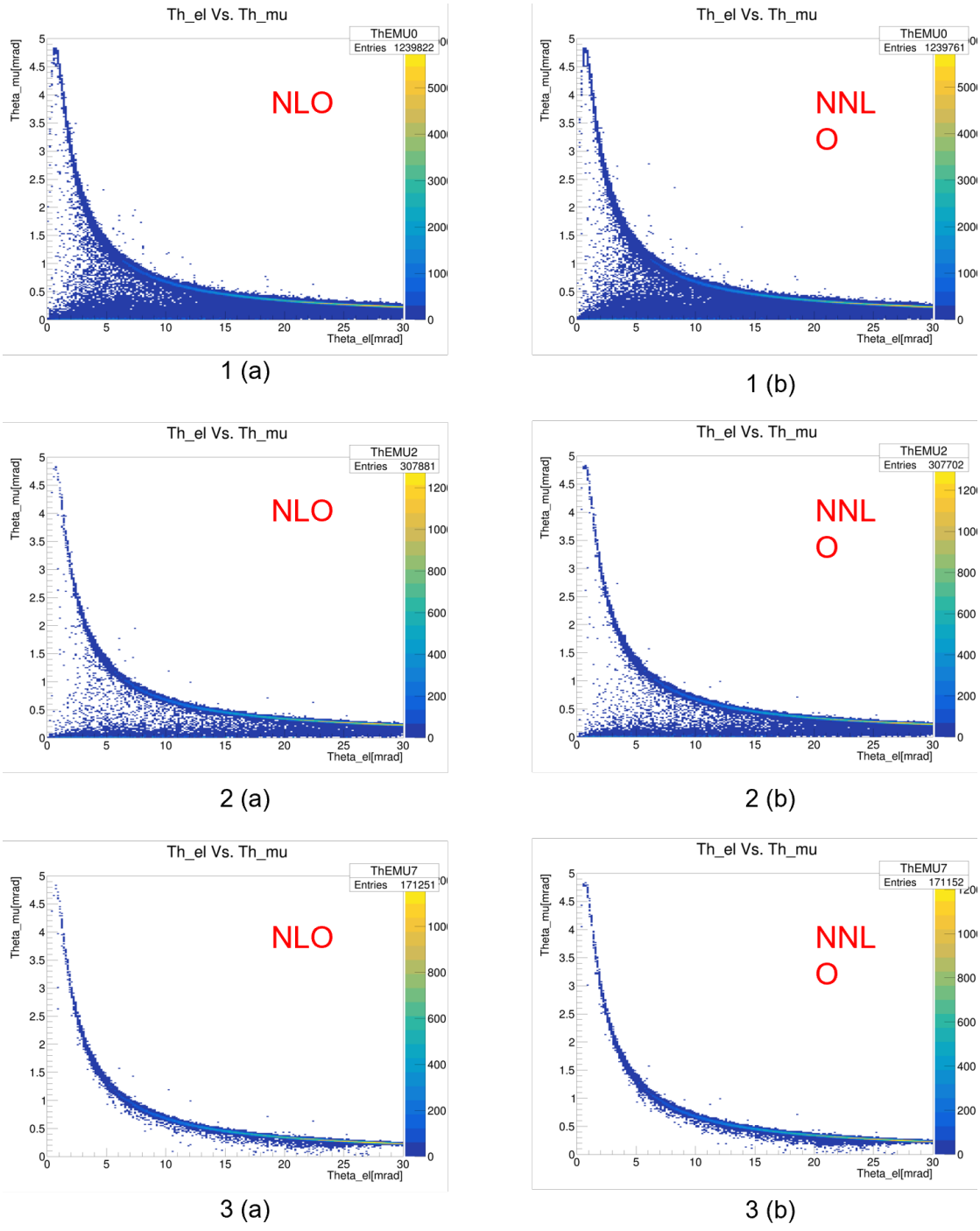

Figure 4.15: Correlation between the muon and electron scattering angles, before the selection (top line), after the acceptance cuts (second line) and after the final selection (bottom line).

4.4 Reconstruction of the momentum transfer t

The analysis technique carried on by the MUonE experiment is based on the extraction of the hadronic contribution thanks to a template fit method described in [20]. The parameterization used in the fit method for the hadronic contribution is depending on the Mandelstam variable t as shown in eq. 2.13. As of today, the template fit has been performed using the angular distributions of the electrons and muons scattering angles but in principle it could be performed also using directly the distribution of t. With this aim in mind, in this section various strategy to estimate the value of t event by event have been analyzed and compared to see which one presents the better resolution.

The differential unpolarized cross section of the studied process, at LO in QED, is reported in fig.4.16, and the dependence on the transfer momentum is described by the formula [23]:

$$\frac{d\sigma_0}{dt} = \frac{4\pi\alpha_0^2}{t^2\lambda(s, m_\mu^2, m_e^2)}\left[(s - m_\mu^2 - m_e^2)^2 + st + \frac{t^2}{2}\right] \tag{4.11}$$

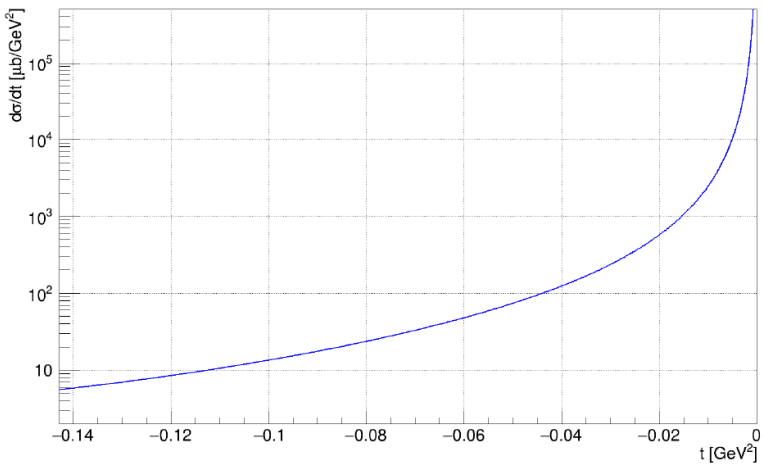

Figure 4.16: Differential cross section of the μe elastic scattering at LO, as a function of the momentum transfer t.

The variable t can be reconstructed using only calorimetric information since, as seen in section 2, in case of elastic events, it can be defined as:

$$t = 2m_e^2 - 2m_e E_e' \tag{4.12}$$

where the energy of the scattered electron $E_e^{'}$ is directly measured inside the calorimeter. At the same time, in case of elastic events, once the energy of the incoming muon beam is known, the energy of the outgoing electron can be calculated also starting from angular information using the following formulas:

$$\beta = \frac{\sqrt{1-(m_\mu/E_\mu)^2}}{1+m_e/E_\mu} \tag{4.13}$$

$$z = \beta cos(\theta_e) \tag{4.14}$$

$$E_e^{'} = \frac{1+z^2}{1-z^2} m_e \tag{4.15}$$

Therefore, a second method of extraction of the variable t is here also studied, using the angular information of the exit angle of the electron measured by the tracking system. In the following analysis, the distribution of the Mandelstam variable t measured with the calorimeter and with the tracking system have been studied and compared with the MC truth distributions. The formula used to compute the value of t from the lepton angles are correct only in case of elastic events, therefore in the analysis different scenarios have been simulated with and without applying the cuts for the elastic events selection. On the contrary, even in case of radiative events, the measurement of t with the calorimeter is expected to be correct since also the energy transferred to the photons is then absorbed by the crystals and therefore measured. In the analysis the energy reconstructed inside the calorimeter has been corrected for the 5% of the energy that is lost outside the 3×3 array of crystals.

In fig.4.17 and 4.18, the MC truth distributions for the variable t are shown, compared with the distributions obtained with the calorimeter and the tracking stations. As expected, in fig. 4.17 (a), where no cuts were applied, the calorimeter distribution follows well the MC truth while the tracking t is shifted towards the lowest values. In this sample of events also the radiative events are included. It should be noted that, even at this very early stage, the calorimetric measurements well reproduces the theoretical expectation, even without all the requirements which need to be applied when using the tracker information.

After applying the cuts for selecting the elastic events, also the distribution obtained with the tracking system well represents the MC truth, fig.4.18.

The resolution of the calorimetric measurement is then compared to that of the tracker

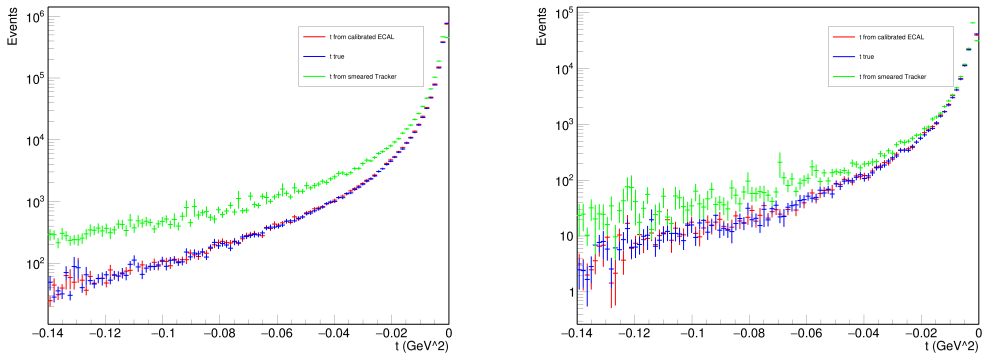

(a) (b)

Figure 4.17: Comparison between t MC truth distribution with t from calibrated ecal and from tracking system, without applying any cuts (a), and after the acceptance cuts.

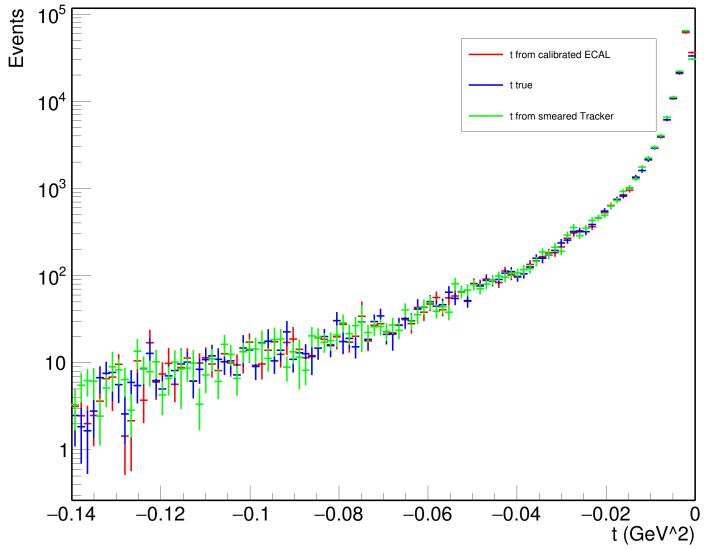

Figure 4.18: Comparison between t MC truth distribution with t from calibrated ecal and from tracking system after the final cuts.

at the three stages of the analysis. The plots (a) - (f) of fig.4.19 show the value of the difference $\Delta t = t_{meas} - t_{true}$, in case of t measured by the calorimeter (left column) or by the tracking system (right column), as a function of t_{true}, before any selection (top), after the acceptance requirements (center), after all the requirements (bottom). Already from these plots is visible that applying the cuts the difference in t reduces and it stabilize around zero. The differences between the calorimetric measure and the tracking one is visible from the projection of the resolution Δt, in different intervals of

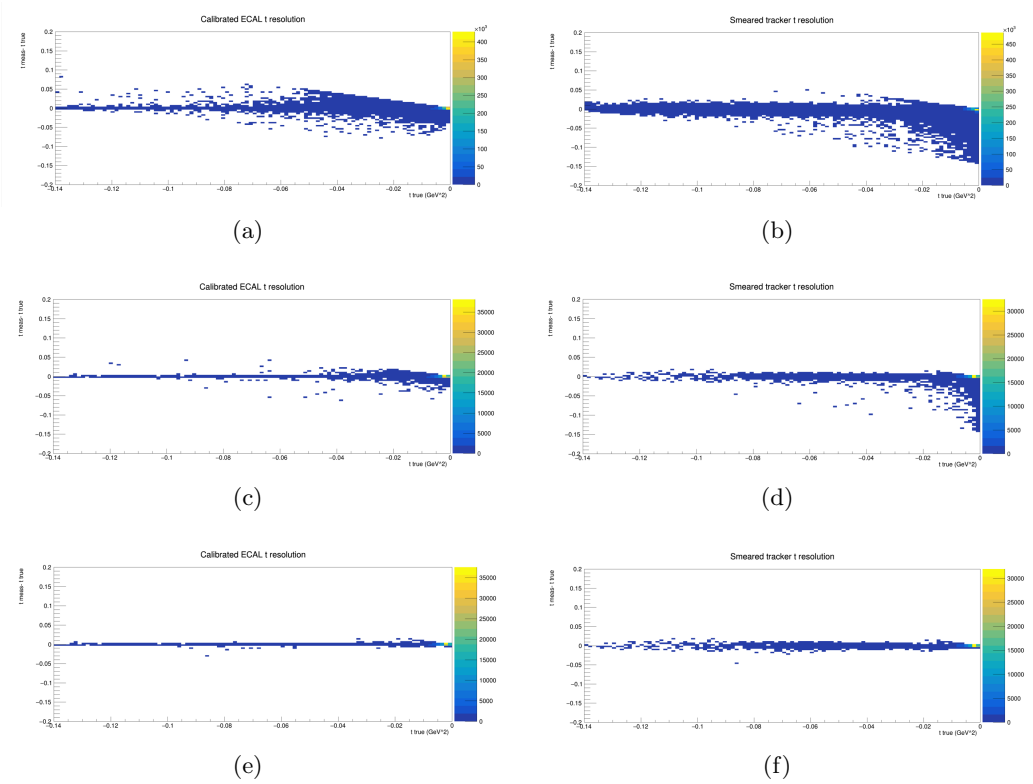

Figure 4.19: Distribution of the alue of the difference $\Delta t = t_{meas} - t_{true}$ as a function of the value of alue of the difference t_{true}.

the variable t_{true}. In all the three cases, with and without the cuts, the RMS of the calorimetric distribution is smaller than the one of the the tracking system.

This first result on the resolution suggest that further studies on the application of a calorimetric measurement for the final extraction of the hadronic contribution should be done. The next step could be perform the template fit with the distribution of t instead of the angular one and compare the fit parameters results.

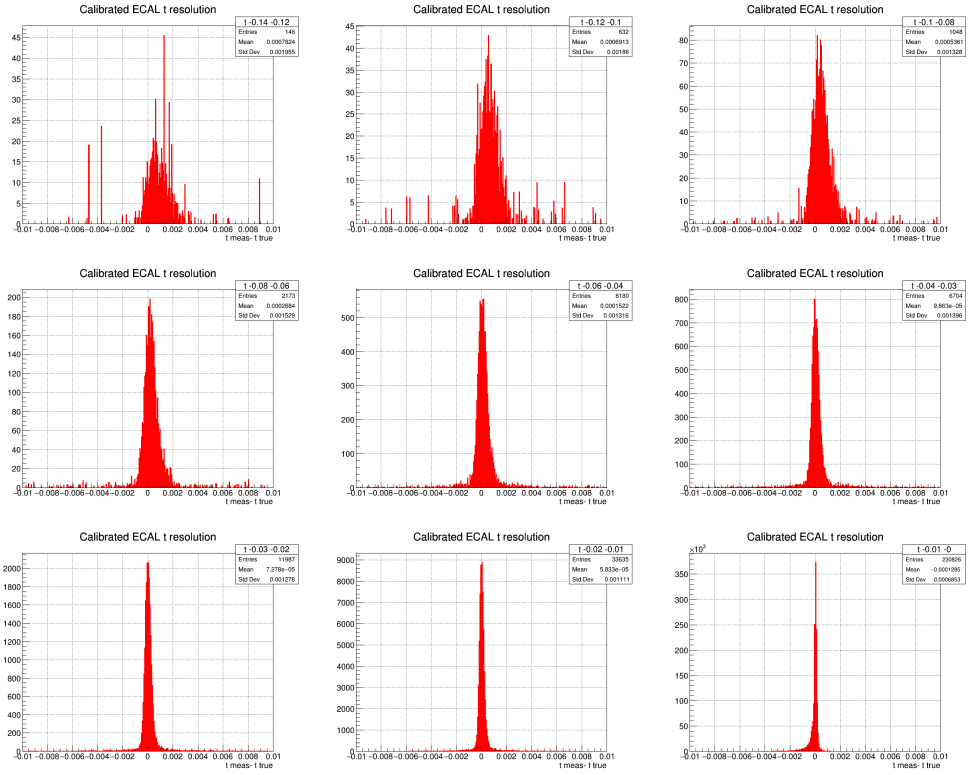

(a)

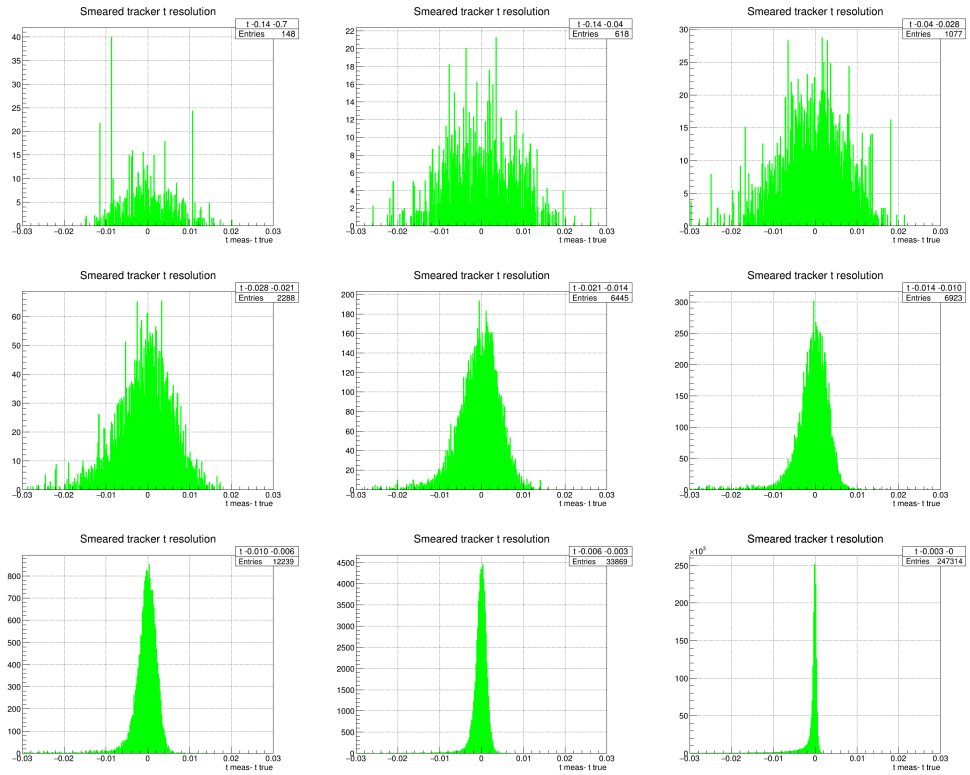

(b)

Figure 4.20: Distribution of the difference $t_{meas} - t_{true}$ for different intervals of t_{true} measured by the calorimeter (red) and with the tracking system (green).

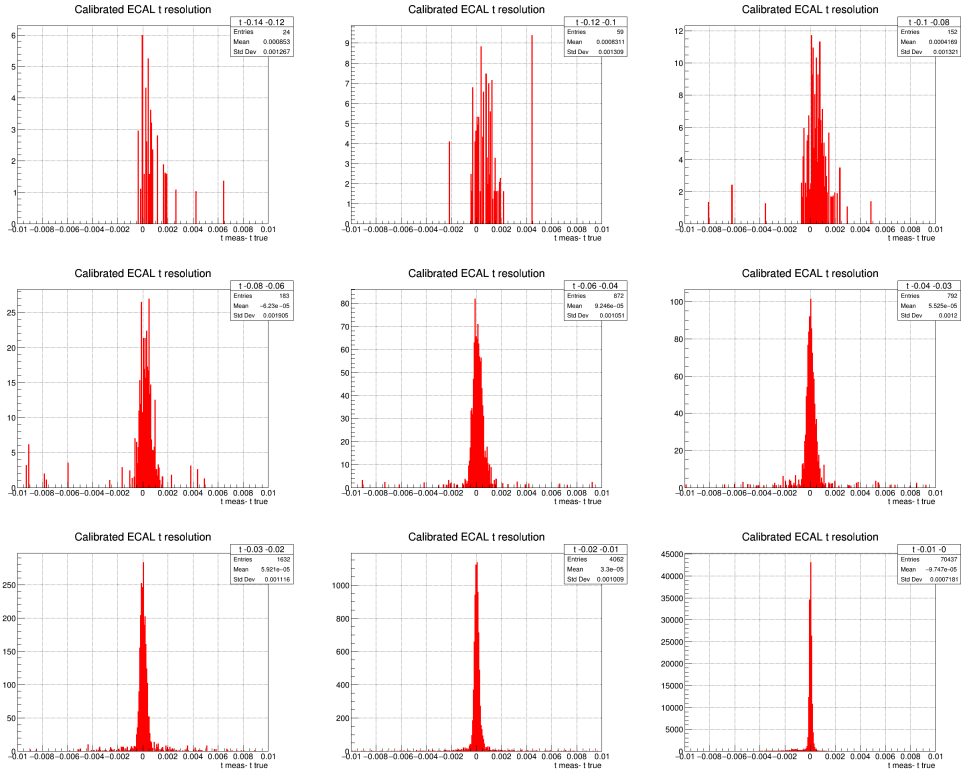

(a)

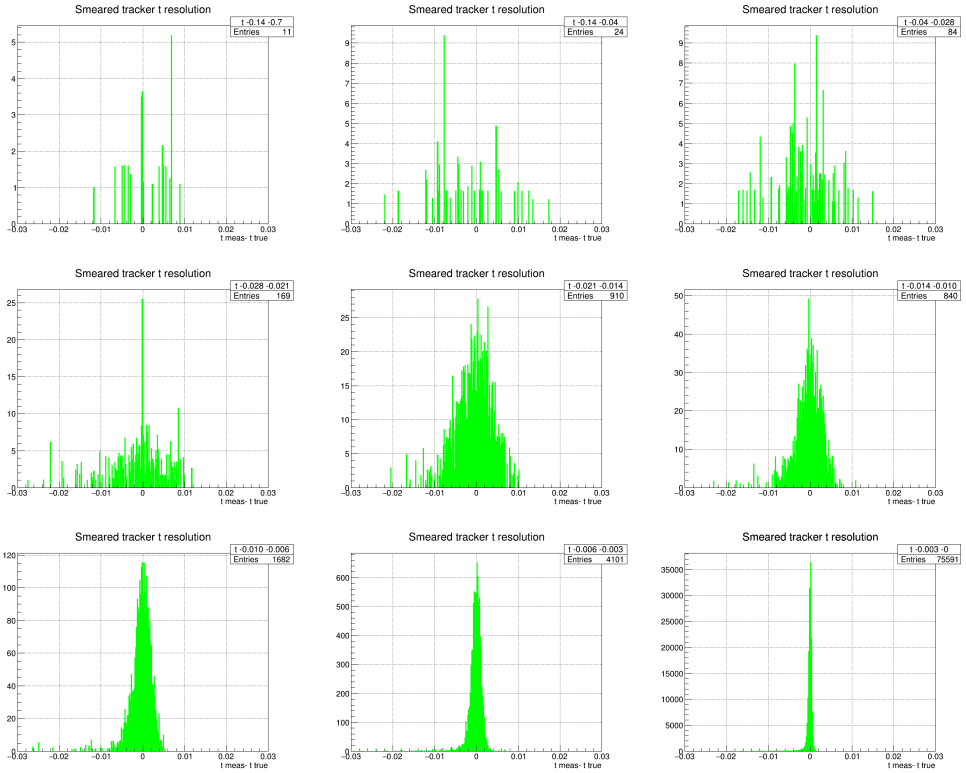

(b)

Figure 4.21: Distribution of the difference $t_{meas} - t_{true}$ for different intervals of t_{true} measured by the calorimeter (red) and with the tracking system (green), after the acceptance cuts.

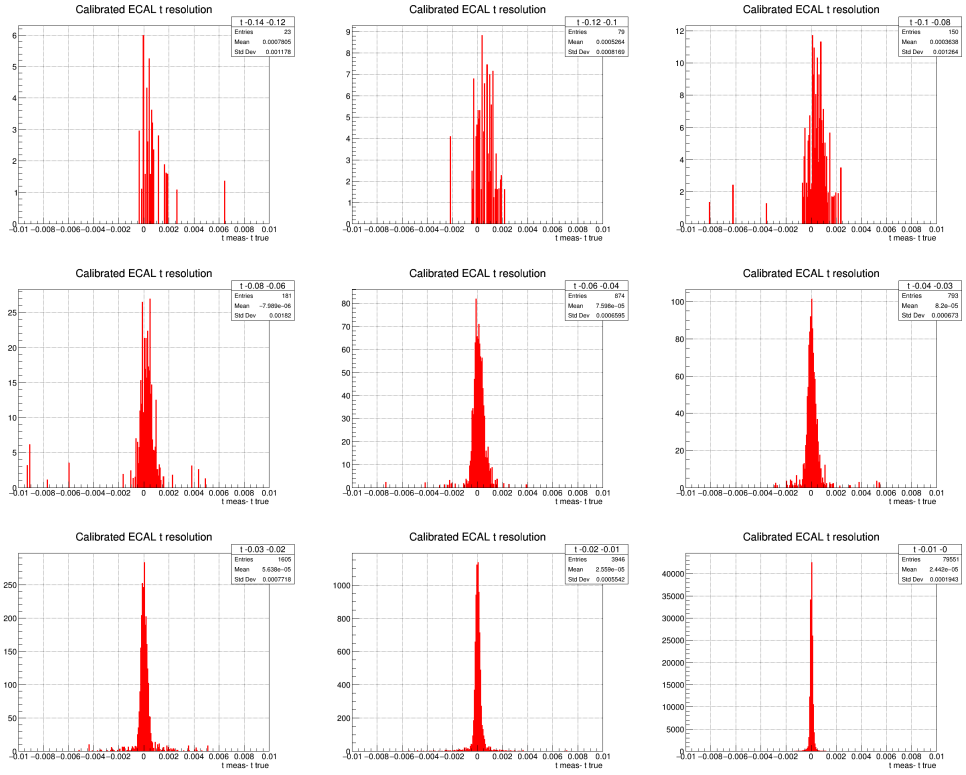

(a)

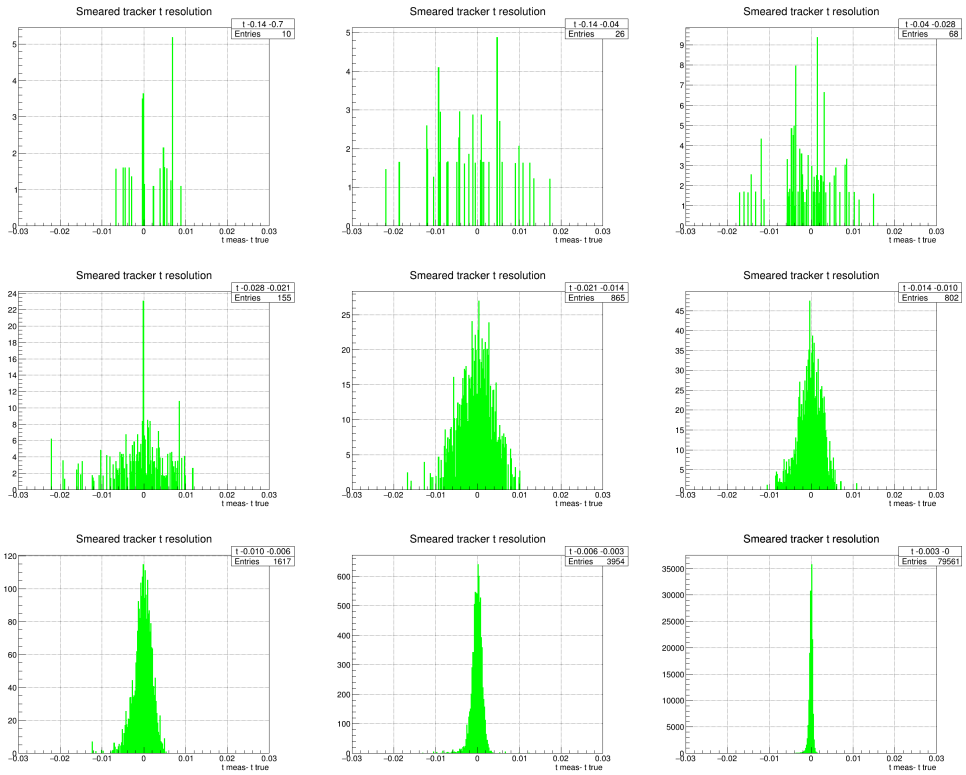

(b)

Figure 4.22: Distribution of the difference $t_{meas} - t_{true}$ for different intervals of t_{true} measured by the calorimeter (red) and with the tracking system (green), after the final cuts.

Chapter 5

Calorimeter test beam

In this final section, a preliminary analysis on the calorimeter Test Beam of July 2022 is presented. This was the first test of the small-size calorimeter (5×5 array of crystals) with a particle beam. The test was performed in the T09 beam line of SPS in the East Area of CERN. The T09 beam provides different kinds of particles hence it was possible to test the calorimeter with electrons and minimum ionizing particles (MIPS) as muons. The calorimeter was also tested with a laser system sent to the calorimeter through optical fibers. In the seven days of data taking, several sets of data were recorded, with different configurations of the apparatus. A preliminary analysis performed on a subset of data, collected in a stable configuration, is discussed in the following. For the future, a more detailed analysis of all the data is necessary.

5.1 ECAL test beam setup

The main goal of the Test Beam of July 2022 was to test for the first time the experimental setup, including the new data acquisition system (DAQ), and take runs of data, with beam of particles with tunable energy known with a $\pm 3\%$ precision, to perform a first calibration and study the overall performance of the calorimeter. The total experimental apparatus of the test included:

- Particle beam from the T09 beam line of SPS at CERN;
- A set of Cherenkov counters which allowed the selection of the desired particle species;

- A set of tracking chambers which could allow tracking each particle with a sub-mm precision (which was however not used);
- Homogeneous e.m. calorimeter composed by an array of 5×5 scintillating crystals of PbWO4 mounted in a carbon fiber alveolar box and read by APDs;
- Electronic read out system and a computer dedicated to the DAQ;
- Laser system connected via scintillating fibers;

A brief description of each single component of the apparatus is given in the following paragraphs. During the test beam few adjustments were made in terms of mechanics and electronics to perform real-time improvements. In the following section, along with the data, the most relevant changes of the technical configuration of the apparatus are described.

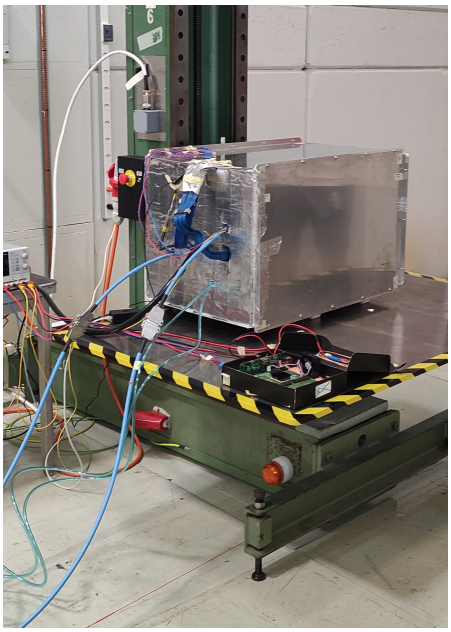

Figure 5.1: Final assembled calorimeter placed in the experimental area along the trajectory of the beam (red line on the floor).

T09 beam line

The T09 beamline is situated in the renovated East Area of CERN and started its operation in 2021. The final T09 beam originates from a 24 GeV/c proton beam of the PS accelerator that impinges on the North target and produces a variety of particles.

Among these available particles there are electrons, positrons, muons, pions, kaons and (anti)protons. The T09 beam line, used for the experiment is therefore a mixed hadron and electron beam and can transport either positively or negatively charged particles with momenta between 0.1 GeV and 16 GeV. The beam line has a multi-target configuration. By changing the material target it is possible to change the composition of the final beam. For the MUonE test beam, electrons and muons were exploited up to an energy of 10 GeV. The beam can also be used in a focused mode, with a beam size of 4 mm and 1-2 mrad of divergence, or in a parallel mode, with a beam size of 12 mm and a divergence of 0.2-0,5 mrad. The maximal rate of paarticles is 10^6 particles/spill but it drops to 10^4 particles/spill for energies lower than 1 GeV. The spill duration is of about 2.4 sec and there are typically 1-2 spills per minute. The beam was controlled from an interface placed in the control room.

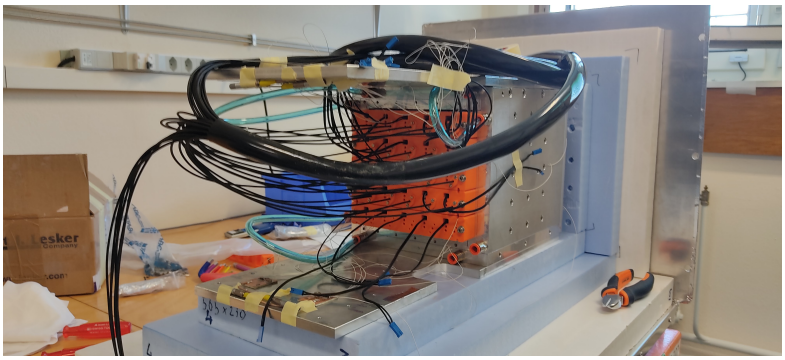

Figure 5.2: View of the inside of the calorimeter. The APDS and the optical fibers are inserted in the orange support and placed close to the calorimeter surface.

Calorimeter, mechanical support and APDs

The main structure of the calorimeter is composed by 25 scintillating crystals, inserted in a carbon fiber box and read by 25 HAMAMATSU APDs. The characteristics of the scintillating crystals are already been described in section 2. The temperature of the calorimeter was regulated by a fluid circuit inserted in a metal box. The temperature was also monitored thanks to sensors placed in contact with the internal surface of the calorimeter. Each crystal was read by a single APDs with an active area of mm, kept in position by a plastic container, as shown in fig. The APD is not in direct contact with the ECAL surface and no optical grease was applied. The calorimeter and the APDs had already been tested in the lab at Legnaro with test pulses.

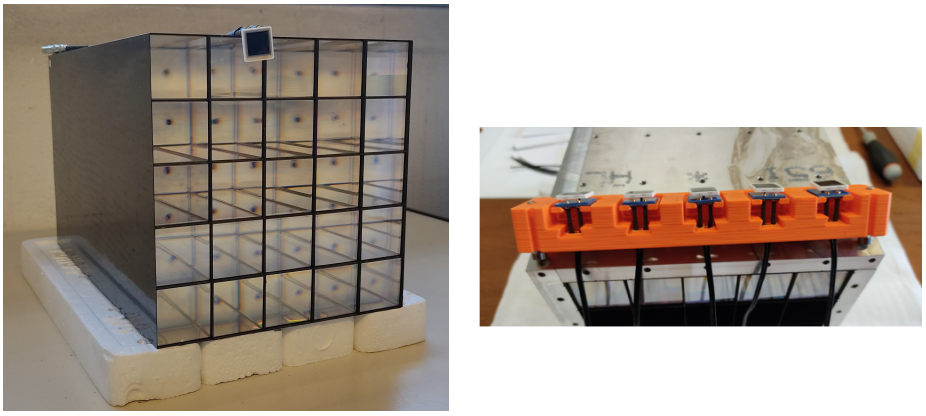

(a) (b)

Figure 5.3: Scintillating crystals inserted in the carbon fiber structure along with one APD (a). Support structure with APDs (b).

Read out chain

The readout chain of the Test Beam is composed by two Front End Board (FEB), shown in fig 5.4, each board can read at maximum 16 channels, 32 in total, so the 25 channels of the calorimeter were divided into two groups. A schematic view of the geometrical order of the crystals an of the FEB order, namely the corresponding channel inside the board, is shown in fig.5.7. Then the two boards were connected to the FC7 fw board, developed by Imperial College and modified by the Collegues in Bologna. Different versions of the firmware were tested during the data taking to try and improve the data acquisition in real time.

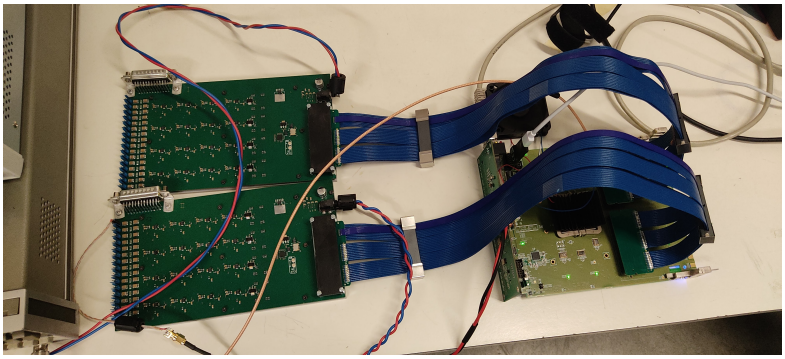

Figure 5.4: View of the two front end boards (on the left) cable connected to the FC7 board (on the right).

Laser system

The used laser was the NPL45C laser with an output of 2.9 mW at 50 kHz and an energy of 58 nJ/pulse. The Laser was sent to the crystals through scintillating fibers, one for each crystals, inserted in the same support of the APDs but in a different hole (fig.). The laser pulses were collected in the same run of the beam signals, in the period of time between two spills.

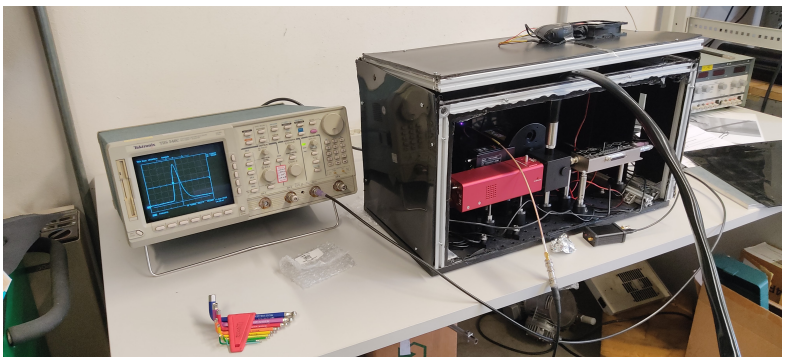

Figure 5.5: Internal view of the laser system (black box) connected to an oscilloscope for preliminary testing.

5.2 Data samples and setup configuration

Not all the data from the test beam have been analysed in this thesis. The selected runs come from the last days of data taking where the experimental setup and firmware was stabilized. In particular, changes were made on the firmware for the DAQ, on the values of the High Voltages of the APDs and on the temperature of the whole system. The firmware was changed to be more efficient in the event collection, so as to record more events for each beam spill. The High Voltages of the APDs were increased to increase the gain since the visible signal was very small and the temperature was modified thanks to the cooling system but then the program fro the monitoring of the temperature broke so, for each run, only the nominal temperature is here indicated.

Fig. 5.6 shows two examples of the event display that was visible almost real-time in the control room. All the signals from the 25 crystals are shown, ordered geometrically from 1 (upper left) to 25 (bottom right). The left graph is showing an example of beam event where the electron shower was shared by at least four crystals and the four different peaks are visible on the upper right portion of the figure. The right graph instead is

showing a typical laser event where the laser pulse is injected in all the 25 crystals simultaneously. The beam events and the laser events were collected in the same run because the laser was sent to the calorimeter in the period of time during two spills of the beam. However, many more beam signals were collected in one spill than the ones collected when the laser was on so the number of beam events in one run is much higher than the number of lasers.

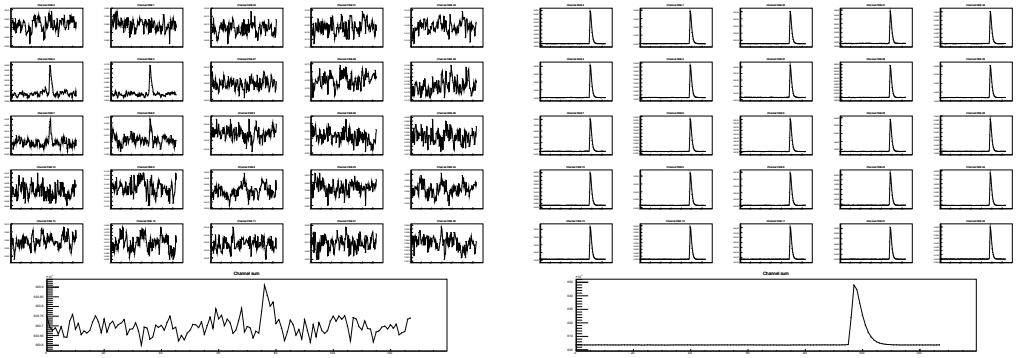

(a) (b)

Figure 5.6: Graphic view of a beam event (a) and laser event (b) as seen in the control room. The large plots on the bottom show the sum of the signals collected in the 25 counters.

1 2	**2** 1	**3** 30	**4** 31	**5** 32
6 4	**7** 3	**8** 27	**9** 28	**10** 29
11 7	**12** 6	**13** 5	**14** 25	**15** 26
16 10	**17** 9	**18** 8	**19** 23	**20** 24
21 13	**22** 12	**23** 11	**24** 21	**25** 22

Figure 5.7: Scheme of the calorimeter crystals order. on the top line is written the number corresponding to the geometrical order and on the bottom line the corresponding feb channel.

When analysing the data, the geometrical order of the crystals helps having a clear view of the structure of the calorimeter, but the order of the channels inside the FEBs is more important. In fact this is the order used inside the firmware to acquire the data and it helps revealing systematic effects due to the electronics readout. Fig.5.7 shows a front view of the calorimeter where also the number of the feb channel corresponding to each crystal is indicated. The different colors correspond to the two different boards. Inside the boards the channels were amplified in group of fours.

The next table summarises the APDs configuration, namely the correspondence between crystal, feb channel and bias voltages. The voltage $V_{b,0}$ corresponds to the nominal one given by HAMAMATSU that was used in the first part of the test beam. However, with this voltages the gain was very little, probably also due to other factors reducing the light collection. Therefore after few days the voltages were increased to a value $V_{b,1}$ equal for all the APDs, in order to have a bigger signal.

APD	FEB	Crystal	$V_{b,0}$ (V)	$V_{b,1}$ (V)	APD	FEB	Crystal	$V_{b,0}$ (V)	$V_{b,1}$ (V)
AA5654	1	4	381.2	405	AA5658	21	22	383.6	405
AA5647	2	5	377.7	405	AA5661	22	21	383.2	405
AA5668	3	9	384.6	405	AA5663	23	17	383.6	405
AA5665	4	10	381.6	405	AA5664	24	16	373.5	405
AA5666	5	13	380.6	405	AA5653	25	12	382.4	405
AA5651	6	14	382.0	405	AA5655	26	11	382.2	405
AA5648	7	15	379.9	405	AA5667	27	8	381.4	405
AA5657	8	18	381.6	405	AA5650	28	7	380.6	405
AA5662	9	19	382.4	405	AA5670	29	6	379.7	405
AA5652	10	20	383.8	405	AA5649	30	3	380.6	405
AA5659	11	23	381.8	405	AA5669	31	2	383.2	405
AA5660	12	24	380.8	405	AA5656	32	1	381.8	405
AA5646	13	25	380.0	405					

Table 5.1: APDs bias voltages and channel numbers.

The analysed runs of data are reported in table 5.1 together with the information on the energy and temperature selected. The used beam configuration was parallel mode so the beam spot was about 12 mm and the APDs voltages were already switched to

the higher value. The analysis focuses on the calculation of the electronic noise present in every single channel and shared by many channels. The goal is to investigate the presence of coherent noise, that was already noticed during the Test Beam, and if found, try to understand the possible source.

N°	Energy (GeV)	Temperature (C°)	V_b	Collection day	Beam mode
1	4	20	405 V	25/07	Parallel
2	5	20	405 V	26/07	Parallel
3	6	20	405 V	25/07	Parallel

Table 5.2: Analysed data set with run configurations.

5.3 Noise analysis

As stated in section 4, the second contribution to the energy resolution of the calorimeter comes from the electronic noise of the readout chain and depends on the features of the readout circuit. The noise contribution to the energy resolution increases with decreasing energy of the incident particles, therefore is important to reduce it as much as possible. Speaking of one single readout channel, the equivalent noise C_1 is given by the sum of two terms:

- an intrinsic contribution to the single channel, $C_{1,in}$;
- a coherent term, shared with the other channels, $C_{1,c}$;

By definition these two terms are independent, hence they sum quadratically as:

$$C_1^2 = {C_{1,in}}^2 + {C_{1,c}}^2 \tag{5.1}$$

In the test beam events, the signal from the incident particles was shared between different crystals, as shown in fig. 5.6 (a). In this scenario, the coherent component of the noise has a high impact on the measurement since increases linearly with the number of the involved channels. In fact, the noise of a signal spread to N different channels, C_N, has the same behaviour of the single channel noise, and can be defined as:

$$C_N^2 = {C_{N,in}}^2 + {C_{N,c}}^2 \tag{5.2}$$

The intrinsic part is defined as the quadratic sum of the intrinsic noise of the single channels, that are independent from each others. On the contrary, the coherent terms are correlated and they sum linearly.

$$C_{N,in}^2 = \sum_{i=1}^{n} {C_{i,in}}^2 = N{C_{i,in}}^2 \tag{5.3}$$

$$C_{N,c} = \sum_{i=1}^{n} C_{i,c} = NC_{i,c} \tag{5.4}$$

Finally, the total noise on N channels can be written as:

$$C_N = C_{1,in}\sqrt{N}\left[1 + N\left(\frac{C_{1,c}}{C_{1,in}}\right)^2\right]^{1/2} \tag{5.5}$$

As said before, the coherent noise has a strong impact on measurements that involve several channels simultaneously because it increases linearly with N. To understand the effective contribution of the coherent noise it is possible to calculate the parameter k

$$k = \left(\frac{C_{1,c}}{C_{1,in}}\right)^2 \tag{5.6}$$

that represents the fraction between the coherent part over the intrinsic one, in a single channel i. The parameter k can be calculated from the measurement of the ratio R_N

$$R_N = \frac{C_N}{\sqrt{N}C_1} = \left[1 + kN\frac{1}{(1+k)}\right]^{1/2} \tag{5.7}$$

If case of k=0, no coherent noise, the expected value for the ratio R_N is the unity. The ratio increase with the increase of the coherent term. In this analysis, the noise of the single channels was firstly evaluated. Then the contribute of the coherent noise was extrapolated for the two Front End Boards (FEB), in which the 25 readout channels were grouped.

5.3.1 Single channel noise

All the plots in this section come from the study of the 4 GeV data sample. The results obtained for the other energies are reported at the end. In the calculation of the single channel noise an event-by-event approach was used. The noise was extrapolated from a fit in the part of the recorded waveform where no signal was present. The beam events

were analysed separately from the laser events, but the same process has been followed for both. Starting from a typical event, as the one shown in fig. 5.6, for each channel the first 60 bins of the waveform were selected (fig. 5.8) and inserted in a histogram that was then interpolated with a Gaussian function to compute the mean and the RMS (fig. 5.9). The mean of this distribution represents the mean value of the baseline while the RMS represents the fluctuations, namely the noise, both expressed in ADC counts.

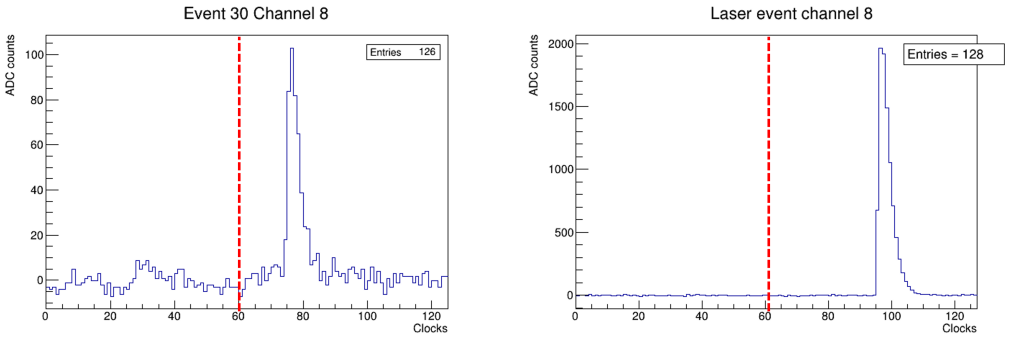

(a) (b)

Figure 5.8: Single channel waveform of a beam event (a) and of a laser event (b).

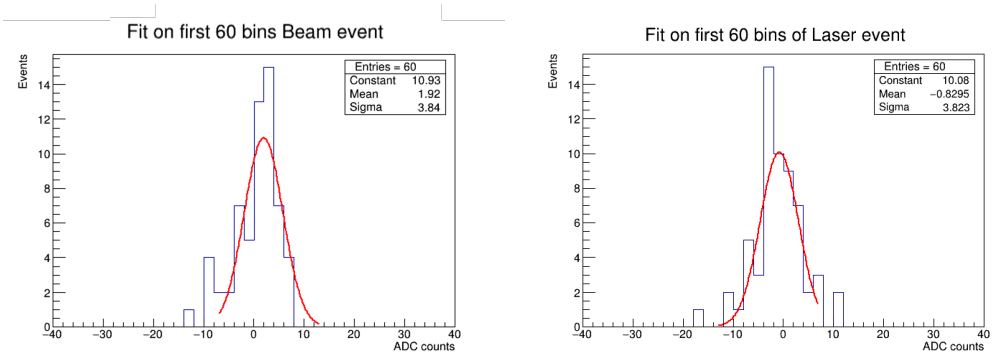

(a) (b)

Figure 5.9: Fit on the first 60 bins of one single channel for a beam event (a) and for a laser event (b).

The fit was performed event-by-event, extracting each time the mean value and the RMS per each channel. These values were then collected in final histograms, one with the means one and one for the RMS, both for signal events and laser events. The final histograms for one single channel are shown in fig. 5.10. The mean values of all the events of the baseline and of the RMS, for each channel, are shown in fig.5.11.

The right plot in fig. 5.11 shows that the value of the baseline is quite stable along the

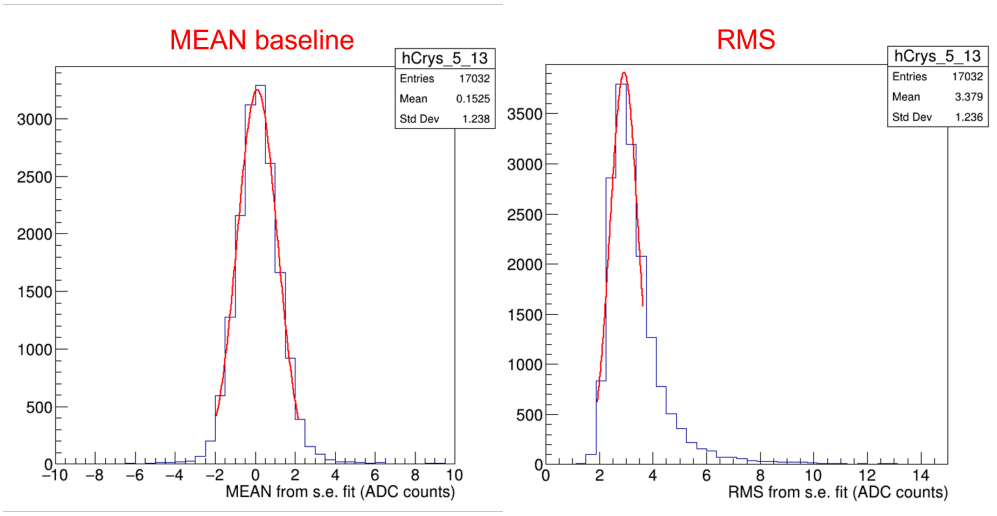

(a)

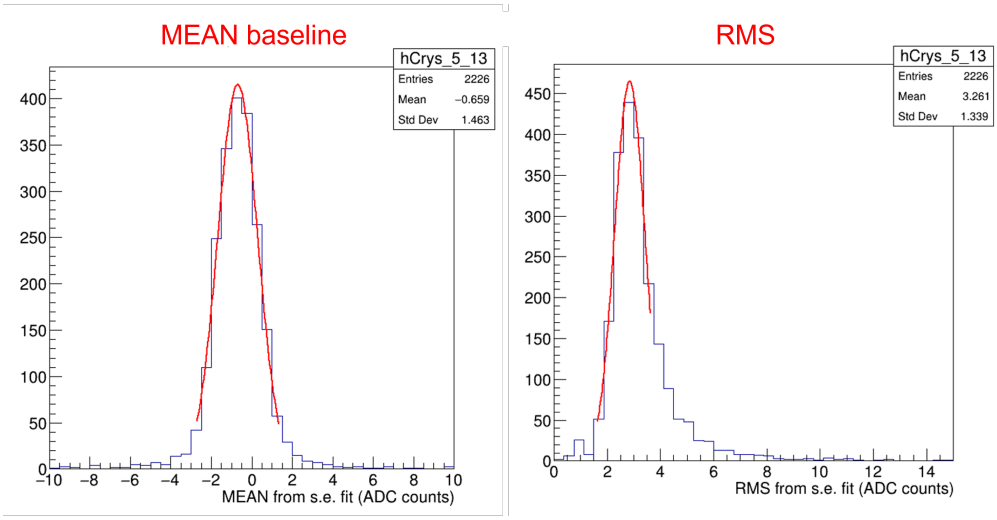

(b)

Figure 5.10: Fit on final parameter distributions (mean,RMS) obtained via the event-by-event analysis.

channels but is lower for the laser events than for the beam events. The mean value of the 25 channel is reported in table 5.3. In the analysis the mean was calculated after subtracting the waveform pedestal, that was calculated event by event. This step shouldn't create a systematic difference between laser and beam events but this phenomenon should be further investigated. On the contrary, looking at the various RMS, the value is not constant along all the channels. The geometrical order in this case is misleading. In fact, the right graph in figure 5.11, is showing a peculiar trend, almost

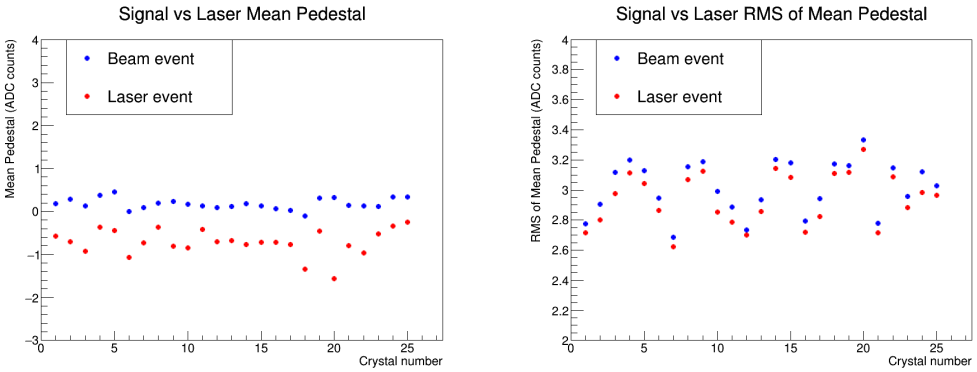

(a) (b)

Figure 5.11: Final values of the baseline and RMS for the different channels, geometrically ordered.

sinusoidal not easily understandable. Instead, in fig. 5.12, the crystals are ordered by the feb number and divided in the two front end board. Here it is clear how all the crystals of the second front end board (on the right) have a higher noise. The mean values for the two boards are reported in table 5.3. The mean RMS value for all the 25 channels is 3 ADC counts. From a rough calibration this value can be converted to 40 MeV of noise per channel. This results is not bad for a first terst of the calorimeter but it can be improved and it is important to understand how much of it is not intrinsic but comes from an external source that could be removed.

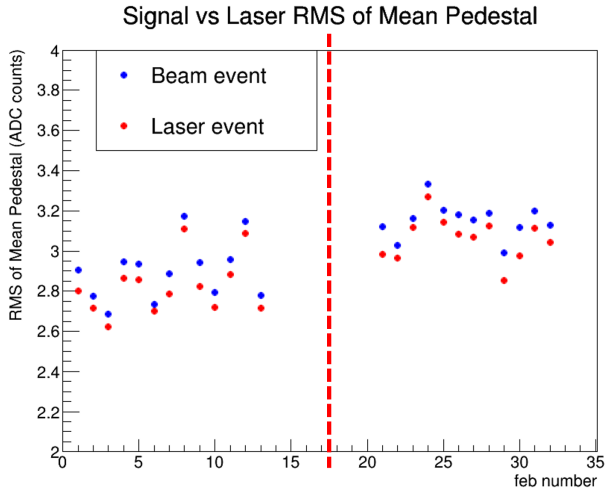

Figure 5.12: Final values of the RMS for the different channels, ordered by feb number and fivided in the two boards.

The results of analysis on the other two data samples are consistent with the results

from the 4 GeV set of events. All the results are reported in table 5.3. No effect related to the collected energy is observed.

		MEAN (ADC)	RMS (ADC)	RMS FEB 1 (ADC)	RMS FEB 2 (ADC)
4 GeV	beam	0.18	3.02	2.90	3.14
	laser	-0.71	2.94	2.82	3.06
5 GeV	beam	0.17	3.01	2.95	3.13
	laser	-0.69	2.94	2.85	3.06
6 GeV	beam	0.16	3.01	2.89	3.13
	laser	-0.69	2.93	2.83	3.03

Table 5.3: Final values of the mean baseline and RMS for the different data sets averaged on all the channels and on the channels from on single board.

5.3.2 Coherent noise

The coherent noise spreads to different channels that can somehow "talk" to each other. In this case, since the 25 channels are read by two different boards, the coherent noise might affect differently the channels from the FEB 1 than the others from FEB 2. Therefore the two boards were studied separately. The same approach event-by-event was used also for the study of the coherent noise, but instead of taking the firs 60 bins of one single channel, all the channels of one board were summed, obtaining the final waveform shown in fig. 5.13 (a). Two histograms were then filled with the 60 summed bins from the two boards. These histograms are visible in fig. 5.14. Also in this case from the histograms the mean value of the baseline and the RMS were extrapolated through a Gaussian fit. After performing the fit for each event, the fit parameter values were inserted into final histograms: one histogram containing the mean and one containing the RMS for each FEB, both for laser and for signal events. In case of both mean and RMS, the distributions of the second front end board (left column of fig. 5.18 and 5.19) are wider than the ones of the first board. The values of the mean baseline and of the final RMS for the two boards are reported graphically in fig.5.15. As expected from the results of the single channel analysis, the baseline of the sum of the channels for the laser events is lower than the one from the beam events. Regarding the RMS, the total noise of the second board is much higher than the one of the first board, even though the second board has 12 channels while the first one has 13 channels.

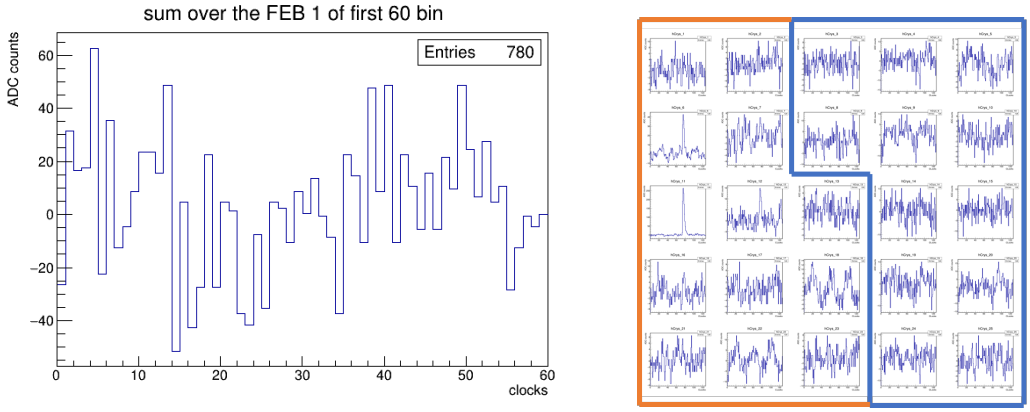

(a) (b)

Figure 5.13: Graphic view of the sum of the first 60 bin of one board (a) and the example of a beam event (b) where the coloured borders indicates the two boards.

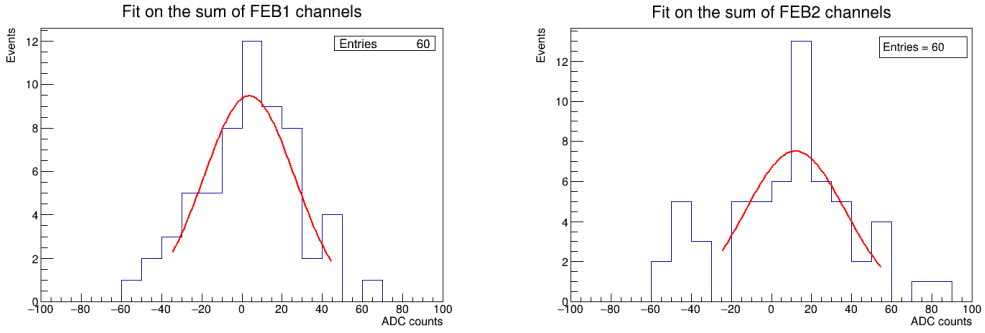

(a) (b)

Figure 5.14: Single event fit on the sum of the first 60 bins of the two boards.

To quantify the contribution to the total noise of the coherent term, for each channel the ratio R_N, defined in the previous section, has been calculated. The expected value of the ratio in case of null contribution of the coherent term of the noise is 1. The more this ratio exceeds the unity the more coherent noise is present. From the values of the ratio it is possible to calculate the value of the parameter k defined as the squared ration of the coherent term over the intrinsic one. The values for each channel of the ratio R_N and of the coefficient k are reported graphically in in fig. 5.16 and 5.17, while the mean values of k for the two boards are reported in the table 5.4.

From the value of k it is possible to calculate the two components of the noise C_{in} and C_c. The results of the calculations are reported together with the values of k in table 5.4. The values of the coherent component are comparable to the ones of the intrinsic term. It

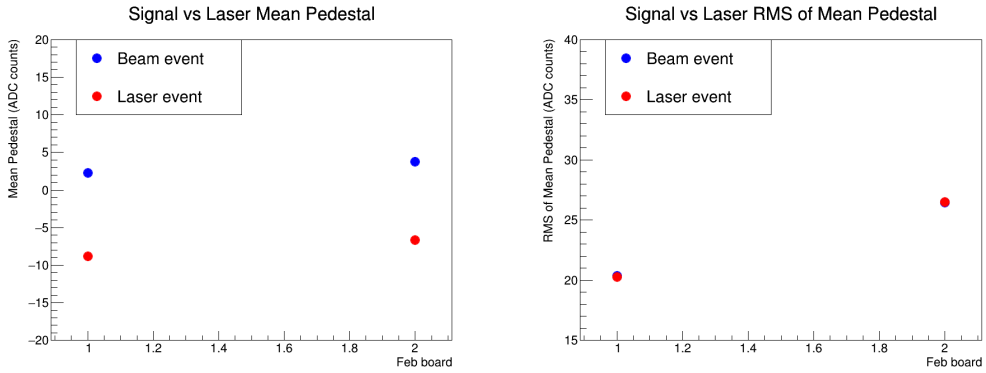

(a) (b)

Figure 5.15: Final values of the mean baseline (a) and RMS (b) for the sum of the channels of the two boards.

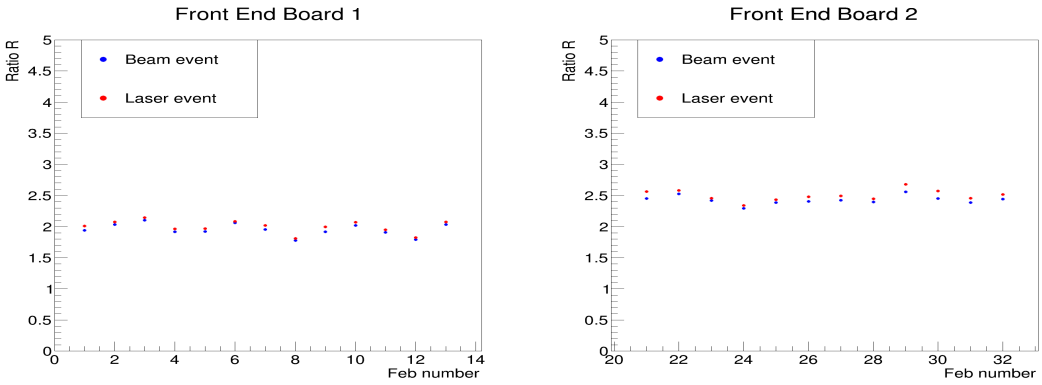

Figure 5.16: Value of the ratio R_N for all the channels

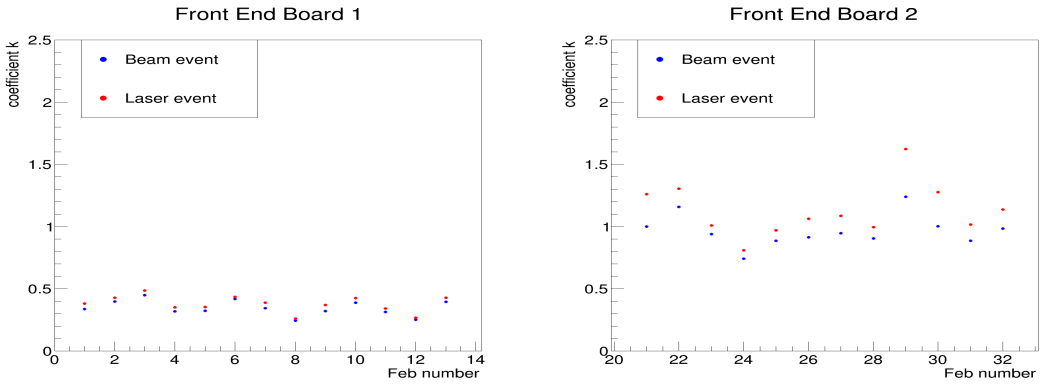

Figure 5.17: Values of the parameter k for all the channels.

means that removing the source of coherent noise it is possible to reduce significantly the final noise of a single channel, that implies reducing even more the noise on a measure spread on different channels, since the coherent noise sums linearly. The value of k doesn't show a particular trend related to the change of energy of the beam. On the other hand, the coherent noise of the second front end board is much higher than the in the first one. A further analysis on the correlation between the channels is needed in order to understand whether there are few channels cross-talking that are influencing the others or if the source of noise is common to all the channels.

Energy			k	C_1 (ADC)	C_{in} (ADC)	C_c (ADC)
4 GeV	FEB 1	beam	0.34	2.90	2.50	1.47
		laser	0.38	2.82	2.40	1.48
	FEB 2	beam	0.96	3.14	2.50	2.21
		laser	1.13	3.06	2.10	2.23
5 GeV	FEB 1	beam	0.39	2.95	2.50	1.56
		laser	0.44	2.85	2.38	1.57
	FEB 2	beam	1.01	3.13	2.21	2.22
		laser	1.04	3.06	2.13	2.17
6 GeV	FEB 1	beam	0.34	2.89	2.50	1.46
		laser	0.36	2.83	2.42	1.46
	FEB 2	beam	1.05	3.13	2.20	2.24
		laser	1.35	3.03	1.98	2.30

Table 5.4: Values of k, C_{in} and C_c for the different data sets.

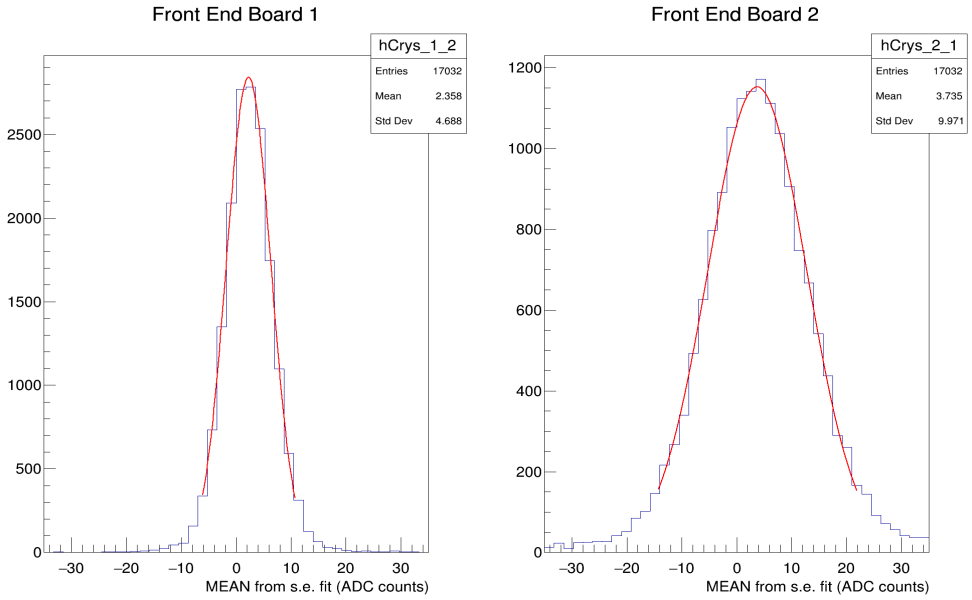

(a)

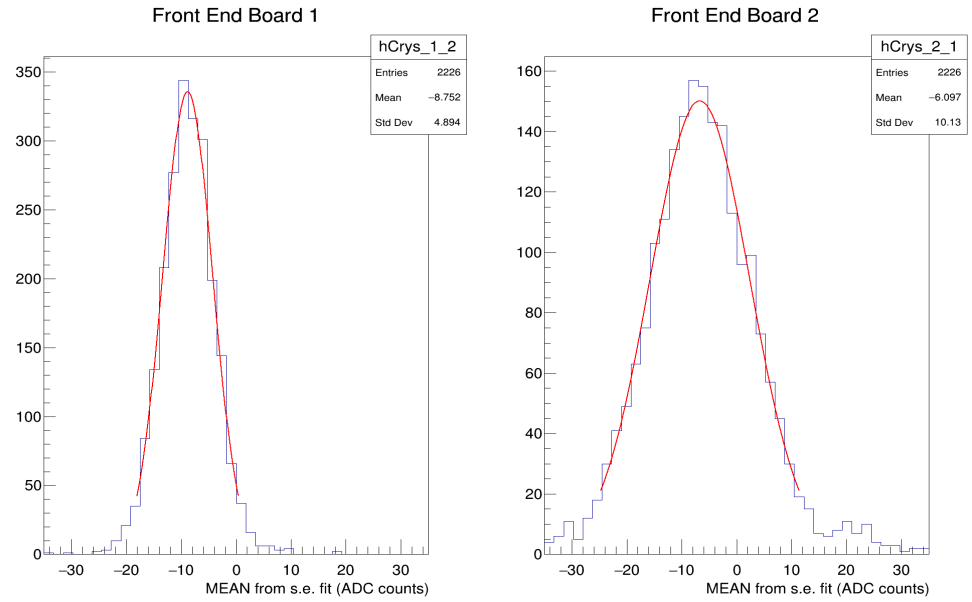

(b)

Figure 5.18: Histograms containing all the values of the mean obtained in the event-by-event analysis for the two boards. Top line represents the beam events and bottom line the laser events.

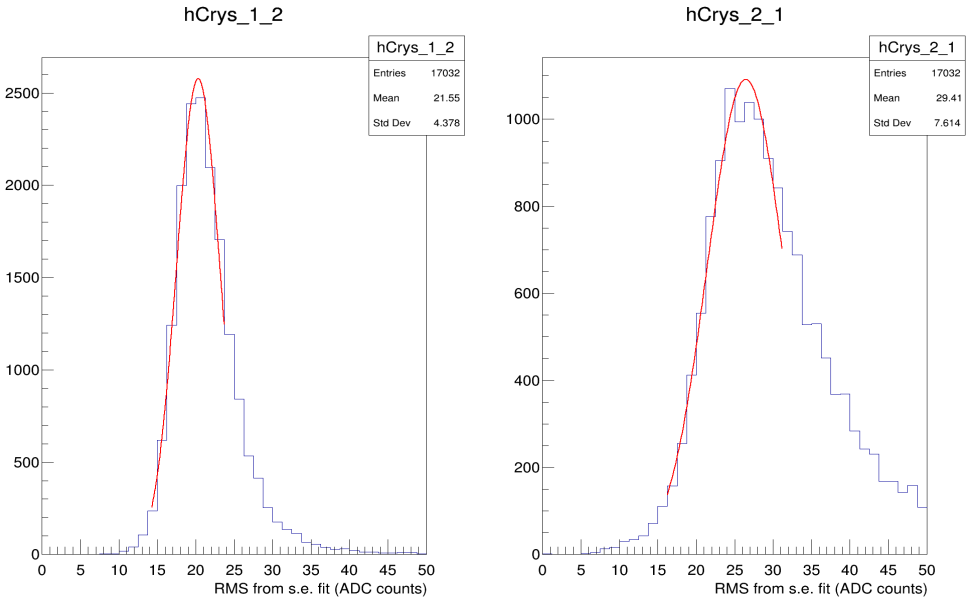

(a)

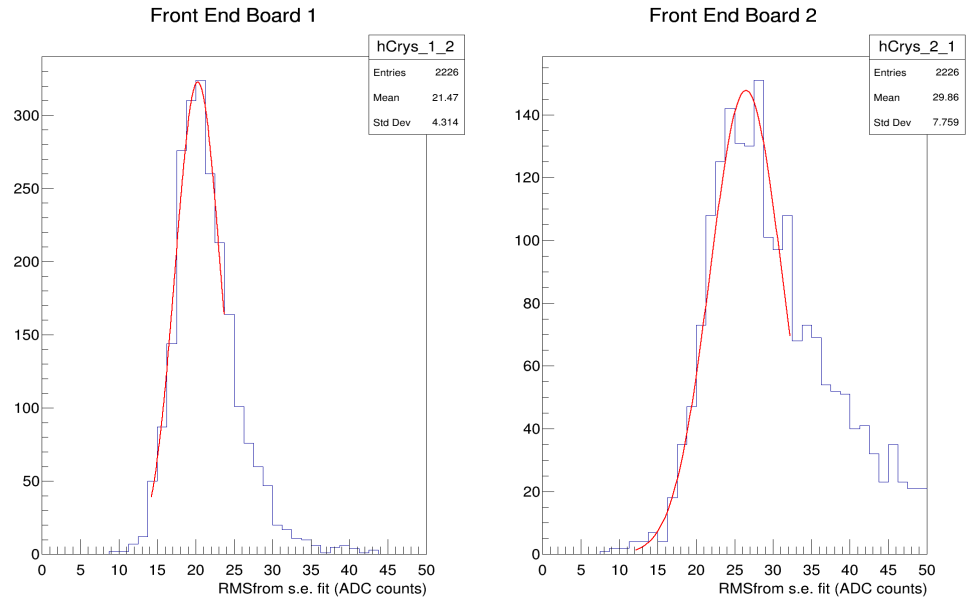

(b)

Figure 5.19: Histograms containing all the values of the RMS obtained in the event-by-event analysis for the two boards. Top line represents the beam events and bottom line the laser events.

Conclusions

In this thesis the role of the calorimeter in the MUonE experiment has been investigated through the use of MC simulations and also a first analysis on the calorimeter Test Beam of July 2022 has been performed. Regarding the study of the calorimeter performances with simulations, the Fast Sim simulation tool has been updated including NNLO radiative corrections provided by the new version of the MESMER MC event simulator. The response of the calorimeter has been confirmed even in presence of up to real photons in the final state of the process. The mean fraction of energy deposited in an array of 3×3 crystals is comparable with the one obtained in [22] in case of NLO events. Also the energy resolution of the calorimeter has been estimated, without considering the electronic noise term, not included in the simulation. As for the role of the calorimeter inside the experimental program of MUonE experiment, this thesis confirms capital role of the calorimeter as a support of the tracking system but also as a standalone resource for the data analysis. In fact, it has been demonstrated that the calorimetric information on the position of the outgoing electron can resolve the ambiguity on the particle identification due to the tracking system angular resolution. The algorithm for the selection of the elastic events proves to works and to remove radiative events also at NNLO. Moreover, the software analysis on the reconstruction of the Mandelstam variable t proves that the measure with the calorimeter has a better resolution than the one obtained by the tracking system. This is an important result and will be further investigated by performing the final template fit analysis using the distribution of t from calorimetric information rather then the angular distributions.

Finally, the results of data analysis of the Test Beam reported in the last section of this thesis shows that, in this configuration, the calorimeter has on average 3 ADC counts of noise per channel, but a consistent part of this noise has a coherent source and is shared between the channels. The future studies should focus on finding the source of coherent noise and find a way to remove it. Overall, the calorimeter performance in the Test

Beam was positive and it represents an important step towards its future contribution to the MUonE experiment.

Bibliography

[1] Dirac Paul Adrienne Maurice. The quantum theory of the electron. *Proc. R. Soc. Lond. A*, 117(778):610–624, 1928.

[2] P. Kusch and H. M. Foley. The magnetic moment of the electron. *Phys. Rev.*, 74:250–263, Aug 1948.

[3] T. Aoyama et al. The anomalous magnetic moment of the muon in the standard model. *Physics Reports*, 887:1–166, 2020. The anomalous magnetic moment of the muon in the Standard Model.

[4] V B Berestetskii, O N Krokhin, and A K Khlebnikov. Concerning the radiative correction to the *mu*-meson magnetic moment. *Soviet Phys. JETP*, Vol 3, 12 1956.

[5] Friedrich Jegerlehner. *The Anomalous Magnetic Moment of the Muon*, volume 274. Springer, Cham, 2017.

[6] Particle Data Group and Zyla. Review of Particle Physics. *Progress of Theoretical and Experimental Physics*, 2020(8), 08 2020. 083C01.

[7] Borsanyi et al. Leading hadronic contribution to the muon magnetic moment from lattice QCD. *Nature*, 593:51–55, 2021.

[8] Fred Jegerlehner and Andreas Nyffeler. The muon g−2. *Physics Reports*, 477(1):1–110, 2009.

[9] Thomas Blum, Norman Christ, Masashi Hayakawa, Taku Izubuchi, Luchang Jin, Chulwoo Jung, and Christoph Lehner. Hadronic light-by-light scattering contribution to the muon anomalous magnetic moment from lattice QCD. *Physical Review Letters*, 124(13), apr 2020.

[10] Junjie Cao, Yangle He, Jingwei Lian, Di Zhang, and Pengxuan Zhu. Electron and muon anomalous magnetic moments in the inverse seesaw extended NMSSM. *Physical Review D*, 104(5), sep 2021.

[11] J. Grange, V. Guarino, P. Winter, M., E. Swanson, T. van Wechel, and K. Lynch. Muon (g-2) technical design report, 2015.

[12] Muon g 2 Collaboration. Measurement of the Positive Muon Anomalous Magnetic Moment to 0.46 ppm. *Physical review letters*, 126(141801):1–11, 2021.

[13] G. W. Bennett et al. Final report of the e821 muon anomalous magnetic moment measurement at BNL. *Physical Review D*, 73(7), apr 2006.

[14] Tsutomu Mibe. New g−2 experiment at j-parc. *Chinese Physics C PACS*, 3440:745–748, 07 2010.

[15] G Abbiendi. Letter of Intent: the MUonE project. Technical report, CERN, Geneva, Jun 2019. The collaboration has not yet a structure, therefore the names above are for the moment an indication of contacts.

[16] C.M. Carloni Calame, M. Passera, L. Trentadue, and G. Venanzoni. A new approach to evaluate the leading hadronic corrections to the muon g-2. *Physics Letters B*, 746:325–329, 2015.

[17] Measurement of the running of the QED couplingin small-angle bhabha scattering at LEP. *The European Physical Journal C*, 45(1):1–21, jan 2006.

[18] G. Abbiendi, C. M. Carloni Calame, U. Marconi, C. Matteuzzi, G. Montagna, O. Nicrosini, M. Passera, F. Piccinini, R. Tenchini, L. Trentadue, and G. Venanzoni. Measuring the leading hadronic contribution to the muon g-2 via $\mu e \to \mu$ e scattering. *The European Physical Journal C*, 77(3), mar 2017.

[19] G Abbiendi. Status of the MUonE experiment. *Physica Scripta*, 97(5):054007, apr 2022.

[20] G. Abbiendi, G. Ballerini, D. Banerjee, J. Bernhard, M. Bonanomi, C. Brizzolari, L.G. Foggetta, M. Goncerz, F.V. Ignatov, M. Incagli, M. Kucharczyk, U. Marconi, V. Mascagna, C. Matteuzzi, R. Pilato, D. Pocanic, M. Prest, A. Principe, F. Ronchetti, M. Soldani, R. Tenchini, E. Vallazza, G. Venanzoni, M. Witek, and M. Zdybal. A study of muon-electron elastic scattering in a test beam. *Journal of Instrumentation*, 16(06):P06005, jun 2021.

[21] The Phase-2 Upgrade of the CMS Tracker. Technical report, CERN, Geneva, Jun 2017.

[22] Eugenia Spedicato. *Fast simulation of the MUonE 2021 test run setup.* PhD thesis.

[23] Massimo Alacevich, Carlo M. Carloni Calame, Mauro Chiesa, Guido Montagna, Oreste Nicrosini, and Fulvio Piccinini. Muon-electron scattering at NLO. *Journal of High Energy Physics*, 2019(2), feb 2019.

[24] Carlo M. Carloni Calame, Mauro Chiesa, Syed Mehedi Hasan, Guido Montagna, Oreste Nicrosini, and Fulvio Piccinini. Towards muon-electron scattering at NNLO. *Journal of High Energy Physics*, 2020(11), nov 2020.

[25] Ettore Budassi, Carlo M. Carloni Calame, Mauro Chiesa, Clara Lavinia Del Pio, Syed Mehedi Hasan, Guido Montagna, Oreste Nicrosini, and Fulvio Piccinini. NNLO virtual and real leptonic corrections to muon-electron scattering. *Journal of High Energy Physics*, 2021(11), nov 2021.

[26] Ettore Budassi, Carlo M. Carloni Calame, Clara Lavinia Del Pio, and Fulvio Piccinini. Single $\pi 0$ production in μe scattering at MUonE. *Phys. Lett. B*, 829:137138, 2022.

[27] N. Doble, L. Gatignon, G. von Holtey, and F. Novoskoltsev. The upgraded muon beam at the sps. *Nuclear Instruments and Methods in Physics Research Section A: Accelerators, Spectrometers, Detectors and Associated Equipment*, 343(2):351–362, 1994.

[28] H. A. Bethe. Molière's theory of multiple scattering. *Phys. Rev.*, 89:1256–1266, Mar 1953.

[29] Particle Data Group, P A Zyla, R M Barnett, J Beringer, O Dahl, D A Dwyer, D E Groom, C J Lin, K S Lugovsky, E Pianori, D J Robinson, C G Wohl, W M Yao, K Agashe, and W Aielli, G. Review of Particle Physics. *Progress of Theoretical and Experimental Physics*, 2020(8), 08 2020. 083C01.

[30] G. Grindhammer, M. Rudowicz, and S. Peters. The fast simulation of electromagnetic and hadronic showers. *Nuclear Instruments and Methods in Physics Research Section A: Accelerators, Spectrometers, Detectors and Associated Equipment*, 290(2):469–488, 1990.

[31] G. Grindhammer and S. Peters. The parameterized simulation of electromagnetic showers in homogeneous and sampling calorimeters, 2000.

[32] Soon Yung Jun. Gflash as a parameterized calorimeter simulation for the CMS experiment. *Journal of Physics: Conference Series*, 293:012023, apr 2011.

[33] Christian W. Fabjan and Fabiola Gianotti. Calorimetry for particle physics. *Rev. Mod. Phys.*, 75:1243–1286, Oct 2003.

[34] T.C. Awes, F.E. Obenshain, F. Plasil, S. Saini, S.P. Sorensen, and G.R. Young. A simple method of shower localization and identification in laterally segmented calorimeters. *Nuclear Instruments and Methods in Physics Research Section A: Accelerators, Spectrometers, Detectors and Associated Equipment*, 311(1):130–138, 1992.

Ringraziamenti

Alla fine di questo percorso vorrei ringraziare le persone che hanno reso possibile questo mio traguardo.

Ringrazio il mio relatore, il professor Simonetto, che negli ultimi tre anni mi ha insegnato tanto, ha avuto la pazienza di spiegarmi anche le cose che già pensavo di sapere e mi ha sempre sostenuto e aiutato a raggiungere i miei obiettivi.
Ringrazio il mio correlatore il dott. Conti e tutta la collaborazione MUonE per avermi accolto nel gruppo e per avermi fatto fare esperienze in cui non tutti gli studenti possono sperare. In questi mesi ho avuto la fortuna di conoscere persone appasionate del prorio lavoro, che mi hanno subito messa a mio agio, mi hanno fatto crescere e fatto apprezzare ancora di più questo mondo di cui ho iniziato a far parte.
Tra questi ringrazio in particolar modo il professor Abbiendi e Eugenia che fin dai primi giorni mi hanno seguita e hanno fatto chiarezza sui miei mille dubbi, sempre disponibili e pronti ad aiutarmi.
Ringrazio poi Anna e Christian, che hanno reso l'università un posto migliore. Grazie Anna per la tua amicizia, non scontata e che negli anni si è rafforzata sempre di più. Grazie per la tua leggerezza e per tutte le risate che hanno reso le lezioni più sopportabili. E grazie anche a te Christian, di avermi passato tutti gli appunti che non prendevo quando ero stanca e perchè sei sempre stato disponibile a studiare assieme per gli esami, anche per quelli che non dovevi dare. Senza di voi non mi sarei mai laureata.

Infine alcuni ringraziamenti speciali.

Ringrazio i miei genitori e mia sorella, il cui affetto non mi abbandona mai e da cui mi sento sempre protetta. Spero di potervi rendere orgogliosi come io lo sono di voi.
Ringrazio Filippo, che condivide con me tutte le gioie e le fatiche e sa sempre come spingermi a dare il meglio. Grazie di essere sempre al mio fianco.

Ringrazio mia nonna, che non dubita mai delle mie capacità e la cui forza è per me un grande esempio.
Ringrazio tutti i miei familiari e le mie amiche di una vita. Mi avete accompagnato fin qui e non avrei potuto chiedere di meglio.

Grazie,

Sara